Galaxies and Active Galactic Nuclei in Galaxy Clusters: Insights from Cosmological Simulations

Gregor Rihtaršič

Munich 2022

Galaxien und aktive Galaxienkerne in Galaxienhaufen: Erkenntnisse aus kosmologischen Simulationen

Gregor Rihtaršič

München 2022

Galaxies and Active Galactic Nuclei in Galaxy Clusters: Insights from Cosmological Simulations

Gregor Rihtaršič

Master's Thesis

at the Faculty of Physics

Ludwig Maximilian University

Submitted by

Gregor Rihtaršič

born in Kranj

Supervised by

PD Dr. Klaus Dolag

Assist. Prof. Dr. Dunja Fabjan

Dr. Veronica Biffi

Munich, August 24, 2022

Contents

Chapter 1

Introduction

Galaxy clusters are the largest collapsed structures in the Universe. Their deep gravitational potential wells, densely populated with galaxies and filled with hot cluster gas, host extreme conditions that can significantly influence the evolution of cluster galaxies. Processes like ram-pressure stripping and strangulation can remove the cold gas reservoir from the galaxies, potentially quenching star formation and suppressing the activity in galactic nuclei, governed by the accretion onto the supermassive black holes (i.e., AGN activity). On the other hand, cluster outskirts are believed to be a particularly suitable environment for AGN activity due to the relatively high density of galaxies with low velocity dispersion. The intricate interplay between the environmental processes, star formation rate and AGN activity, which itself can influence star formation via feedback processes, is a topic of extensive research in astrophysics. Recent X-ray studies have found a lack of active galactic nuclei in the inner cluster regions (Koulouridis et al. 2018, Ehlert et al. 2014) and an excess on the cluster outskirts (Koulouridis & Bartalucci 2019). This work aims to complement those studies by investigating AGN activity in the large-scale cosmological hydrodynamical simulations from the Magneticum suite. It explores the radial profiles of AGN activity in clusters and groups with $M_{500} > 10^{13} M_{\odot}$, while going beyond that, shedding light on the correlation with star formation, effects of the local density and the large-scale environment. It also attempts to constrain the underlying processes governing star formation and AGN activity.

This thesis is organised as follows: chapter 1 serves as a broad introduction to cosmology, active galactic nuclei and galaxy clusters. It discusses the distribution of dark matter and galaxies in galaxy clusters and defines the density profile that is used for regression in appendix B. It introduces cluster galaxies and larger substructures in the context of hierarchical structure formation and discusses different processes that can potentially impact the AGN activity and star formation. Chapter 2 presents the Magneticum simulations and the algorithm Subfind, used for identification of galaxies and clusters. It also defines the quantities used throughout this work. Chapter 3 explores how the large-scale environment and overlaps between cluster regions impact the radial profiles of individual clusters. Chapter 4 investigates the properties of cluster galaxies and their correlation with the environment, mostly focusing on star formation rate, while chapter 5 investigates AGN activity in galaxy clusters. The

focal points of those two chapters are the radial profiles of the ratio between the number of star-forming and quiescent galaxies and the fraction of galaxies hosting an X-ray bright AGN. The main conclusions are summarized in chapter 6. Statistical uncertainties and confidence intervals used in this work are derived in appendix A.

1.1 Active Galactic Nuclei

Some of the galaxies in the Universe display phenomena in their nuclear regions that cannot be explained by stellar activity. These systems are called *active galactic nuclei (AGN)* and are characterized by unique observational signatures over the whole electromagnetic spectrum. They can have very high bolometric luminosities, up to 10^{48} erg/s, and can outshine their host galaxies by several orders of magnitude, making them some of the brightest non-explosive sources in the Universe. Observations of the first AGN date back to the beginning of the 20th century, when Fath (1909) reported on the intriguing spectrum of NGC 1068, with emission lines superimposed on the absorption spectrum of a galaxy. Since then, the studies of AGNs have evolved into a prominent field in astrophysics.

Galaxies can show signs of nuclear activity in various ways. Hence, a complex taxonomy has been developed to classify different AGNs in the "AGN zoo" based on the observed properties (summarized in Cimatti et al. 2019, Padovani et al. 2017). All AGN types can be roughly divided into a few categories. *Quasars* are some of the brightest AGNs and have been identified up to very high redshifts. They were initially discovered as optical counterparts of radio sources of unknown origins. Since they resembled point-like stars in early observations, they were dubbed quasi-stellar radio sources (quasars); however, their spectra revealed that they are much more luminous objects at high redshifts (Schmidt 1963). *Seyfert galaxies*, named after Carl Seyfert, that first reported on them in 1943 (Seyfert 1943), share many properties with quasars; however, they are less luminous (10^{43} – 10^{45} erg/s), and their host galaxies are clearly detectable. *Radio galaxies* are characterized by strong radio emission, similar to some quasars, but their cores are not as luminous. The regions of radio emission extend far beyond the host galaxies, reaching the scales from tens of kpc to Mpc, often forming two *radio lobes* on each side of the radio galaxy, with areas of high surface brightness, called *hot spots*. They are often connected to the galaxy with relativistic *jets*. *Blazars* are a class of AGNs, particularly bright over the entire electromagnetic spectrum. In blazars, relativistic jets are oriented at small angles with respect to the observer, which causes relativistic effects such as Doppler boosting, and rapid time variability of the flux on the scale of hours at high energies (X-ray) or weeks/months at longer wavelengths. One of the sub-classes of blazars, *BL Lacertae* objects, got its name after the object with star-like morphology, initially thought to be a variable star within our galaxy. Beyond the main groups, AGNs are further divided into sub-classes based on their spectra. In radio wavelengths, we divide quasars into radio-loud and radio-quiet, and radio galaxies into *FR I* and *FR II* galaxies.

In optical wavelengths, we divide AGNs into *Type 1* AGNs with broad emission lines, while the AGNs with only narrow lines are called *Type 2* AGNs.

Despite the complex taxonomy of AGNs and a large variety of spectral properties, the models have been successfully unified, attributing all observed signatures to a single physical object. The nature of the source of the AGN activity can be illustrated by considering a few AGN properties. The total luminosity can only vary on timescales, larger than required to bring the information (travelling with the speed of light) across the source region. The rapid time variability of AGNs thus indicates a very compact source in the galactic centre, on the scale of a miliparsec. Furthermore, broad emission lines, observed in optical spectra, caused by extremely high orbital velocities of the emitting material (up to 10 000 km/s) indicate the presence of a very massive object. Following the works of Salpeter (1964) and Zel'dovich & Novikov (1964), it is now a general consensus that the AGNs are powered by gravitational energy released during the accretion of matter onto a supermassive black hole in the centre of the galaxy.

Black Holes: General theory of relativity, proposed by Albert Einstein in 1915, predicts that if an object with a finite mass is confined to a small enough volume, it bends the surrounding space-time to the point where it decouples from the rest of the Universe. It forms a region that nothing, not even light, can escape, called a *black hole* (Carroll 2019). Black holes were initially treated as a purely mathematical phenomenon until, in the 1960s, evidence started to mount for the existence of astrophysical black holes. First observational evidence of stellar-mass black holes, predicted to form after the collapse of massive stars, was provided with the observations of an X-ray binary Cygnus X-1 (Bolton 1972, Webster & Murdin 1972). Meanwhile, the observations of active galactic nuclei provided evidence for another class of black holes, reaching masses of the order of dwarf galaxies, between 10^6 to 10^{10} solar mass ($M_\odot$), the so-called *supermassive black holes* (SMBHs). Supermassive black holes are believed to be found in the centres of most galaxies in the Universe (e.g., Magorrian et al. 1998), although their origin is still subject to debate. It is hypothesized that the progenitor black holes (tens or hundreds $M_\odot$) can form via the collapse of a very massive star, the collapse of a gas cloud or from a very dense star cluster via relativistic instability (e.g., see Rees 1978). The collapse may also be triggered by the extreme pressure in the early Universe, forming the so-called primordial black holes. After the seeding of the progenitor black holes, supermassive black holes grow via mergers and accretion of matter (e.g., Pacucci & Loeb 2020, Kulier et al. 2015). AGN activity, which can hardly be explained with other processes than the accretion onto supermassive black holes, is a strong piece of evidence of their existence but is not the only one. For example, the velocity dispersion of stars in the centre of other galaxies also points to the existence of very massive central objects (Wolfe & Burbidge 1970). Observations have also revealed the presence of a massive black hole in the centre of our galaxy, by detection of a central radio source of synchrotron radiation (Balick & Brown 1974) and by direct observations of stellar orbits near the galactic

centre (Eckart & Genzel 1996)[1]. In 2019, the Event Horizon Collaboration published the first horizon scale image of a supermassive black hole and its shadow in a galaxy M87 (Event Horizon Telescope Collaboration 2019), even further proving that the AGN activity is fuelled by SMBHs. The image was followed by the first image of the supermassive black hole in the centre of our galaxy, released just a few months prior to the submission of this thesis (Event Horizon Telescope Collaboration 2022). Both images are shown in figure 1.1.

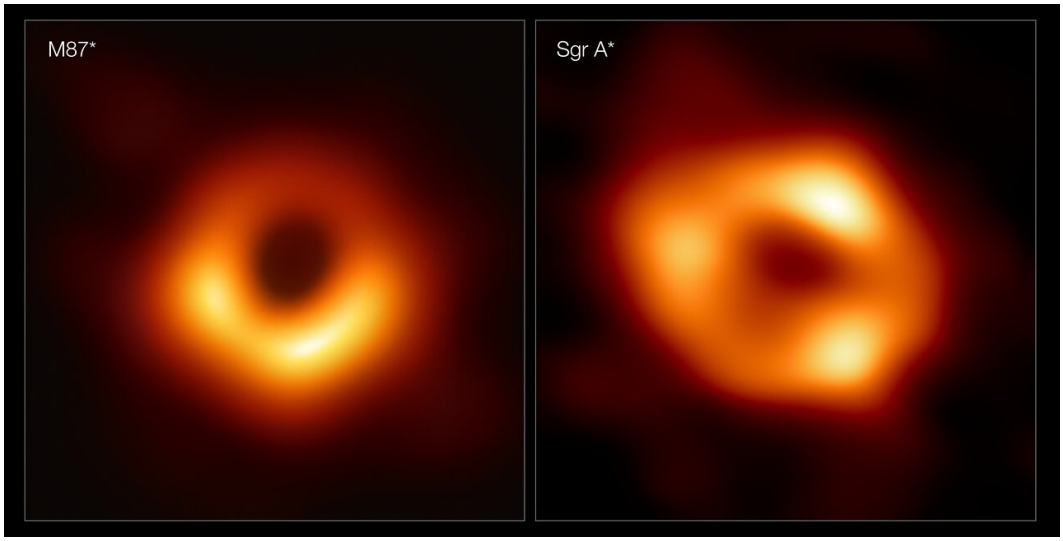

Figure 1.1: The 1.3 mm microwave image of the supermassive black hole in M87 (left panel) and in the Milky Way (*Sgr A**, right panel), captured by the Event Horizon Telescope (EHT). The central dark spot represents the shadow of the black hole, a few times larger than the event horizon, surrounded by hot emitting gas. The images are taken from Event Horizon Telescope Collaboration (2019) and Event Horizon Telescope Collaboration (2022) and are also available at `www.eso.org`.

The mechanism powering AGN emission is fuelled by the gas in the inner galactic regions. This gas is transported from distant regions in the galaxy to the 100 pc vicinity of the SMBH by different processes, e.g., galaxy mergers and interactions, bar instabilities, and other internal processes. The exact mechanism for bringing the gas to the inner 10 pc is still unknown. When the gas is transported to the vicinity of the central black hole, it is subjected to various forces. It starts to feel the gravitational pull of the black hole, and of the surrounding gas. It is exposed to radiation and thermal pressure, stellar winds and supernova explosions of stars, densely populating the galactic centre. The gravitational potential energy of the gas is transformed into kinetic energy as the gas falls into the potential well of the SMBH, and is further dissipated through viscous friction, which heats the gas and causes thermal emission. If the infalling gas has low angular momentum, it can be accreted via the so-called spherical accretion, described by the Bondi model (see section 2.3), if the gravitational force is stronger than radiation pressure. If angular momentum is large, the gas settles into circular orbits with minimum energy, forming an accretion disc around the black hole. Inside the accretion disc, differential rotation of different layers causes viscous friction

[1]For confirming the existence of a supermassive black hole in the centre of the Milky Way by obseving stellar orbits, Reinhard Genzel and Andrea Ghez were awarded a Nobel Prize in Physics in 2020.

and transports angular momentum outward, allowing the gas to approach the black hole. In general relativity framework, the gas cannot orbit the black hole in arbitrarily low orbits, like in Newtonian dynamics - the extreme curvature of space-time adds higher order terms to the effective potential and prevents particles with some minimal angular momentum from orbiting the black hole in a stable orbit. The accretion disc can thus only exist down to the location of the *innermost stable circular orbit* (ISCO); if a gas parcel falls below this orbit, it is bound to spiral into the black hole. This also limits the amount of gravitational energy that can be dissipated and emitted as radiation. The radius of the ISCO largely depends on the black hole spin; if the angular momentum of the accretion disc is aligned with the black hole spin, the gas can reach lower orbits, and more energy can be radiated away compared to retrograde accretion, where the angular momentum vectors are counter-aligned (Netzer 2013).

The accretion of the gas onto the SMBH is a complex process giving rise to different spectral features. Thermal radiation of the hot gas in the accretion disc peaks in the UV wavelengths. It can also excite clouds of gas in the vicinity of the black hole, contributing to the emission lines. Furthermore, the disc is believed to be surrounded by a hot corona, with temperatures up to 10^7K, which can inverse Compton scatter photons and produce X-ray emission. A bit further out from the centre, between 0.1 and 10 pc, the AGN is surrounded by a large torus of dust, which causes the absorption features and the infrared emission, and is essential for explaining the large variety of AGN types; If oriented perpendicular to the observer, it can obscure the central regions, significantly altering the observed AGN properties. Some AGNs produce *jets*, collimated relativistic outflows of particles emerging above and below the accretion disc, which are visible over the entire electromagnetic spectrum but most notably contribute to radio wavelengths. Jets can deposit energy far away from their host galaxy. When interacting with the medium surrounding the galaxies, they can produce *radio lobes*, symmetric regions of radio emission on both sides of the host galaxy that can reach scales from kpc to Mpc. The orientation of jets with respect to the observer can affect the spectrum and the AGN classification.

SMBHs grow and emit energy in two distinct modes. In *radiatively efficient mode* (or quasar mode), the accretion disc is formed around the black hole, as described above, enabling the emission of a large fraction of potential energy. In radiatively efficient mode, the black hole accretes with a high accretion rate. *Radiatively inefficient mode* (also called radio mode), on the other hand, is characterized by a low accretion rate and low efficiency of energy conversion to radiation since the matter is advected to the centre without dissipating the energy via the accretion disc. SMBHs in radio mode release most of their energy into their surroundings in the form of kinetic energy via powerful radio jets, often associated with them, while SMBHs in quasar mode emit most of the energy via radiation. Black holes are believed to spend most of the time in radiatively inefficient mode.

X-ray observations: X-ray emission seems to be one of the most reliable indicators of AGN activity, since it is observed in many different AGN types, even if they are obscured in other wavelengths. However, X-ray AGN identification also faces some limitations. AGNs are not the only sources of X-rays observed in the Universe; galaxies can also emit in X-rays due to hot interstellar gas, supernova remnants and X-ray binary populations. The hot gas in galaxy clusters is also an important source of X-ray emission (see section 1.3). Furthermore, some AGNs may also be obscured in X-ray, appearing weaker than expected. In order to get a complete sample of AGNs, not contaminated by other sources of X-ray emission, high luminosity thresholds ($\sim 10^{42}$ erg/s) are usually used for identification of *X-ray bright* AGNs (e.g., Koulouridis & Bartalucci 2019, Koulouridis et al. 2018, Ehlert et al. 2014, Haggard et al. 2010). The abundance of such AGNs in galaxies is not high; however, modern X-ray telescopes (e.g., Chandra X-ray observatory) and their deep extra-galactic surveys opened the door for statistically meaningful analysis of the environmental dependence of AGN activity. For an overview of X-ray surveys, see Brandt & Hasinger (2005).

1.2 Cosmology and Structure Formation

At the beginning of the 20th century, the Universe was believed to be static and unchanging. This idea started to be questioned in the advent of general relativity when equations started to hint at the possibility of an expanding Universe (Friedmann 1924), although efforts were made to preserve the deeply rooted idea of a static Universe (e.g., Einstein introducing the cosmological constant in Einstein 1917). In 1929, Edwin Hubble proved that the Universe is expanding by observing that the radial velocities of galaxies increased with distance, according to what is now known as the *Hubble law*[2] (Hubble 1929):

$$\frac{v}{d} = H_0 = h \cdot 100 \mathrm{kms}^{-1}\mathrm{Mpc}^{-1} = \left(\frac{\dot{a}}{a}\right)_{t=0}, \tag{1.1}$$

where v is the radial velocity of a galaxy at a distance d from the observer. The Hubble constant H_0 can be interpreted as the relative volume expansion rate of the present-day Universe. The expansion of the Universe is described with the *scale factor* a, which is proportional to the size of some comoving volume of space, and is set to 1 at present day. Hubble constant can be expressed with dimensionless parameter h, which is often explicitly expressed in physical quantities to emphasize their underlying dependence on cosmology (Croton 2013). Throughout this work, distances are often expressed in kpc/h. If the expansion of the Universe is traced back in time, it can be seen that at some point in the past, distances between all objects in the Universe were zero (the so-called *Big Bang singularity*). Assuming the constant expansion rate (H_0), we can estimate the time passed from the big bang by defining the *Hubble*

[2]The hypothesis that the Universe is expanding, based on the measured radial velocities of galaxies, was also published by Georges Lemaitre a few years before Hubble (Lemaître 1927), hence the Hubble law is also known as the *Hubble-Lemaitre law*.

time:

$$t_h = \frac{1}{H_0}. \tag{1.2}$$

Using the value of the Hubble constant $H_0 \approx 70 \mathrm{kms}^{-1}\mathrm{Mpc}^{-1}$, we obtain that the Universe is around 14 billion years old. The expansion of the Universe is, in reality, not constant over time; current cosmological models and measurements estimate that the Universe is 13.7 billion years old (Planck Collaboration 2020).

In the expanding and possibly curved Universe, the meaning of distance is not straightforward anymore. One of the definitions used in this work, the *proper distance* d_p, is obtained by integrating the FLRW metric between two points in space with constant time coordinate (e.g., see Weinberg & Steven 1972). While this may be a good way of measuring the "actual" distances between objects, it makes for a rather confusing description of relative distances in an expanding Universe, where objects follow the flow of the cosmological fluid (i.e., the *Hubble flow*) and are drifting apart. The *comoving distance* d_c is defined as

$$d_c = \frac{d_p}{a}. \tag{1.3}$$

It is defined so that the objects, drifting apart solely due to the overall cosmic expansion, remain at the same comoving distance, which is equal to the proper distance at present ($a = 1$). Note that in the general case, the comoving distance is not equal to the *radial coordinate distance* r in the FLRW metric (Weinberg & Steven 1972), however in a flat Universe, that is assumed in this work, they are equivalent.

In the currently most widely accepted ΛCDM cosmological model, the Universe mainly consists of three components, of which the baryonic matter accounts for only a few per cent of the total energy density. Most of the matter in the Universe is in the form of *cold dark matter*, a type of matter which is believed to interact only through gravity. The term *cold* refers to its non-relativistic velocities. Dark matter accounts for less than a third of the total energy density; the rest is contributed by the *cosmological constant*, interpreted as the energy density of space, which can explain the accelerated expansion of the Universe.

In 1964, it was discovered that the present-day Universe contains a background of isotropic microwave radiation, called the *cosmic microwave background* (CMB) (Penzias & Wilson 1965), which was released only 370 000 years after the Big Bang, at the epoch of recombination, and is now considered to be one of our most important windows into the early Universe. The CMB is almost isotropic and has a 2.725 K black-body spectrum, with small temperature fluctuations (of the order of 10^{-5}). The temperature fluctuations reflect the small fluctuations of the baryonic matter density, formed under the influence of the dark matter fluctuations. The almost homogeneous Universe, indicated by the nearly isotropic CMB, is vastly different from what is observed in the present-day Universe; the small density perturbations have undergone gravitational evolution and grown into the tangled structure of

clumps and filaments, called the *cosmic web*. Amid the dense features of the cosmic web, vast under-dense regions are formed, called *cosmic voids*. The structure of the cosmic web can be seen in figure 2.1, where the gas in MAGNETICUM simulations (see chapter 2) is visualized, tracing the underlying dark matter distribution. Some dark matter over-densities collapse into gravitationally bound structures, decoupled from the overall cosmic expansions, called *dark-matter halos*. When the baryonic gas settles into the dark-matter halo potential well and gets dense enough, it starts to cool efficiently enough to form stars, leading to the creation of galaxies. It is believed that the vast majority of galaxies are hosted by dark matter halos. The abundance of dark matter halos with a certain mass, formed from the initial random density fluctuations, can be predicted with the *Press-Schechter formalism* (Press & Schechter 1974), and its extended version (Bond et al. 1991), which agree with the results of numerical simulations. The obtained halo mass function predicts a generally larger abundance of halos at low redshift and a higher abundance of low-mass halos.

1.3 Galaxy Clusters

The Press-Schechter formalism (Press & Schechter 1974) predicts that most dark matter halos in the Universe have low mass, on the scales of galaxies; however, the tail of the halo mass function also hints at the existence of very massive halos (above $10^{14} M_{\odot}$). The structures hosted by such massive halos are called *galaxy clusters*. Galaxy clusters are aggregations of hundreds to thousands of galaxies. With their radii on the Mpc scale, they are the largest gravitationally bound structures in the Universe that have had time to undergo gravitational collapse. In figure 2.1, galaxy clusters can be seen as dense hot (blue) spots of gas, residing at the nodes of the cosmic web, connected to the cosmic filaments.

Most of the mass in galaxy clusters, between 84 and 90 % is found in the form of dark matter. When Fritz Zwicky observed Coma clusters in 1933, he noticed the unusually high velocity dispersion of galaxies, indicating that the mass of the cluster was much larger than inferred from its emission. While referring to the invisible mass component, he coined the term dark matter (Zwicky 1933). The massive dark matter halo of galaxy clusters can be studied with gravitational lensing. Gravitational lensing studies of the Bullet Cluster, which consists of two colliding galaxy clusters, showed that the bulk of the dark matter is displaced with respect to the baryonic matter, which is one of the best pieces of evidence for the existence of dark matter to date (Clowe et al. 2006, Bradač et al. 2006).

Most of the baryonic mass in galaxy clusters is in the form of the *intracluster medium* (ICM). As the clusters form, the gravitational pull accelerates the gas and dark matter to high velocities. The gas converts most of its energy into thermal energy via shocks. The amounts of energy released are tremendous, making cluster formation one of the most energetic events since the Big Bang (Borgani & Kravtsov 2011). The virial temperatures of the ICM inside the cluster potential well reach up to $10^7 - 10^8$ K, and are responsible for the diffuse X-ray

emission due to thermal bremsstrahlung. The X-ray luminosity of the ICM can reach up to $10^{42} - 10^{45}$ erg/s and can be used to reliably identify galaxy clusters. It increases with ICM density towards the cluster centre and can potentially interfere with X-ray AGN identification (e.g., Ehlert et al. 2013a). The densest ICM regions in the centre are expected to emit energy and cool very efficiently, potentially causing a temperature inversion. The clusters in which the innermost regions are cool and dense are called *cool-core clusters*. The thermal structure of the cool core clusters, predicted from radiative cooling, does not agree with observations, indicating an additional source of feedback in the central regions. It is widely believed that the feedback is provided by the AGN activity in the cluster galaxies, injecting vast amounts of energy into the ICM (Borgani & Kravtsov 2011). This is one of the clearest examples of how the small-scale processes associated with active galactic nuclei can profoundly impact the large-scale environment of galaxies. Another way the hot ICM allows us to detect galaxy clusters is via *Sunyaev-Zeldovich effect*. As the photons of the CMB travel through the hot cluster gas, they inverse Compton scatter on the free electrons to higher energies, which appears as a distortion of the CMB spectrum. The observed distortion is independent of the cluster distance, which allows us to detect clusters at very high redshifts.

Aggregations of galaxies with masses below the cluster mass are called *galaxy groups*. The threshold mass for the cluster classification varies in the literature since the transition between cluster and the group regime is gradual, without any fundamental physical distinction between both. In this work, I will follow the convention in Koulouridis et al. (2018), and refer to all groups with mass above $10^{13} M_{\odot}$ as galaxy clusters, but it should be noted that according to some literature, this is well within the group regime (e.g., Cimatti et al. 2019). In chapters 4 and 5 it will be shown that the properties of galaxies in large galaxy groups do not differ drastically from those in more massive galaxy clusters.

1.4 Cluster Density Profile

The density distribution in cluster halos (and dark matter halos in general) is smooth, gradually declining with radius; hence, the definition of their size and mass is not self-explanatory. Conventionally, cluster radius and mass are defined as:

$$M_{\Delta} = \frac{4\pi}{3} \Delta \rho_{crit} R_{\Delta}^3, \tag{1.4}$$

where ρ_{crit} is the *critial density*, the total density of a flat Universe:

$$\rho_{crit} = \frac{3H^2}{8\pi G}. \tag{1.5}$$

G is the gravitational constant, and H is the Hubble parameter (relative expansion rate, defined analogously to H_0 in equation (1.1) at an arbitrary time). Radius R_{Δ} in equation (1.4) is defined as the radius of a sphere with average density Δ times ρ_{crit}, and M_{Δ} is the mass

of the sphere. If Δ is equal to the characteristic overdensity of virialized halos ($\Delta \approx 178$ in Einstein-de Sitter cosmology), the radius is referred to as the *virial radius*. In this work, I will follow the convention in the literature (e.g., Koulouridis & Bartalucci 2019, Ehlert et al. 2014) and use $\Delta = 500$. The cluster mass is hence defined as M_{500} in this work, and the clustercentric distance r is defined relative to R_{500} of the cluster:

$$r = \frac{\tilde{r}}{R_{500}}, \tag{1.6}$$

where $\tilde{r}$ is the absolute clustercentric distance.

Formation of dark matter halos is governed by the scale-independent gravitational force, resulting in the self-similar structure of halos of vastly different sizes. It turns out that the density profile of dark matter halos can be well described with Navarro-Frenk-White (henceforth *NFW*) profile (Navarro et al. 1997, 1996, 1995), which is remarkably universal. It can describe the density profile regardless of the cosmological parameters, the matter power spectrum of the initial fluctuations and the halo mass - it can be used to describe galaxies as well as the profiles of rich galaxy clusters (Navarro et al. 1997). The NFW profile is defined as:

$$\frac{\rho(\tilde{r})}{\rho_{crit}} = \frac{\delta_c}{(\tilde{r}/\tilde{r}_s)\,(1+\tilde{r}/\tilde{r}_s)^2}, \tag{1.7}$$

where δ_c is the characteristic, dimensionless density and $\tilde{r}_s$ is the scale radius, which scales with the size of the cluster (R_{500}). Thus, it is useful to define the relative scale radius r_s:

$$r_s = \frac{\tilde{r}_s}{R_{500}}, \tag{1.8}$$

so that $r/r_s = \tilde{r}/\tilde{r}_s$. The relative scale radius r_s is constant for halos of different sizes and is often given in the form of *concentration*, defined as

$$c_\Delta = \frac{R_\Delta}{\tilde{r}_s}, \tag{1.9}$$

c_{200} is conventionally used (e.g., Navarro et al. 1997). In this work, I use the NFW profile (equation (1.7)) to convert between r_s and c_{200}. The characteristic density δ_c can be expressed with c_{200} (from the definition of R_{200}, equation (1.4)):

$$\delta_c = \frac{200}{3}\frac{c_{200}^3}{[\ln(1+c_{200}) - c_{200}/(1+c_{200})]}, \tag{1.10}$$

hence if the total matter density profile is considered, the NFW profile has only one free parameter (c_{200}) (Navarro et al. (1997)).

It should be pointed out that other models with more parameters provide a more accurate description than the NFW profile with constant concentration (e.g., Einasto profile, Klypin et al. 2016, Einasto 1965). However, the NFW profile is still a solid approximation and is

extensively used due to its simplicity. Dependence of the concentration on the halo mass, redshift and the amount of substructure, has also been thoroughly studied (e.g., Ragagnin et al. 2019, Klypin et al. 2016, Bullock et al. 2001, Jing 2000, Navarro et al. 1997). Concentration is reported to decrease with redshift and gradually decrease with halo mass. In the early stages of the halo growth, mergers affect the entire halos, and thus the scale radius, which measures the size of the cluster core, grows together with the virial radius. In late stages, however, the mass is mostly accreted onto the outskirts, causing an increase in halo size while leaving the size of the core unchanged. As the smaller halos form at earlier times, they tend to be more concentrated than massive halos (Zhao et al. 2003, Bullock et al. 2001).

The distribution of dark matter in Magneticum simulations, used in this work, has been thoroughly studied in Ragagnin et al. (2019). In this work, I focus on the radial distribution of galaxies. It is still debatable whether galaxies are a reliable tracer of the dark matter profile in galaxy clusters. Some report agreement between the two (e.g., Wang et al. 2018, Bahcall & Kulier 2014), while others report different distributions of dark matter and cluster satellites (e.g., Budzynski et al. 2012). Numerical simulations have shown that the profile of galaxies and subhalos is usually less concentrated than the dark matter profile, mostly due to tidal interactions and stripping, which cause galaxies in the central regions to fall below the selection limit (Nagai & Kravtsov 2005). In this work, I use the NFW profile[3] for the number density of cluster galaxies:

$$\frac{\mathrm{d}N}{\mathrm{d}V}(r) = \frac{n_0}{(r/r_g)\,(1+r/r_g)^2} \tag{1.11}$$

with free parameters n_0 and r_g. n_0 is the fourfold number density of galaxies at r_g. The number density used in this work is defined as the number of galaxies with stellar mass above $10^{10} M_\odot/h$ per comoving volume, in clusters and groups with $M_{500} > 10^{13} M_\odot$. The details of the NFW profile fitting procedure is described in appendix B, and the parameter values can be found in table B.1. I find that despite being a solid approximation, the NFW profile is not as suitable for galaxies (especially massive galaxies) as it is for dark matter. From the obtained concentrations, I find that, unlike dark matter, galaxies are significantly more concentrated at high redshifts ($z = 0.90$) compared to lower redshifts ($z = 0.25$).

Stacking the Clusters: A significant portion of this work investigates different properties of galaxies as functions of their clustercentric distance. However, since one cluster does not always contain enough galaxies for statistically meaningful analysis, it is essential to combine different clusters and investigate the average radial profiles. Since clusters are just scaled versions of each other, as shown in section 1.4 it is meaningful to combine galaxies in *relative* radial spherical shells, defined with radius r, relative to R_{500} of each cluster. Note that the baryonic matter is subjected to processes which are not scale-independent anymore, and halos of different sizes can have vastly different gas distribution and properties. However,

[3]Other models are also used in the literature for the number density of galaxies, e.g., King analytic profile (King 1972), but I decide for the NFW profile to compare with the distribution of dark matter.

in the cluster and group mass ranges used in this work, this is still a better approach than, for example, comparing the galaxies at a constant absolute distance $\tilde{r}$. For details about the gas distribution in galaxy clusters, see Sarazin (1988). In chapters 4 and 5, I combine AGN and galaxy counts from relative radial shells of different clusters. The obtained profiles and their statistical uncertainties (derived in A.1 and A.2) refer to the *stacked* profile of all clusters; if we had a different random realisation of clusters (e.g., another cosmological box with different initial conditions), the combined profile would be expected within the errorbars displayed in chapters 4 and 5. However, since the clusters are roughly self-similar, the combined profile of all clusters is expected to resemble the expected profile of individual clusters. In appendix B, I explicitly demonstrate how the combined profile of several halos has the same density profile.

1.5 Hierarchical Growth and Substructure

The smooth density profile, discussed in section 1.4 is only an approximation of the actual distribution of matter in galaxy clusters. In ΛCDM cosmology, the structures grow hierarchically. As the initial density perturbations grow out of the linear regime, smaller dark matter halos virialise first and merge together to form larger systems. This process, also called *hierarchical merging*, is the main mechanism for the assembly of massive dark matter halos, complemented by a minor contribution from the accretion of diffuse matter (Cimatti et al. 2019). Due to hierarchical formation, massive cluster halos can host a significant amount of *substructure*; smaller halos (*subhalos*) embedded into the potential of the main cluster halo. Smaller subhalos can host galaxies, but not necessarily; if they had lost gas during their evolution, they are completely dark and can manifest themselves only through gravitational effects. Aside from galaxy-size halos, clusters can also contain larger group halos with multiple galaxies. In *regular clusters*, which appear relaxed and spherically symmetric (e.g., Coma cluster), the amount of substructure is smaller than in *irregular clusters* (e.g., Virgo cluster).

The merger history of a dark matter halo consists of mergers with similar size halos (*major mergers*) and the accretion of smaller halos (*minor mergers*). The frequency of mergers can be obtained with extended Press-Schechter formalism (Bond et al. 1991) or with N-body simulations (e.g., Rodriguez-Gomez et al. 2015 and references therein), and is increasing with redshift and decreasing with the mass ratio of the progenitors; meaning that minor mergers happen much more frequently than major mergers. Since the interactions between dark matter halos are dominated by scale-free gravitational force, the growth of galaxy-size halos resembles the growth of cluster-size halos in terms of merger mass ratios and rate. One dark matter halo is expected to undergo ~ 2 mergers with satellites with approximately 10% of its mass during its evolution up to the present. This means that a Milky Way size halo is expected to accrete at least one halo with $10^{11} M_{\odot}$, which is comparable to the mass of the Large Magellanic Cloud, Milky Way's largest satellite. On cluster scales, this means that

Virgo cluster size halo ($\sim 10^{14} M_{\odot}$) is expected to merge with 1-2 subhalos with $10^{13} M_{\odot}$ (which are expected to contain several bright galaxies) and $\sim$ 20 Milky Way sized objects (Benavides et al. 2020, Giocoli et al. 2008). In ILLUSTRIS simulations (Benavides et al. 2020), it is found that between 20 and 40 % of galaxies have fallen into massive clusters as a part of larger groups or galaxy associations. Most of those groups are poor, containing one bright galaxy and possibly a few low-mass companions, however, rich groups also have a noticeable contribution.

All of this hints to the large amount of substructure expected inside the cluster environment. The evidence for smaller groups and massive dark matter subhalos, contained within galaxy clusters has been found in observations by measuring positions and velocities of galaxies (e.g., see Iodice et al. 2019), with gravitational lensing (e.g., Natarajan et al. 2009) and with X-ray maps (e.g., Jauzac et al. 2016). Considering the large velocity dispersion of galaxies in galaxy clusters ($\sigma \simeq 500 - 1000 \mathrm{kms}^{-1}$), associations of galaxies are unlikely to form after the galaxies fall into the potential well of the cluster, they have to be accreted onto the cluster as a single unit, again indicating the importance of mergers with groups for cluster growth (Benavides et al. 2020).

Once the group of galaxies enters the galaxy cluster, it gets influenced by the cluster environment. It quickly evolves in phase space, making it difficult to detect in observations. The size and the velocity dispersion of the accreted groups double on time scales between 0.5 and 5 Gyr (Benavides et al. 2020), which is comparable to the dynamical time scale in galaxy clusters (Sarazin 1988). Furthermore, tidal forces near the cluster centre strip the halos of the in-falling groups very efficiently - most galaxies leave the host group halo as early as 0.5 Gyr after the pericentric passage. Hence, most of the massive substructures within the cluster environment are on their first infall into the cluster and are yet to pass the pericentre (Choque-Challapa et al. 2019).

Although I will mainly be using a simplified assumption of spherically symmetric clusters with constant dark matter profile, it is essential to keep the existence of massive substructures in mind, as they can have a strong influence on the evolution and properties of galaxies in the cluster environment. Groups of galaxies within galaxy clusters host much more suitable conditions for galaxy mergers than the global cluster environment with large velocity dispersion of galaxies. Even after the group gets dynamically hotter under the tidal effects of the cluster and even after it gets gravitationally unbound, velocity dispersion between the former group members is lower than between galaxies that are accreted separately (Benavides et al. 2020).

1.6 Cluster Galaxies

Galaxies in the cluster environment have considerably different properties than those in intermediately dense environments, between voids and clusters (i.e., *field galaxies*). 80 – 90% of galaxies in clusters are *early-type galaxies* (evolved elliptical and lenticular galaxies), much more than in the under-dense regions, where they constitute only 10 – 20% of all galaxies. Furthermore, cluster galaxies tend to be more massive than field galaxies. The morphological differences are a consequence of environmental effects, discussed in section 1.7 and further explored in chapter 4.

The brightest galaxy in a galaxy cluster is called the *brightest cluster galaxy* (BCG), which is a giant elliptical galaxy sitting at the bottom of the cluster potential well. Their special location makes BCGs statistically different from other cluster galaxies (*cluster satellites*); they tend to be very luminous and massive, with stellar mass between 10^{11} and $10^{12} M_{\odot}$, which is much more than expected from the mass function of cluster galaxies. Many BCGs have double or multiple nuclei (two or more surface brightness peaks in the central regions), indicating that the BCGs can grow with the accretion of other cluster galaxies that sink into the potential well via dynamical friction. The BCGs almost always host an AGN in radio mode (Cimatti et al. 2019). In Chapter 5, I often exclude BCGs from the analysis since they are statistically vastly different from massive satellite galaxies (e.g., they are much more likely to host an AGN).

1.7 Effects of Cluster Environment

The environment of galaxy clusters, with its deep gravitational potential and increased density of galaxies and gas, profoundly impacts the evolution of cluster galaxies. As the galaxies are moving through the relatively dense intracluster medium, they are exposed to *ram pressure*, which scales with the density of the intracluster medium ρ and with the velocity of the galaxy relative to the ICM v:

$$p = \rho v^2. \tag{1.12}$$

If the ram pressure is larger than the gravitational force of the galaxy on the gaseous disc (per unit area), the gas is removed from the galaxy in the process called *ram-pressure stripping*. The efficiency of ram pressure stripping increases with cluster mass (Koulouridis et al. 2018, Ehlert et al. 2015). We have direct observational evidence of ram-pressure stripping - long stripped tails of hot and cold gas have been found, trailing the cluster galaxies (e.g., Ehlert et al. 2013b).

Ram-pressure stripping can influence star formation rate and AGN activity in several ways. It can remove the hot gas from galaxies (or galaxy groups) during their first infall into the cluster, while the cold and dense gas clouds may remain bound within the galactic potential. When the galaxy approaches the increasingly pressurized cluster centre, the pressure (ram

pressure and static thermal pressure) may compress the remaining gas, leading to a short period of enhanced star formation ($\sim 10^7$yr). This mechanism can explain elevated levels of star formation in merging clusters and in the gas clouds drifting inside the nearby clusters (Evrard 1991, Bekki & Couch 2003). It is also theorized that ram pressure stripping can lead to the removal of angular momentum of gas clouds in the galaxy, funnelling the gas towards the galactic centre. This can lead to enhanced AGN activity, often observed in ram-pressure stripped galaxies (e.g., Poggianti et al. 2021). On the other hand, if the ram pressure is too strong, the galaxies eventually succumb to it and are quenched. It is also possible that the ram-pressure triggered AGN activity aids the suppression of star formation.

The gas does not have to be removed entirely for a galaxy to quench. The cluster environment may instead prevent the accretion of the hot halo gas onto cluster galaxies, causing the cold gas reservoir to be gradually depleted by star formation. This can happen, for example, when the hot halo gas of cluster galaxies is efficiently ram-pressure stripped. This set of models is broadly labelled as *strangulation*. Both ram-pressure stripping and strangulation cause the gas-rich disc galaxies to transform into red spheroidal galaxies, but they do so on different time scales. Whereas ram pressure stripping is expected to quench the galaxy abruptly after the infall, strangulation is a longer and more gradual process.

As shown in section 1.4, the inner cluster regions are densely packed with galaxies. While the high velocity dispersion prevents mergers, galaxies can still gravitationally interact during frequent flybys. This process, called *harassment*, can have a significant impact on cluster satellites. It can kinematically heat the galaxies, transforming disc galaxies into ellipticals (Moore et al. 1996), and can transport the gas to the centre of cluster galaxies, triggering central starbursts and AGN activity (see the introduction of Ehlert et al. 2014 and references therein). Tidal forces exerted on the galaxy during a close encounter can also remove matter from the galaxy in a process called *tidal stripping*.

Some studies suggest that the *cluster outskirts* are a much more suitable environment for AGN activity, compared to the inner cluster regions (an excess of AGNs on the cluster outskirts is reported for example in Koulouridis & Bartalucci 2019, Haines et al. 2012, Fassbender et al. 2012, Ruderman & Ebeling 2005). The galaxies on the outskirts more likely belong to the in-falling population that still possesses enough cold gas to fuel star formation and AGN activity. Furthermore, the velocity dispersion of galaxies on the cluster outskirts is lower compared to the inner regions, increasing the likelihood of mergers, which are thought to be an important (although not necessarily dominant) mechanism for AGN triggering (e.g., see Steinborn et al. 2018, Hernquist & Mihos 1995 and references therein). It is believed that the non-axisymmetric perturbations during mergers and galaxy interactions can induce mass inflows towards the galactic centre.

The galaxy environment can impact the AGN activity and (at least circumnuclear) star formation in a very similar way, since both are fueled by the same cold gas reservoir. The correlation between star formation and nuclear activity has been confirmed in several studies (e.g., Florez et al. 2020, Mullaney et al. 2012, Diamond-Stanic & Rieke 2012). However, this connection is still a topic of debate since AGN activity itself can efficiently quench the star formation rate in galaxies. Some studies thus favour the quenching role of AGNs (e.g., Leslie et al. 2016). This work will try to shed some light on the interplay between the cluster environment, AGN activity and star formation (see chapters 4 and 5).

Chapter 2

Simulations

2.1 Magneticum Pathfinder Simulations

In this work, I aim to investigate the AGN activity in galaxy clusters while also considering their large-scale neighbourhood. On the one hand, this requires a simulation of a large cosmological volume with a sufficiently high number of galaxy clusters. On the other hand, such simulation needs to include small-scale processes like star formation and AGN feedback and should have high enough resolution to describe the behaviour inside individual galaxies realistically. Both requirements are fulfilled by the *Magneticum Pathfinder* suite of cosmological hydrodynamical simulations[1]. The Magneticum suite includes several cosmological boxes, simulated with the Tree/SPH code GADGET-3, which is an improved version of GADGET-2 (Springel 2005, Springel et al. 2005b). It uses an improved Smoothed Particle Hydrodynamics (SPH) solver for the gas evolution (Beck et al. 2016) and includes a better treatment of viscosity (Dolag et al. 2005). The simulations also account for the gas cooling (Wiersma et al. 2009), star formation and stellar feedback processes (Springel et al. 2005a, Springel & Hernquist 2003), UV/X-ray background (after Haardt & Madau 2001), chemical enrichment (Tornatore et al. 2007, 2004) and thermal conduction (Arth et al. 2014). The cooling is included with the publicly available code CLOUDY (Ferland et al. 1998) and follows 11 chemical elements (H, He, C, N, O, Ne, Mg, Si, S, Ca, Fe). The simulations also follow the SMBH evolution and implement AGN feedback, based on the models from Springel et al. (2005a), Di Matteo et al. (2005) with some further improvements (see section 2.3). For a concise description of the simulations, refer to Dolag et al. (2016). Magneticum simulations assume the WMAP cosmology (Komatsu et al. 2009) with Hubble constant $H_0 = 70.4$, total matter density parameter $\Omega = 0.272$, baryonic fraction of 16.8 %, index of the primordial power spectrum $n = 0.963$, and normalization of the fluctuation amplitude $\sigma_8 = 0.809$.

The Magneticum suite encompasses simulations of several cosmological boxes with different resolutions. For the purpose of this work, I use the *hr* resolution run *box2b*, which spans over 640 comoving Mpc/h and contains $2 \cdot 2880^3$ particles. The mass of the dark matter

[1] Technical information about the *Magneticum* project is available at `www.magneticum.org`.

particles is $6.9 \cdot 10^8 M_\odot/h$ and the gas particles $1.4 \cdot 10^8 M_\odot/h$. The gas particles can also form stellar particles with $\sim 1/4$ of their mass. Softening lengths are $3.75\text{kpc}/h$ for dark matter and gas particles and $2\text{kpc}/h$ for stellar particles. In this work I analyse snapshots at two redshifts; I refer to $z = 0.25$ as *low redshift* and $z = 0.90$ as *high redshift*. In figure 2.1, the gas from box2b is visualized at low redshift, with colour representing the temperature.

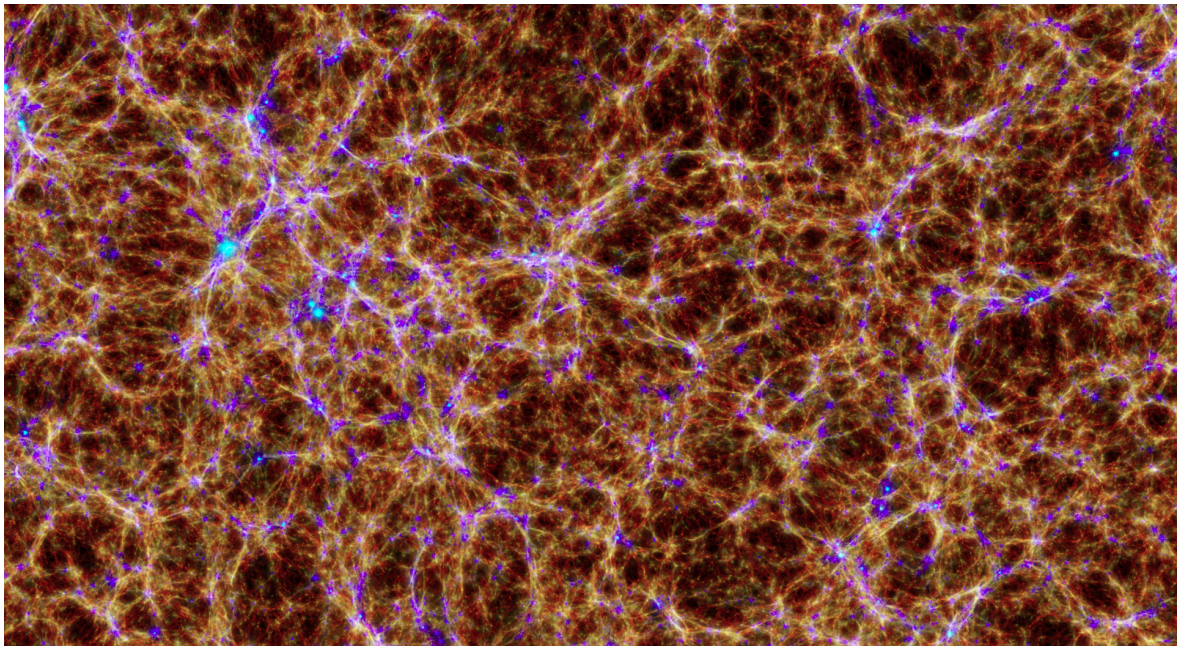

Figure 2.1: Visualization of a cutout of the box2b/hr from the Magneticum simulation set at $z = 0.2$. The long side the image, spans over the size of the box (640 comoving Mpc/h). The image depicts the gas, colour coded according to its temperature from cold/brown to hot/light blue, and the galaxies and stars, coloured in white. The image was rendered with SPLOTCH (Dolag et al. 2008) and is available at www.magneticum.org.

2.2 Subfind Algorithm

In order to investigate galaxies and galaxy clusters in the simulations, we first need reliably identify them in the simulation snapshots, which contain information about individual particles. This is done with the subhalo identifier SUBFIND (Springel et al. 2001), modified to treat the baryonic component (Dolag et al. 2009). Subfind uses the Friends-of-Friends (FOF) algorithm to connect particles into main groups (halos) based on some linking length. The main FOF groups can have several local density maxima, which are identified by varying the global density threshold until locally overdense regions disconnect. Each region is further subjected to a gravitational unbinding procedure that eliminates particles with positive energy, leaving only gravitationally bound subhalos, with their centre defined as the position of the most bound particle. Subfind-identified subhalos are used in this work as galaxy candidates, while galaxy clusters and groups are identified as the main FOF groups. Subfind can also identify substructures one level above subhalos; it can find galaxy groups with several galaxies embedded in the potential of the main FOF groups (used in section 4.1). Furthermore, Subfind calculates several properties, such as the stellar mass of galaxies and R_{500} and M_{500}

of clusters on the fly, based on particle properties and distribution. It should be stressed that Subfind has its limitations. It is possible that in some cases, parts of the galaxies get spuriously assigned to other structures (e.g., during a close encounter between two galaxies).

In the two snapshots of box2b used in this work, Subfind identifies around 56 000 groups with $M_{500} > 10^{13} M_{\odot}$ at low redshift (34 000 at high redshift) and around 2000 groups with $M_{500} > 10^{14} M_{\odot}$ at low redshift (around 500 at high redshift). Throughout this work I will refer to groups with $M_{500} > 10^{13} M_{\odot}$ as (*all*) *galaxy clusters*, and to groups with $M_{500} > 10^{14} M_{\odot}$ as *massive clusters*. Note that there are also a few very massive clusters with $M_{500} > 10^{15} M_{\odot}$, but they will not be considered separately in this work due to the small sample size.

2.3 SMBH Implementation

Implementation of SMBHs into large cosmological simulations seems like a particularly challenging task since the processes that govern black hole mass accretion and feedback take place in the proximity of a black hole, well below the scales we can hope to resolve in such simulations. On the other hand, an accurate black hole implementation is essential due to their immense impact on the surrounding cluster environment (see section 1.3 and Borgani & Kravtsov 2011 for a review). Luckily, it turns out that using a relatively simple subgrid model can achieve an accurate description of AGN feedback and black hole growth.

In Gadget-3 code, SMBHs are implemented according to Springel et al. (2005a) and Di Matteo et al. (2005), with added improvements by Fabjan et al. (2010) and Hirschmann et al. (2014). A concise description of the model together with further improvements is also given in Steinborn et al. (2015); however, they have not yet been implemented in box2b, used in this work. Black holes are seeded in all well-resolved galaxies above some stellar mass threshold. To identify suitable galaxies, FOF algorithm is performed on stellar particles, with a linking length of 0.05 times the mean separation of the DM particles, which is smaller than the linking length used to identify dark matter halos. This method ensures that the halos where black holes are seeded belong to well-resolved galaxies that have undergone sufficient star formation (Hirschmann et al. 2014). In the *hr* simulation used in this work, black holes are seeded in halos with the stellar mass around $10^{10} M_{\odot}$ at the position of stellar particles with the largest binding energy and are given the initial mass of $3.2 \cdot 10^{5} M_{\odot}$. In some simulations (and in the earlier version of Gadget (Springel et al. 2005a), black holes are pinned to the centre of the potential well, which ensures that they do not wander off due to numerical effects. This method has its shortcomings (e.g., if a large SPH kernel is used to scan for the particles with the deepest potential, black holes can spuriously jump to neighbouring massive galaxies). In this version of Gadget, black hole pinning is not required; black holes are kept in place by enforcing more strict momentum conservation in the implementation of gas accretion and black hole mergers. Furthermore, the additional dynamical friction force is

included when the resolution is not high enough for it to emerge naturally in the simulations (Hirschmann et al. 2014).

Black hole particles are implemented as sink particles with fundamental properties such as mass $M_\bullet$ and mass accretion rate $\dot{M}$. They grow by swallowing the surrounding gas, i.e., by deflating the gas particles in its proximity. This process is implemented in a stochastic way - each neighbouring gas particle contributes to accretion with some probability, which is proportional to the SPH kernel weight, calculated at the particle position. Each particle contributes to accretion only with a fraction of its mass, resulting in more continuous gas accretion [2] (refer to Fabjan et al. 2010 for a more detailed description).

In order to realistically describe the growth of black holes in the simulations, an accurate determination of the mass accretion rate $\dot{M}$ is of paramount importance. A common way of calculating the accretion rate is with the Bondi model, which assumes an isotropic and isothermal sphere of gas (Bondi 1952, and Springel et al. 2005a for its implementation in the simulations):

$$\dot{M}_{\mathrm{B}} = \frac{4\pi\alpha G^2 M_\bullet^2 \langle\rho\rangle}{\left(\langle c_{\mathrm{s}}\rangle^2 + \langle v\rangle^2\right)^{3/2}}, \tag{2.1}$$

where c_s is the sound speed of the accreted gas, ρ is the density, and v is the velocity of gas relative to the black hole. Brackets represent the kernel-weighted SPH averages. The boost factor α is added due to the limited resolution - the unresolved regions in the vicinity of the black hole are denser, yielding higher accretion rates than inferred from the smoothed SPH averages. α is usually set to 100 (Springel et al. 2005a). The black hole accretion rate is given by equation 2.1 and is limited by the Eddington accretion rate:

$$\dot{M}_{\mathrm{Edd}} = \frac{4\pi G M_\bullet m_{\mathrm{p}}}{\eta_r \sigma_{\mathrm{T}} c}, \tag{2.2}$$

which is defined so that the Eddington luminosity is equal to

$$L_{\mathrm{Edd}} = \eta_r \dot{M}_{\mathrm{Edd}} c^2, \tag{2.3}$$

which is the maximal luminosity that an object can have so that it remains gravitationally bound - it is the luminosity where the radiation pressure balances out the gravitational force (expressed for purely ionized hydrogen). σ_T is the Thomson scattering cross-section, and η_r is the radiative efficiency. In our simulations it is constant ($\eta_r = 0.2$). The ratio between $\dot{M}_\bullet$ and $\dot{M}_{\mathrm{Edd}}$ is called *Eddington ratio*. The accretion rate is then calculated:

$$\dot{M}_\bullet = \min\left(\dot{M}_B, \dot{M}_{\mathrm{Edd}}\right). \tag{2.4}$$

[2] This mechanism results in a change of the *dynamical* mass of the black hole particle. The actual black hole mass $M_\bullet$ used for calculating $\dot{M}$, can be followed analytically from $\dot{M}$ in a continuous way.

AGN feedback, the amount of energy released back into the surrounding gas (per unit time) is given by:

$$\dot{E}_{\rm feed} = \epsilon_r \epsilon_f \dot{M}_\bullet c^2, \tag{2.5}$$

where ϵ_f is the fraction of the released energy that is thermally coupled to the surrounding gas. Here, a distinction between radio and quasar mode is made: if the accretion rate is below 0.01 $\dot{M}_{\rm Edd}$, then $\epsilon_r = 0.2$ and if it is higher, then $\epsilon_r = 0.05$. This follows from the fact that in radio mode, most of the energy is released in a kinetic form and is thermalized in the surrounding gas, whereas in quasar mode, energy is mostly radiated away. Since the scales resolved in cosmological simulations are larger than those where kinetic feedback is expected to dominate, all energy is injected thermally into surrounding gas particles, selected with a spherical top-hat kernel, to provide a smooth distribution of energy (Fabjan et al. 2010).

The subgrid model used in our simulations still has some noteworthy shortcomings. It assumes the abrupt transition between radio and quasar mode, which is only a rough approximation to the smooth transition observed in nature. A more detailed model is suggested by Steinborn et al. (2015), where efficiencies are given as functions of $M_\bullet$ and $\dot{M}_\bullet$. Furthermore, purely thermal feedback currently implemented is not entirely accurate; it is speculated that a mechanical-momentum input from the AGNs could mend some of the observed inaccuracies, such as the overestimated massive end of the stellar mass function (Steinborn et al. 2015).

2.4 AGN Luminosity

In this work, I will focus on the environmental dependence of the black hole mass accretion rate $\dot{M}_\bullet$, since it is the fundamental quantity in determining the AGN activity. However, it is not very suitable for comparison with observations, where the principal quantity is AGN luminosity (X-ray luminosity in studies that I refer to in this work). In order to compare with observation, I first convert $\dot{M}_\bullet$ to bolometric luminosity L_{bol} with a simple model

$$L_{bol} = \epsilon_r \dot{M}_\bullet c^2, \tag{2.6}$$

where the efficiency ϵ_r is set to 0.1 (see Maio et al. 2013 and references therein). This can be further converted to X-ray luminosity by applying the bolometric corrections proposed by Marconi et al. (2004):

$$\begin{aligned} \log\left(\mathrm{L_{HXR}}/\mathrm{L}_{bol}\right) &= -1.54 - 0.24\mathcal{L} - 0.012\mathcal{L}^2 + 0.0015\mathcal{L}^3 \\ \log\left(\mathrm{L_{SXR}}/\mathrm{L}_{bol}\right) &= -1.65 - 0.22\mathcal{L} - 0.012\mathcal{L}^2 + 0.0015\mathcal{L}^3, \end{aligned} \tag{2.7}$$

where $\mathrm{L_{SXR}}$ refers to luminosity in *soft* X-ray band (0.5-2 keV) and $\mathrm{L_{HXR}}$ in *hard* X-ray band (2-10 keV). $\mathcal{L}$ is defined as

$$\mathcal{L} = \log\left(\mathrm{L}_{bol}/\mathrm{L}_\odot\right) - 12. \tag{2.8}$$

Correction is derived for the luminosity range $8.5 < \log(L_{bol}/L_\odot) < 13$ from the template spectra, with the aim of estimating the intrinsic luminosity (and not from the observed AGN spectra) which is closer to L_{bol} derived from $\dot{M}_\bullet$ in the simulations (see Marconi et al. 2004 and Biffi et al. 2018 for an overview). In this work I use the combined soft and hard X-ray bands (0.5-10 keV). Note that the energy range refers to rest-frame energies.

The model used for converting $\dot{M}_\bullet$ to X-ray luminosity is fairly simple and could be improved, for example, by considering different radiation regimes (radio and quasar mode, see sections 1.1 and 2.3). One such model, which accounts for the suppressed AGN emission at low Eddington ratios, is described in Churazov et al. (2005) (see also Steinborn et al. 2015). For an even more accurate comparison with observations, one could also use the virtual X-ray observatory PHOX (Biffi et al. 2018, 2013, 2012) to generate mock X-ray catalogues from the simulation output, which would also take into account effects like AGN obscuration and add contamination from other sources. This, however, is far beyond the scope of this work. The simple dependence of L_{bol} on $\dot{M}_\bullet$ (equation (2.6)) and the fact that the X-ray luminosity in equation (2.7) scales monotonically with L_{bol} (in the range used in this work), allows us to intuitively infer the underlying changes of the mass accretion rate from X-ray luminosity. This is essential since the mass accretion rate directly reflects the environmental effects I want to explore in this work.

2.5 Stellar Mass

Stellar mass of galaxies M_* is calculated with Subfind (section 2.2) from stellar particles bound to the identified subhalos. In this work, I split galaxies based on their stellar mass into two classes. I refer to galaxies with $10.15 < \log M_*(M_\odot) < 11$ as *low-mass* galaxies, and to galaxies with $\log M_*(M_\odot) > 11$ as *massive* galaxies. In some cases, I also plot *all* galaxies ($\log M_*(M_\odot) > 10.15$), a sample dominated by much more abundant low-mass galaxies.

Considering massive galaxies separately from low-mass galaxies is essential for several reasons. *(i)* Massive galaxies display distinctively different properties and are affected by the environment in profoundly different ways than the low-mass population (see chapters 4 and 5). *(ii)* Observations face magnitude limitations, and to avoid the incompleteness of the sample, a high brightness cut is often used for selection (table 5.1). Furthermore, since the stellar masses in our simulations tend to be overestimated (Steinborn et al. 2015), it might be meaningful to use massive galaxies for comparison with observations. *(iii)* Due to the resolution limitations of the simulations, massive galaxies may have more realistic properties than low-mass galaxies. At $\log M_*(M_\odot) \approx 10.15$[3], black holes are seeded, causing the abrupt and unrealistically high AGN activity, which affects the distribution and properties of galaxies. Thus, higher stellar mass limits are usually chosen when investigating galaxies in

[3] $\log M_*(M_\odot) = 10.15$ roughly corresponds to $10^{10} M_\odot/h$.

box2b (e.g., in Steinborn et al. 2018 they use galaxies with $\log M_*(M_\odot) > 11$, and in Lotz et al. 2021 they use $\log M_*(M_\odot) > 10.85$). Nonetheless, this work is not restricted to the analysis of massive galaxies, since low-mass galaxies can still provide a unique insight into the environmental effects on AGN activity, despite being less realistic.

2.6 Star Formation Rate

Star formation rate (SFR) measures the the total mass of stars in a galaxy formed per year (in $M_\odot/\mathrm{yr}$). In this work, the star formation rate is given as the total star formation rate of all particles belonging to a subhalo and is calculated with Subfind. According to the star formation rate, galaxies are usually divided into *star-forming* and *quiescent* population. This can be done, for example, by using the so-called "blueness criterion" (Franx et al. 2008), in which the star-forming population satisfies the following condition:

$$\mathrm{sSFR} \cdot t_h > 0.3, \tag{2.9}$$

where sSFR is the *specific star formation rate*; star formation rate per unit of stellar mass, and t_h is the Hubble time at some redshift. The criterion is time-dependent and can be used even for higher redshifts (although time dependence does not make a significant difference between $z = 0.25$ and $z = 0.90$). Using sSFR in place of SFR is reasonable since massive galaxies contain more gas that can be converted into stars.

In this work, however, I choose a different criterion. Subfind is only able to resolve SFR larger than $0.02 M_\odot/\mathrm{yr}$; all galaxies with a lower star formation rate have SFR $\equiv 0$ in the Subfind snapshots. In the following sections I divide those galaxies into those with SFR = 0 (henceforth called *quiescent* population and those with SFR > 0 (henceforth called *star-forming* population) in the Subfind snapshots. This definition is primarily used for convenience: the population with SFR = 0 cannot be used in plots, where SFR dependence is shown and has to be considered separately. Secondly, most low-mass star-forming galaxies (according to equation (2.9)) lie on the star-forming main sequence (see chapter 4), and are identified as star-forming by both criteria. Similarly, most of the quiescent galaxies have SFR = 0. I explicitly verified that both criteria produce qualitatively similar results.

Classification is not equivalent anymore in massive galaxies, which tend to have lower sSFR, possibly falling below the "blueness" limit (equation 2.9), but still having non-zero SFR. The number of massive star-forming galaxies (according to equation (2.9)) is so low that they are meaningless to consider separately due to statistical noise. The SFR $> 0.02 M_\odot/\mathrm{yr}$ criterion does a better job at splitting the galaxies into two sufficiently populated categories with different levels of star formation.

2.7 Distance to the Nearest Neighbour

This work will also focus on the effects of the *local density* of galaxies, which is usually measured in two different ways. We can either use a fixed aperture and count galaxies in the predefined vicinity of the galaxy, or we can use the distance to the nearest $n-$th neighbour as a proxy (e.g., Hwang et al. 2019). I decided for the latter since it is believed to be particularly suitable for identifying local structures and over-densities inside larger structures (Muldrew et al. 2012). In this work, I define the distance to the nearest neighbour d_n as the distance of one galaxy to its nearest massive neighbouring galaxy (with $\log M_*(M_\odot) > 10.15$). By using the *first* nearest galaxy to define d_n, I also identify galaxies in the immediate proximity of another galaxy, possibly undergoing a strong gravitational interaction. The distance d_n is given as a proper distance in kpc.

Chapter 3

Large-scale Surroundings of Galaxy Clusters

3.1 Distances Between Clusters

This work will focus mainly on the radial profiles of AGN activity and star formation rate in galaxy clusters. Since galaxy clusters are not in isolation but are embedded into the global large-scale environment, it is essential to explore the effects of the neighbouring clusters on the radial profiles. If clusters were distributed uniformly in the Universe, any significant overlaps between profiles of different clusters could be neglected (as will be shown later in the section). However, if the positions of clusters in the simulation are compared to the uniform random distribution (figure 3.1), it is evident that this is not the case. The cosmic web features dense associations of cluster halos, concentrated between cosmic voids (see section 1.2). This can decrease the expected distances between clusters and, in turn, impact the radial profiles.

To verify this formally, we define the *two-point correlation function* $\xi(r)$[1] (Peebles 1980):

$$\mathrm{d}\mathcal{P} = n\,(1 + \xi(r))\,\mathrm{d}V, \tag{3.1}$$

where n is the mean number density of objects (in this case, cluster halos) and $\mathrm{d}\mathcal{P}$ is the probability that the volume $\mathrm{d}V$ at a distance r from a cluster contains another cluster. $\xi(r) = 0$ implies uniform distribution of clusters, with no correlation between their positions. $\xi(r)$ is usually parameterized as a power law:

$$\xi(r) = \left(\frac{r}{r_0}\right)^{-\gamma}. \tag{3.2}$$

In order to evaluate how a cluster is disturbed by its neighbours, we are interested in the *probability that the closest neighbour is at a distance* r. This can be obtained by multiplying

[1] In this section, r denotes the comoving distance in Mpc/h and not relative to R_{500} as defined in other sections.

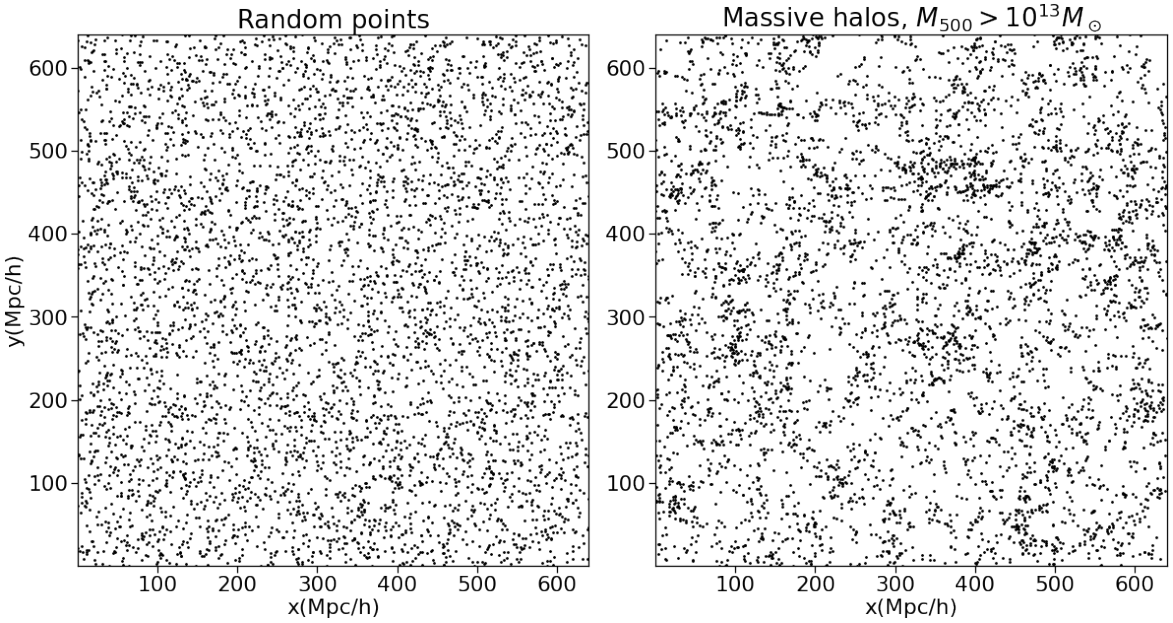

Figure 3.1: Comoving coordinates of halos with $M_{500} > 10^{13} M_\odot$ in box2b at $z = 0.25$ (right panel), and positions of the same number of points, uniformly randomly distributed over the same volume. The depth of the displayed volume is 100 comoving Mpc/h.

the probability that no cluster is found closer than r and that there is a cluster in the interval $[r, r + \mathrm{d}r]$.

In order to obtain the probability that no cluster is found within some finite volume V', we might be tempted to integrate equation 3.1 over the volume V', but we cannot do that since equation (3.1) only holds in the differential form. To demonstrate why, imagine a uniform probability density, with $\mathrm{d}\mathcal{P} = n\mathrm{d}V$. Integrating over the entire volume containing all of the objects, we find that the total probability $\mathcal{P}$ is equal to the number of objects and thus larger than 1. However, equation (3.1) can be integrated if the volume contains only one object. Considering uniform distribution, we correctly obtain the probability that the object is found within V': $\mathcal{P} = V'/V$, where V is the total volume where the object can be found (in our case, the volume of the cosmological box). This can be generalized by using equations (3.1) and (3.2). The probability that *one particular* cluster is found closer than r from some other cluster is obtained by setting $n = 1/V$ and integrating equation (3.1):

$$\mathcal{P}_{single}(r) = \frac{1}{V}\int_0^r \left(1 + \left(\frac{r'}{r_0}\right)^{-\gamma}\right) 4\pi r'^2 \mathrm{d}r' = \frac{4\pi r^3}{3V}\left(1 + \frac{3\left(\frac{r}{r_0}\right)^{-\gamma}}{3-\gamma}\right) \tag{3.3}$$

The probability of finding several objects (or no objects) closer than r can then be calculated with the binomial probability mass function (equation (A.14))[2]. Note that this directly contradicts the assumption, that the positions of *all* clusters are correlated according

[2]The Poisson distribution would be a better choice since it does not constrain the total number of clusters. However, the considered volumes V' are much smaller than the total box volume V, and the binomial and the Poisson approach are equivalent.

to equation (3.1). By using binomial statistics, it is assumed that the clusters are correlated only with the position of the central cluster (and distance r). Nonetheless, the simple analytical formula obtained with this simplification proves to be a relatively good approximation. After deriving equation (3.3), the probability of finding *no* objects closer than r is equal to the probability of not finding *one particular* object closer than r, to the power of the total number of objects N. Multiplying with the probability that an object is found in the interval $[r, r+\mathrm{d}r]$ (equation (3.1)), we can then obtain the probability density function that the closest neighbouring object is at a distance r:

$$\frac{\mathrm{d}\mathcal{P}}{\mathrm{d}r}(r) = \frac{4\pi r^2 N}{V}\left(1 - \frac{4\pi r^3}{3V}\left(1 + \frac{3\left(\frac{r}{r_0}\right)^{-\gamma}}{3-\gamma}\right)\right)^N . \tag{3.4}$$

I estimated the two-point correlation function of clusters with $M_{500} > 10^{13} M_\odot$ in box2b by using the estimator from Landy & Szalay (1993) and comparing the distances between clusters with random uniform distribution of points. By fitting the power-law (equation 3.2) to the estimated two-point correlation function at different r, I obtain $\gamma = 1.65 \pm 0.02$ and $r_0 = 9.35 \pm 0.05\mathrm{Mpc}/h$ at redshift 0.25 and $\gamma = 1.77 \pm 0.02$ and $r_0 = 10.67 \pm 0.08\mathrm{Mpc}/h$ at redshift 0.9 (errors are statistical errors of the fit). The powers γ are in the 1.6-2 range reported in the literature (see Basilakos & Plionis 2004 and references therein). The range of $3\mathrm{Mpc}/h < r < 15\mathrm{Mpc}/h$ was used for fitting to exclude small, non-linear scales where the two-point correlation function decreased rapidly and deviated from the power-law behaviour. The estimated $\xi(r)$ at low and high redshift and the corresponding power-law fits are shown in figure 3.2. It can be seen that the power-law model describes the cluster correlation function well down to $\sim 2R_{500}$ at low and high redshift. It is also intuitively clear why it is not expected to hold down to $r = 0$; if the two clusters had formed very close to each other, they are likely to have merged. Hence the rapid drop of $\xi(r)$ in the cluster centre. I tried to account for this behaviour by introducing a cutoff in the probability ($\xi(r) \to -\infty$) at low r, but that did not alter the conclusions; hence I am not showing it explicitly.

In figure 3.3 the probability density function for the distance to the nearest neighbouring cluster, obtained with the two-point correlation function (equation (3.4)), is plotted against the actual distribution of distances to the nearest neighbouring cluster in box2b. The histograms generally agree with predictions of the two-point correlation function despite the inaccurate assumptions; however, there are some notable differences. Equation (3.4) overestimates the number of clusters very close to their neighbours, possibly due to the rapid decline of $\xi(r)$ at small r (see the previous paragraph). Introducing a probability cutoff at low r could to some degree fix this discrepancy. Furthermore, equation (3.4) underestimates the number of clusters in isolation (with the closest neighbour further than 10 Mpc/h away). This might be a consequence of the inaccurate assumption of independence of the positions of the neighbours. To illustrate why, imagine that we measure the position of all but one cluster, and find that they are all far away from the central cluster. That means that the central cluster is in a

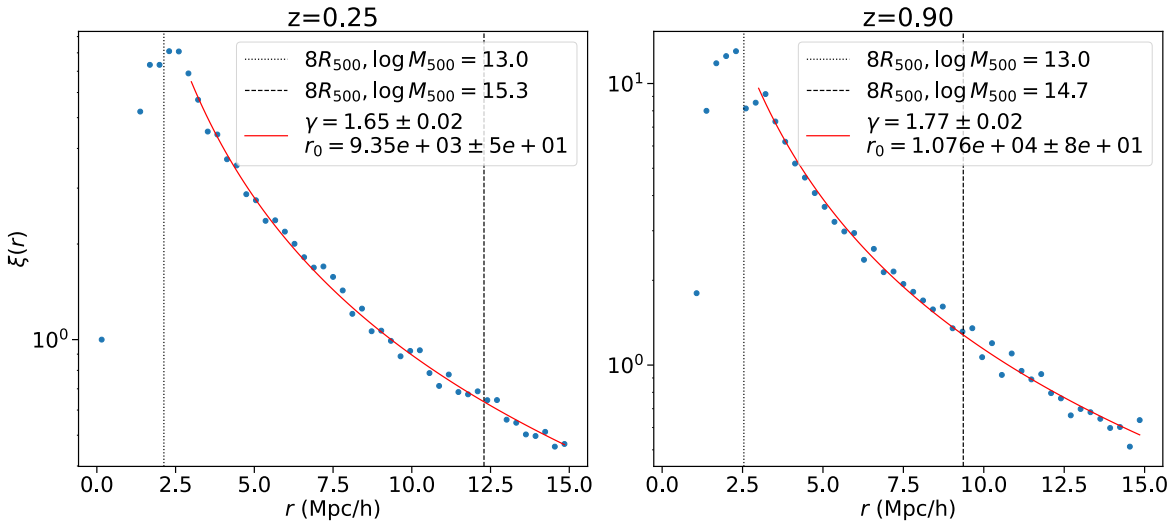

Figure 3.2: Two-point correlation function ξ as a function of the comoving distance r at low redshift (left panel) and high redshift (right panel). The data points represent the two-point correlation function obtained with the estimator from Landy & Szalay (1993). Solid lines represent the power-law model fit (equation (3.2)), with parameter values printed out in the legend. The dotted line represents the $8R_{500}$ of the least massive selected cluster (at the selection limit $10^{13} M_{\odot}$) and the dashed line of the most massive cluster at each redshift. Those distances correspond to the ranges of the radial profiles, shown in chapters 4 and 5.

particularly under-dense region and that the last unknown cluster is probably also far away, closer to other associations of clusters. However, following our assumption of independence, we expect it to be closer, hence the lack of isolated clusters in our model. However, even taking this into account, using the two-point correlation function alone may not be enough since it cannot completely describe the evolved density field in the late Universe, traced by the positions of galaxy clusters in the simulations (Peebles 1980). The contribution of higher order moments should also be considered.

In terms of the redshift evolution, I find that the power-law fit, shown in figure 3.2, yields a similar index γ at both redshifts; at high redshift, γ is even slightly larger, indicating a higher degree of clustering. However, the expected distances to the nearest neighbouring clusters are smaller at low redshift, as can be seen in figure 3.3, due to the overall increase in the number density of clusters. Since the structures grow, the number of clusters above $10^{13} M_{\odot}$ is much larger at low redshift (see section 2.2).

The key takeaway from this section and figure 3.3 is, that in the highly clustered environment of the cosmic web, clusters are expected to have their neighbours significantly closer compared to the uniform distribution. In figure 3.3 I show the distances $8R_{500}$ from the least massive and most massive clusters at low redshift, which is approximately the radial range used later in chapters 4 and 5 (figures 4.7, 5.18 and 5.20). Figure 3.3 demonstrates that even the profiles of smaller clusters may be potentially influenced by another cluster (the probability would be negligible in the case of uniform cluster distribution). The influence is even larger in massive clusters that almost certainly contain another cluster in their vicinity, most likely only a few

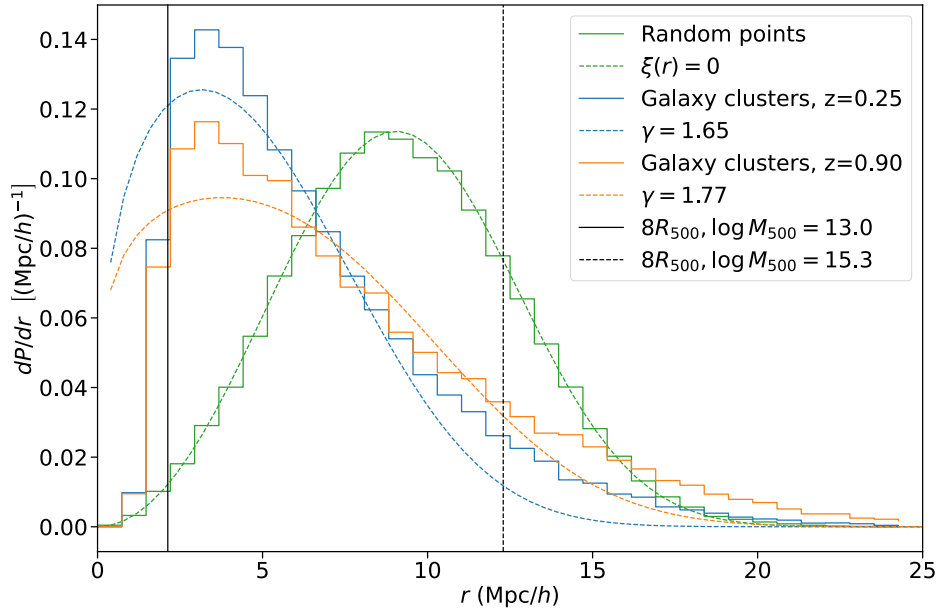

Figure 3.3: Probability of finding the nearest neighbouring cluster at a distance r, as a function of comoving distance in Mpc/h. The histograms (solid lines) represent the distribution of the distances to the nearest neighbour in box2b at low redshift (in blue), high redshift (in orange), and for the random uniform distribution with the number of points equal to the number of clusters at low redshift, distributed over the same volume (in green). Dashed lines represent the prediction from the measured two-point correlation functions (equation (3.4)). I also show the $8R_{500}$ radius of the least massive and most massive cluster in the box at $z = 0.25$.

R_{500} away. The expected impact of such overlaps will be thoroughly discussed in the next section.

3.2 Overlapping and Remote Regions

In order to disentangle the contribution of the neighbouring clusters from other features found in the extended cluster regions, I divide galaxies into two populations. The *overlapping* population comprises the galaxies with some neighbouring cluster closer than the overlapping distance r_{ov}. Any other galaxy, which is only close to the central cluster, belongs to the *remote* population. In figure 3.4 I demonstrate how both populations are defined in the profiles of 3 different clusters. In this work, a relatively large value of $r_{ov} = 6R_{500}$ is chosen, which ensures that the remote regions are sufficiently far away from any neighbouring cluster regions. In figure 3.4, it can be seen that the profiles of smaller halos on the outskirts of massive clusters do not contain any remote regions. Despite the large r_{ov}, this method divides galaxies into two sufficiently large populations for meaningful comparison. Note that since the profiles of different clusters overlap, some galaxies may be considered multiple times. In some profiles, they may belong to the overlapping population, while in others, they may belong to the remote population (see figure 3.4).

To get some idea about how the neighbouring clusters influence the radial profiles, imagine the following simple case. Say that every cluster has an identical radial profile and that the

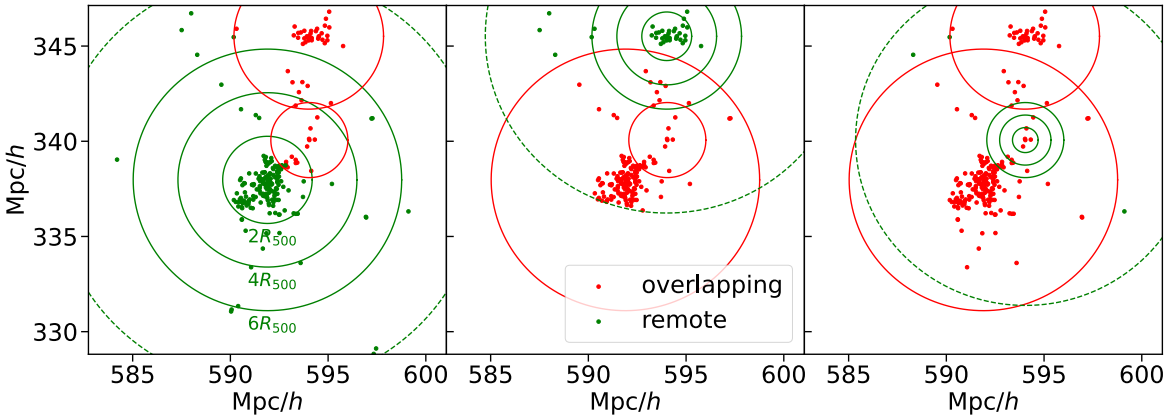

Figure 3.4: Comoving positions of galaxies in 3 clusters (groups) at redshift 0.25. The depth of the displayed volume is 2 comoving Mpc/h. In each panel, the definitions of the overlapping (red) and the remote (green) regions are depicted in the profile of each cluster (marked with green circles). Red circles represent $r_{ov} = 6R_{500}$ of the neighbouring clusters. Green circles represent $2R_{500}, 4R_{500}$ and $6R_{500}$ of the main cluster. Dashed circles represent the regions from which the galaxies of each cluster profile were read. They are large enough not to affect the 3D and 2D projected radial profiles in this work, and are defined solely for practical purposes with no physical meaning.

property $p(r)$ of each cluster galaxy depends only on the distance r (in R_{500}) to its "parent" cluster. Now imagine that several clusters are brought together to overlap, but their profiles remain the same (every galaxy still belongs to its parent cluster). The average property $\langle p \rangle$ of galaxies at position i is calculated by summing the contributions of the neighbouring clusters. Each cluster j at a distance r_{ij} from position i contributes the number of galaxies, given by the NFW number density $\mathrm{d}N/\mathrm{d}V$ (equation (1.11)), with properties $p(r_{ij})$. In other words, $\langle p \rangle$ at position i is calculated as the average of the profiles $p(r_{ij})$ of different clusters, weighted by their number density. In this work, we will not be interested in the average $\langle p \rangle$ at a single point j, but in the average $\langle p \rangle$ in the *radial shells* at a distance r from the centre of the cluster. This can be done as follows:

$$\langle p \rangle = \frac{\sum_i \sum_j p(r_{ij}) \frac{\mathrm{d}N}{\mathrm{d}V}(r_{ij})}{\sum_i \sum_j \frac{\mathrm{d}N}{\mathrm{d}V}(r_{ij})}. \tag{3.5}$$

The sum in equation (3.5) runs over all points i in the radial shells at some distance r, and at each point, over the contributions of all clusters j. Number densities are given by equation (1.7), with NFW parameters from table B.1. If the radial dependence of the property p in a single galaxy cluster is known, equation (3.5) can be used to estimate how the profile would look like in the large-scale environment when influenced by the identical profiles of the neighbouring clusters. Equation (3.5) can be evaluated with Monte Carlo integration; by generating a set of uniformly distributed random points j a distance r from the clusters in the simulation box. While equation (3.5) can be used for the profile of any property p, it is already instructive to define:

$$p(r) = r. \tag{3.6}$$

The average $\langle p \rangle \equiv \langle r \rangle$, obtained with equation (3.5), can be interpreted as a characteristic clustercentric distance of galaxies at distance r. It tells us, what is the expected distance of galaxies at the distance r from the *central* cluster, to *any* (central or neighbouring) cluster. If a cluster is in complete isolation, that means that $\langle r \rangle = r$; all galaxies belong to the central cluster and have properties characteristic of the distance r. However, if a cluster is surrounded by other clusters, the $\langle r \rangle$ decreases; some galaxies may belong to the the inner regions of the neighbouring clusters, with properties, characteristic of low r.

Characteristic distance $\langle r \rangle$ as a function of r is plotted in figure 3.5, where I separately plot the contributions of the main cluster (for which the profile is calculated) and of the neighbouring clusters. As the number density of the central cluster decreases in the outer regions, and as the number of neighbouring clusters rises (due to larger volume and increasing two-point correlation function, see section 3.1), the deviations of the combined profile from the main cluster profile become evident. Furthermore, if only the overlapping regions are shown, this transition from the main cluster dominating the inner regions to the significant contribution of neighbours at large r, appears as a peak; galaxies between 3 and 4 R_{500} have, on average, the highest $\langle r \rangle$, i.e., are on average the furthest away from any cluster. The exact position of the peak depends on the definition of the overlapping regions (r_{ov}); however, tentative signs of this behaviour are also noticeable in the combined profile of all regions. This peak has an interesting implication. If some property has a distinctively lower value in the inner cluster regions (e.g., the fraction of star-forming galaxies, as will be shown in Chapter 4), this may appear as a peak on the cluster outskirts, simply because the galaxies are the furthest away from any cluster regions. This peak is a pure consequence of geometrically overlapping cluster regions and does not necessarily imply any physical increase on the cluster outskirts. The importance of this will be demonstrated in Chapters 4 and 5. Note that figure 3.1 is meant only as a proof of concept. Profiles of other quantities $p(r)$ with different r dependence may have different overall shapes and positions of the peak and should be compared to figure 3.1 with caution.

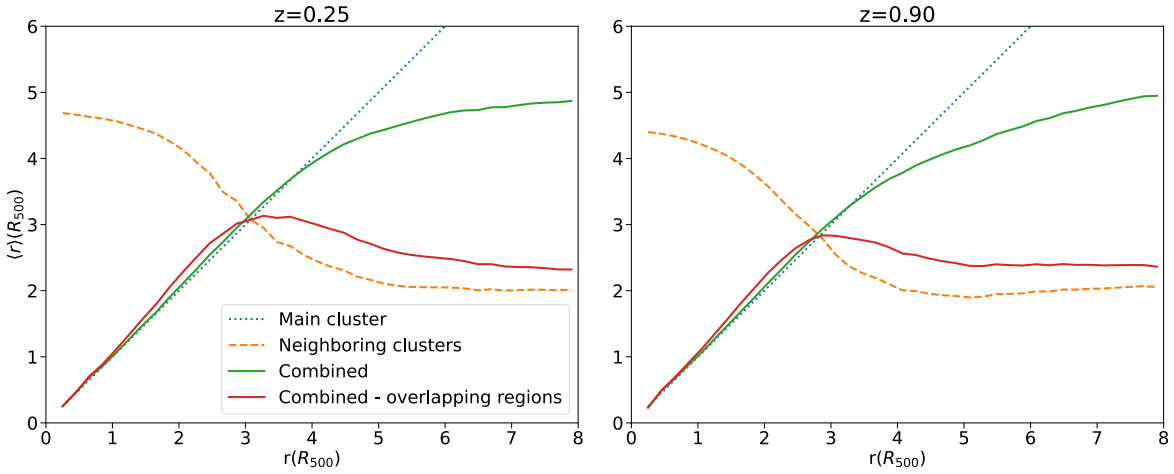

Figure 3.5: Radial profiles of the characteristic distance $\langle r \rangle$, defined with equations (3.6) and (3.5) by using groups with $M_{500} > 10^{13} M_{\odot}$ at redshifts 0.25 and 0.90. I separately show the contributions of the central (main) cluster and the neighbouring clusters. I also plot the profile in the overlapping regions ($r_{ov} = 6R_{500}$).

Chapter 4

Distribution and Properties of galaxies

In this section, I explore the distributions and properties of different populations of galaxies. This is particularly important for understanding the AGN activity since the properties of AGNs are correlated with the properties of their host galaxies. It is also instrumental for understanding which galaxies dominate a certain sub-sample. Several trends are shown in an illustrative manner, some of them are a consequence of already known physical processes, and some of them a consequence of numerical limitations.

When showing the galaxy distributions (e.g., figures 4.2 and 4.3), I normalize each plot (or panel in 2D histograms) to the size of the selected sample - which can vary significantly. Since I am not interested in the number of galaxies but rather only in their relative distribution, I omit the scale altogether. Some galaxies may be found in the vicinity of several neighbouring clusters (see chapter 3) - in the plots with r (e.g., figure 4.2) or M_{500} (e.g., figure 4.12), one galaxy can thus be considered multiple times, whereas in other plots, I only consider each galaxy once.

4.1 Substructure

Before discussing the properties of galaxies, let me first comment on another subject that will become important in the following sections. In section 1.5 I discuss the abundance of substructures that emerges from the hierarchical assembly of galaxy cluster halos. We can briefly investigate how the galaxies inside the cluster environment are distributed - how many and which galaxies belong to some smaller groups that are falling into the cluster, and which galaxies belong to the cluster itself. This is not difficult to check in our simulations since the Subfind algorithm identifies galaxies belonging to smaller groups contained within the main FOF groups (cluster halos). In the following chapters, I split galaxies into *group satellites*, which are part of subgroups containing at least 2 galaxies with $\log M_*(M_\odot) > 10.15$, and *isolated satellites*, which belong directly to the main cluster halos. The Subfind identification of subgroups is not sufficient anymore for such classification above the virial radius since not all galaxies there are a part of the cluster FOF group. Outer cluster regions may contain other

groups of galaxies that will be counted as the main FOF groups by Subfind, separate from the galaxy cluster. To obtain meaningful results, I refer to galaxies within the FOF groups containing at least 2 galaxies ($\log M_*(M_\odot) > 10.15$) as group satellites as well. In the outer regions, the meaning of those groups is thus different than in the inner regions since massive groups can be included, some of which even with $M_{500} > 10^{13} M_\odot$. I thus mostly restrict the use of the substructure classification to the inner cluster regions; for outer regions and the large-scale environment, I instead define the remote and overlapping regions, as outlined in chapter 3.

In figure 4.1 I plot the ratio between the number of group satellites and isolated satellites as a function of the radial distance r, distance to the nearest neighbouring galaxy (with $\log M_*(M_\odot) > 10.15$) d_n, host cluster mass M_{500} and stellar mass of the galaxy M_*. Some of the displayed trends are not surprising. Galaxies which are very close (small d_n) most likely belong to the same group (top right panel). If d_n is very large, of the order of Mpc, the fraction of group satellites again increases - this reflects the effects of massive FOF groups found on the outskirts of clusters; if they are excluded, this trend disappears. We can also clearly see how massive clusters contain overall a more considerable amount of substructure than their less massive counterparts (bottom left panel). This follows directly from the fact that hierarchical assembly is self-similar and that the merger mass ratio is approximately constant (section 1.5) - a larger cluster halo means larger accreted groups containing more galaxies. On the bottom right panel, a dramatic increase in the fraction of group satellites with stellar mass is shown. Very massive galaxies ($\log M_*(M_\odot) \gtrsim 11.5$) are most probably a part of their own smaller groups within the cluster environment, also containing other galaxies. This has further implications - since the massive groups only survive until the first pericentric passage (Choque-Challapa et al. 2019), most of the very massive galaxies are on their first infall into the cluster. Since massive galaxies are more likely embedded in smaller groups, they are worse tracers of the central cluster's dark matter profile than low-mass galaxies. This is also shown in appendix B. Regarding the radial dependence of the ratio (upper left panel), we can notice a significant decline in the fraction of group satellites in the centre of the cluster. Galaxies below $0.5 R_{500}$ most likely belong to the central cluster halo and not other subgroups. This is probably due to the larger number density of galaxies belonging to the central cluster (see section 1.4) and the fact that the groups of galaxies get unbound due to tidal forces in the centre of the cluster. The contribution of the latter cannot be estimated from figure 4.1 alone.

4.2 Local Density

The local density of galaxies (and the distance to the nearest neighbour d_n, which is used as a proxy) is expected to be highly correlated with the clustercentric distance r, since the number density of galaxies increases towards the cluster centre. Hence, merely observing the d_n is not sufficient to distinguish the effects of galaxy-galaxy interactions from the effects of the global cluster environment; it is essential to study the effect of d_n at a fixed distance r. In

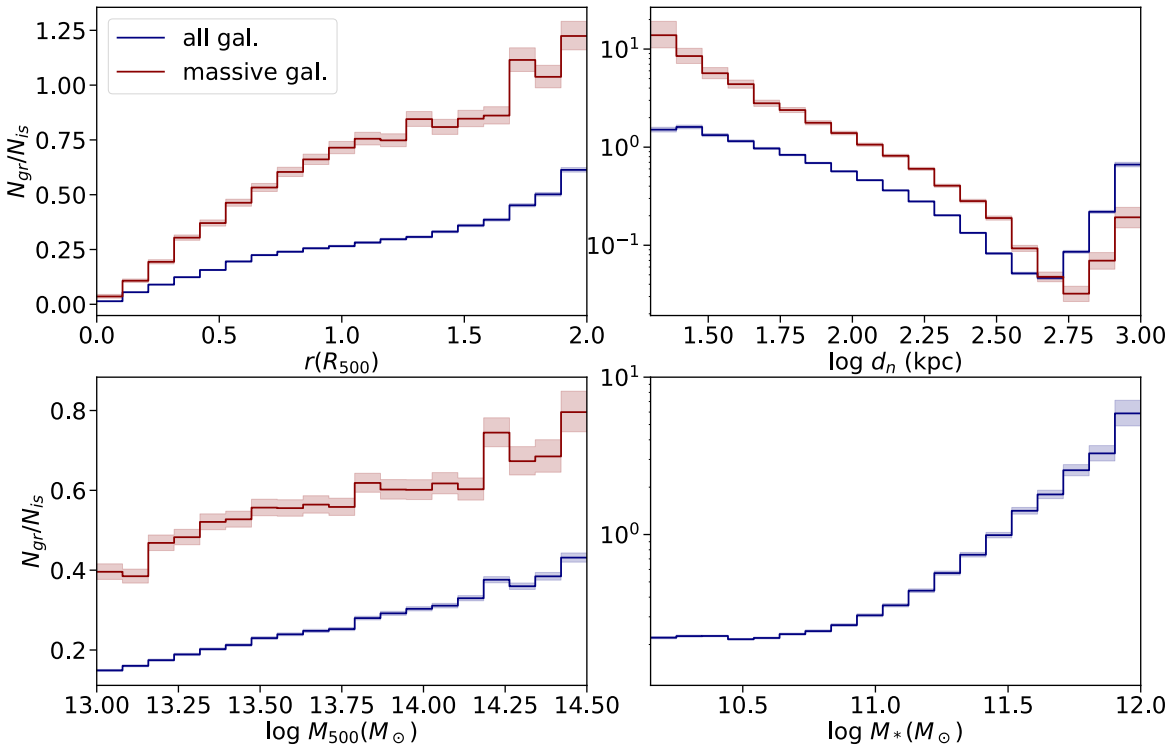

Figure 4.1: The ratio between the number of group satellites (which belong to smaller groups contained within the cluster environment) and the number of isolated satellites (belonging directly to the central cluster halo) as a function of radial distance r, distance to the nearest neighbour d_n, the mass of the parent cluster M_{500} and stellar mass M_*. The plots are shown for all galaxies ($\log M_*(M_\odot) > 10.15$) and massive galaxies ($\log M_*(M_\odot) > 11$, see section 2.5). Inner cluster regions (up to $2R_{500}$) were considered, and the BCGs of the main clusters were excluded. 68% Poisson confidence intervals are shown, see section A.1. Note that the y axis on the right panels is in logarithmic scale.

figure 4.2, I plot the distribution of d_n and r of galaxies in the inner cluster regions at different redshifts and for different galaxy populations. As expected, we can see a close relation between the radius r and the expected distance of a galaxy to its nearest neighbour. The correlation holds down to very small distances in the centre (tens of kpc). Some populations of galaxies, however, depart from this relation and are more likely to be located in a locally denser environment. This is even better demonstrated in figure 4.3, where I plot the d_n distribution of galaxies in two narrow radial shells; the one on the left panel is in the inner cluster regions ($\sim 0.3R_{500}$) and the one on the right panel in remote regions far from any clusters (i.e., in the field, $\sim 6R_{500}$). We can notice that in the clusters, star-forming galaxies prefer a locally denser environment (at some constant r), while star-forming galaxies in the field prefer to be in isolation. This will be again discussed and explained in section 4.5. Massive galaxies generally prefer a locally denser environment, perhaps reflecting their tendency to be in smaller groups along with several galaxies, especially if massive clusters are considered (see section 4.1).

From the redshift dependence of the d_n distribution in figure 4.3 we can see the overall decline in the number density with time in both cluster regions and in the field. Several

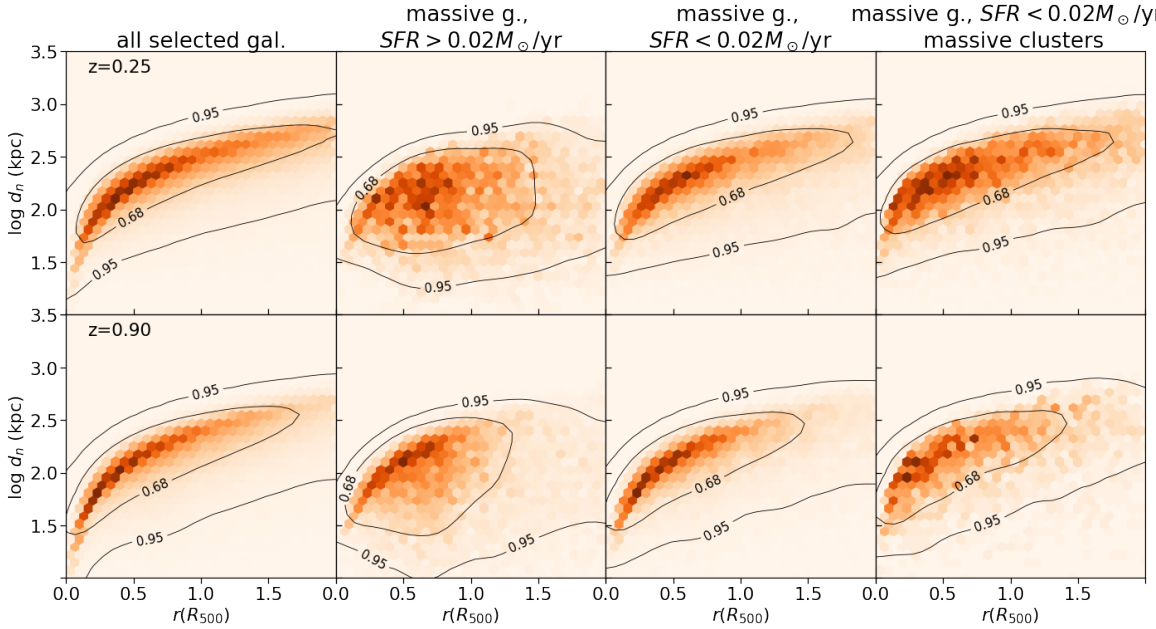

Figure 4.2: Distribution of distances to the nearest neighbour d_n and the clustercentric distances r of the galaxies in the inner cluster regions. Results are plotted for low redshift (upper panels) and high redshift (bottom panels), for all galaxies (low-mass and massive), massive star-forming galaxies, massive quiescent galaxies and massive quiescent galaxies in massive clusters. Contours show the positions of 68% and 95% of galaxies for clarity.

factors may play a role. On the one hand, the Universe expands, and the mean physical distances between objects increase, affecting the mean number density. On the other hand, as the galaxies grow in stellar mass, the number of galaxies above the threshold M_* increases in both clusters and the field (e.g. Torrey et al. 2015). Furthermore, since the size R_{500} of clusters is defined with respect to the critical density of the Universe, which falls off with time, the cluster regions, defined relative to R_{500}, are denser at high redshift (Poggianti et al. 2010). By counting the galaxies in box2b and accounting for the expansion of the Universe, I find that the mean number density of galaxies decreases by two-thirds between redshift 0.90 and 0.25. The mean number density in the inner cluster regions ($r < 4R_{500}$) declines even more drastically, to less than a quarter of the high redshift value. The same factor can be obtained from NFW fit parameters, shown in Appendix B. I also find that the mean number density of cluster regions is around 60 times higher than the box average at low redshift, and 87 times higher at high redshift.

4.3 Radial Distribution

In figure 4.4 I show the radial distribution of star-forming, massive and all selected galaxies. Star-forming galaxies are more likely to be found further away from the cluster's centre, compared to other galaxies, due to the central suppression of star formation (see section 2.6). The distribution of massive galaxies is slightly more peaked, with relative overdensity around $r = 0.6R_{500}$. They are less likely to be found further or closer to the centre (with the exception of the BCGs). In Appendix B I show that massive galaxies cannot be described well with the

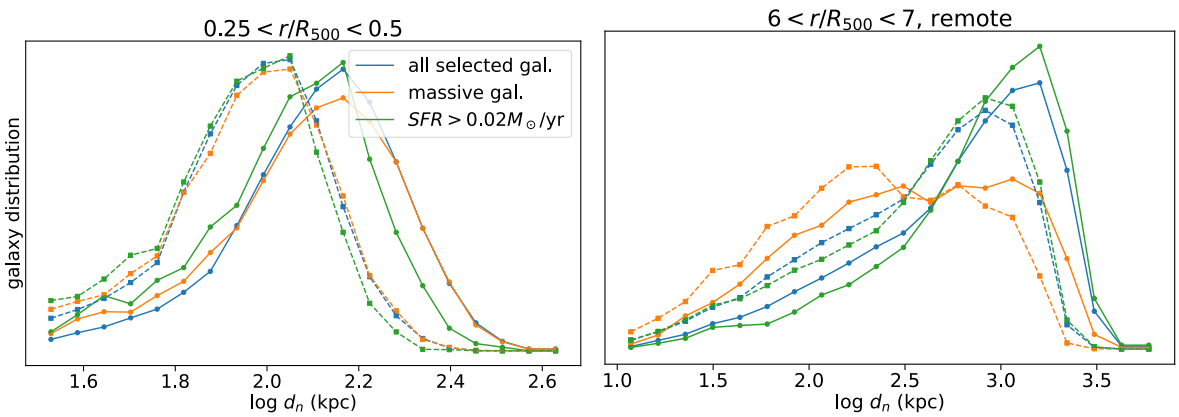

Figure 4.3: Distribution of distances to the nearest neighbour d_n of galaxies between $r = 0.25$ and 0.5 R_{500} on the left panel, and in the remote regions far away from the main cluster (in the field) on the right panel. Solid lines represent the distribution at $z = 0.25$ and dashed lines at $z = 0.90$. Colors represent 3 different populations of galaxies; all galaxies (mostly low-mass quiescent galaxies), star-forming and massive galaxies. Data points represent the centres of the histogram bins and are normalized to have the same surface area.

NFW profile due to this relative overdensity. This difference in the distribution of galaxies with different masses is often referred to as the *mass segregation*. The effect is thought not to be important for low-mass galaxies (e.g., see von der Linden et al. 2010), which is not surprising since the galaxy needs to be massive enough compared to the host cluster in order to be able to sink into the potential well to lower orbits via dynamical friction in a reasonable amount of time (a few Gyr) (e.g., see Boylan-Kolchin et al. 2008). Note that massive galaxies used in this work ($\log M_*(M_\odot) > 11$) may already account for a noticeable portion of the parent halo mass - most of the considered groups have M_{500} just above $10^{13} M_\odot$.

In figure 4.4, we can also see that galaxies at high redshift prefer lower relative radii r; a larger fraction of them is located below R_{500} than at low redshift. This indicates that the galaxies are more concentrated at high redshift, which is formally shown in Appendix B and may explain why some radial features, shown throughout this chapter and chapter 5, appear at lower r at high redshift.

4.4 Stellar Mass

Stellar mass M_* of galaxies should be considered in more detail since it is tightly correlated with AGN activity, as we will see in chapter 5. On the other hand, AGN feedback can quench the star formation rate and thus "freeze" the stellar mass of galaxies. In Magneticum simulations, we can see a clear example of this. Black holes in the simulation are seeded well below the $M_\bullet - M_*$ relation (Steinborn et al. 2015, Magorrian et al. 1998) and thus undergo a phase of very efficient AGN feedback. They accrete below the Eddington limit and are unable to suppress the gas cooling. Thus the black holes grow rapidly until they reach the $M_\bullet - M_*$ relation, where the star formation rate is abruptly quenched. This causes a peak in the stellar mass function, which is not observed in nature and is purely a consequence of the subgrid

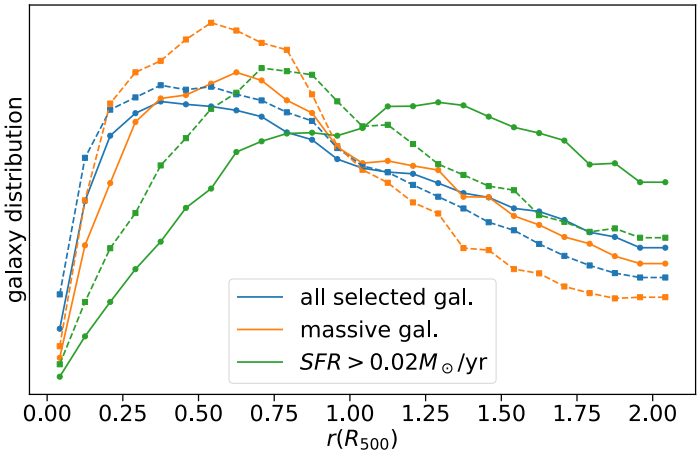

Figure 4.4: Distribution of clustercentric distances r of the galaxies in the inner cluster regions. Results are plotted for two different redshifts; the solid line is used for $z = 0.25$ and the dashed line for $z = 0.90$. Data points represent the centres of the bins of the normalized histograms. Distribution is plotted for star-forming, massive and all galaxies (mostly low-mass quiescent galaxies).

model; the location of the peak depends on the black hole seeding mass (for more details, see Steinborn et al. 2015). In figure 4.5 the distributions of stellar masses M_* and clustercentric distances r are plotted, and we can quickly identify an excess of galaxies above the black hole seeding limit, $\log M_*(M_\odot) \approx 10.15$ (left panels). We can also see that the excess corresponds to the rapid decline in the number of star-forming galaxies caused by the black hole feedback (right panels). This happens at slightly higher masses ($\log M_*(M_\odot) \sim 10.4$) than the black hole seeding M_* due to the time the black hole needs to reach the $M_\bullet - M_*$ relation and quench the galaxy. In figure 4.5 we also notice a significant difference between low and high redshift. The galaxies at higher redshift (lower panels) seem to reach higher stellar masses before being quenched (i.e., frozen on the M_* axis), causing the M_* excess to be more extended. In Steinborn et al. (2015), this is found to be a consequence of slower black hole growth right after the seeding at higher redshift.

Although the excess of galaxies above the seeding M_* implies that the behaviour in that M_* range may not be described realistically, we can use it to cast light onto processes in the cluster environment. Stellar mass of galaxies gets frozen for a while after the newly seeded black hole quenches the galaxy - even more so if the galaxy is in the cluster environment, which is on its own unsuitable for star formation. Any change in stellar mass that happens while the galaxy is quenched is a consequence of other processes, not star formation. We can get some insight into those processes by tracing the M_* of the overdensity of galaxies, as a function of r. In figure 4.5, we can see that the mass of the overdensity is reduced near the centre of the cluster (below $0.5\ R_{500}$), indicating the stellar mass stripping in the cluster centre due to tidal interactions between galaxies. In chapter 5 we will see how this affects the radial AGN activity profiles. I further verified (not shown explicitly) that the M_* of this overdensity decreased even in locally denser environment at constant r ($0.2R_{500}$). It is also possible that this decrease of stellar mass is caused by the Subfind algorithm wrongly assigning some of

the stars to other halos, however I mostly rule out this possibility by using the maximum circular velocity as a proxy for the mass of the galaxy (also discussed later in section 5.4).

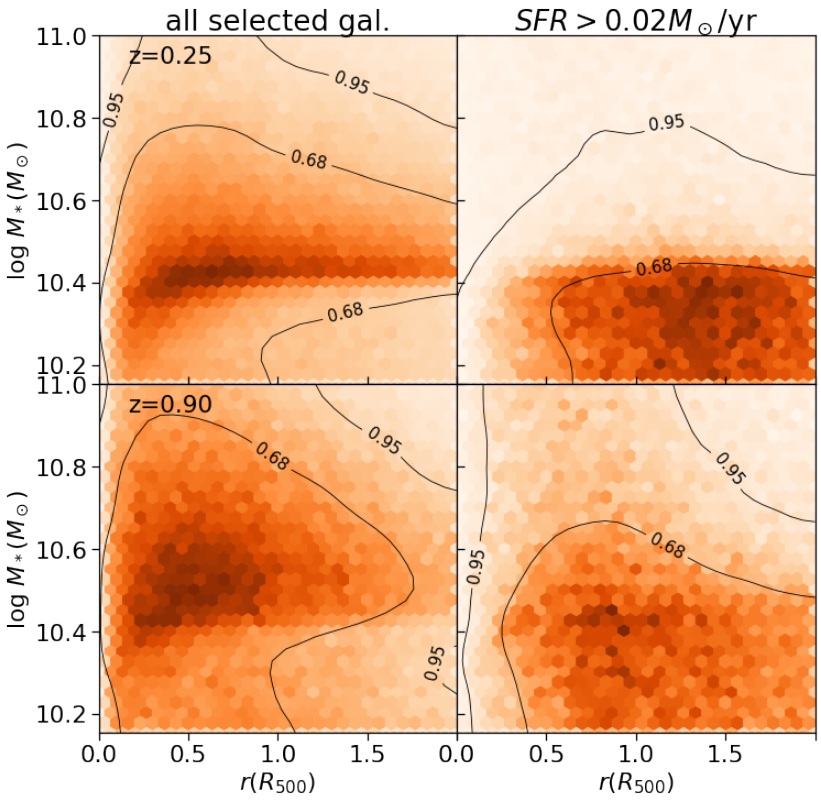

Figure 4.5: Distribution of clustercentric distances r and stellar masses M_* of galaxies in the inner cluster and group regions. Results are plotted at low redshift (upper panels) and high redshift (lower panels) and for star-forming galaxies (right panels) and all (mostly quiescent) galaxies (left panels). Contours show the positions of 68% and 95% of galaxies for clarity.

4.5 Star Formation Rate

The star formation rate of galaxies is tightly correlated with their stellar mass. Star-forming galaxies lie on a power law relation between stellar mass and the star formation rate, also known as the star-forming *main sequence*. The relation is believed to hold for many orders of magnitude in stellar mass and a wide range of redshifts (e.g., see Pearson et al. 2018, Speagle et al. 2014). Star-forming galaxies tend to oscillate around the main sequence on timescales $\sim 0.4 t_h$ due to gas compaction and central gas depletion (see Tacchella et al. 2016), which results in a scatter of galaxies around the main sequence. Nonetheless, star-forming galaxies on the main sequence and the bulk of quiescent galaxies are well separated with a region of SFR values, containing very few galaxies, also called the green valley (e.g., Wyder et al. 2007). The main sequence model can be described with the slope α and the normalization β, which can be rewritten in terms of sSFR:

$$\log\left(\mathrm{sSFR}/\mathrm{yr}^{-1}\right) = (\alpha - 1)\,(\log M_*/M_\odot - 10.5) + \beta - 10.5, \tag{4.1}$$

where slope α is usually between 0 and 1, and parameters α and β are redshift dependent. Note that $\alpha = 1$ means that the SFR is proportional to stellar mass. In figure 4.6 the distribution of M_* and sSFR of galaxies in extended cluster regions in box2b is plotted. For comparison, the fit of equation (4.1) from Pearson et al. (2018) is added, with $\alpha = 0.43$ and $\beta = 0.58$ at low redshifts and $\alpha = 0.46$ and $\beta = 1.10$ at high redshifts. The distribution of the star formation rates in Magneticum was already discussed in Lotz et al. (2021) and in figure 4.6 I successfully reproduce some of their findings.

In the leftmost panels of figure 4.6 we can see that most low-mass galaxies indeed follow a close relation. This relation seems to locally have a different slope ($SSFR \approx const, \alpha \approx 1$) than shown in Pearson et al. (2018); however, the general trend with decreasing sSFR in massive galaxies is in line with observations (although the agreement seems to be slightly better at lower redshift). Some observations also report the bending of the main sequence at high stellar mass, where the galaxies at around $\log M_* \approx 11 M_\odot$ do not follow the same relation as low-mass galaxies but fall below it (e.g., Whitaker et al. 2015, Schreiber et al. 2015), especially at lower redshifts. The relative reduction in SFR with stellar mass may be a result of the larger bulge components relative to the disc components (Abramson et al. 2014), but also other mechanisms, suppressing the star formation (Whitaker et al. 2015). Together with the slope of the main sequence, this causes the bulk of massive galaxies to fall below the common limit for star-forming classification (equation (2.9)) - we have only a handful of massive star-forming galaxies (see section 2.6)[1]. In figure 4.6 we can again see how AGN feedback rapidly quenches galaxies at the black hole seeding stellar mass (leftmost panels). In terms of redshift evolution, we can see that aside from the more gradual quenching at high redshift, there are no major qualitative differences between $z = 0.25$ and $z = 0.90$. It is also worth pointing out the narrow excess of massive galaxies (right panels of the left figure) at a low star formation rate. The excess is found at constant SFR $\approx 0.1 M_\odot/\mathrm{yr}$ and is thus well above the resolution of subfind ($0.02 M_\odot/\mathrm{yr}$). The overdensity is likely caused by some numerical effect, but the exact cause has to my knowledge not yet been identified.

To get some insight into processes governing the star formation rate, I plot the ratio between the number of star-forming and quiescent galaxies (henceforth *star-forming ratio*) as a function of r. In figure 4.7, the star-forming ratio profile is shown for extended cluster regions up to $8R_{500}$. Since at those distances, the large-scale structure surroundings and neighbouring clusters play a significant role, I split all galaxies into overlapping and remote populations according to their distance from the neighbouring clusters (see chapter 3). In *low-mass* galaxies (left panels), we can notice a strong decline in the star formation rate towards the cluster centre at low and high redshift. This is in agreement with observations (e.g., Cohen et al. 2014, von der Linden et al. 2010, Boselli & Gavazzi 2006, Balogh et al. 1998). In the latter, a strong decrease in the star formation rate is reported, with a fraction of

[1]We should always keep in mind that in this work, different classification is used. Star-forming galaxies in this work may be considered quiescent in the literature.

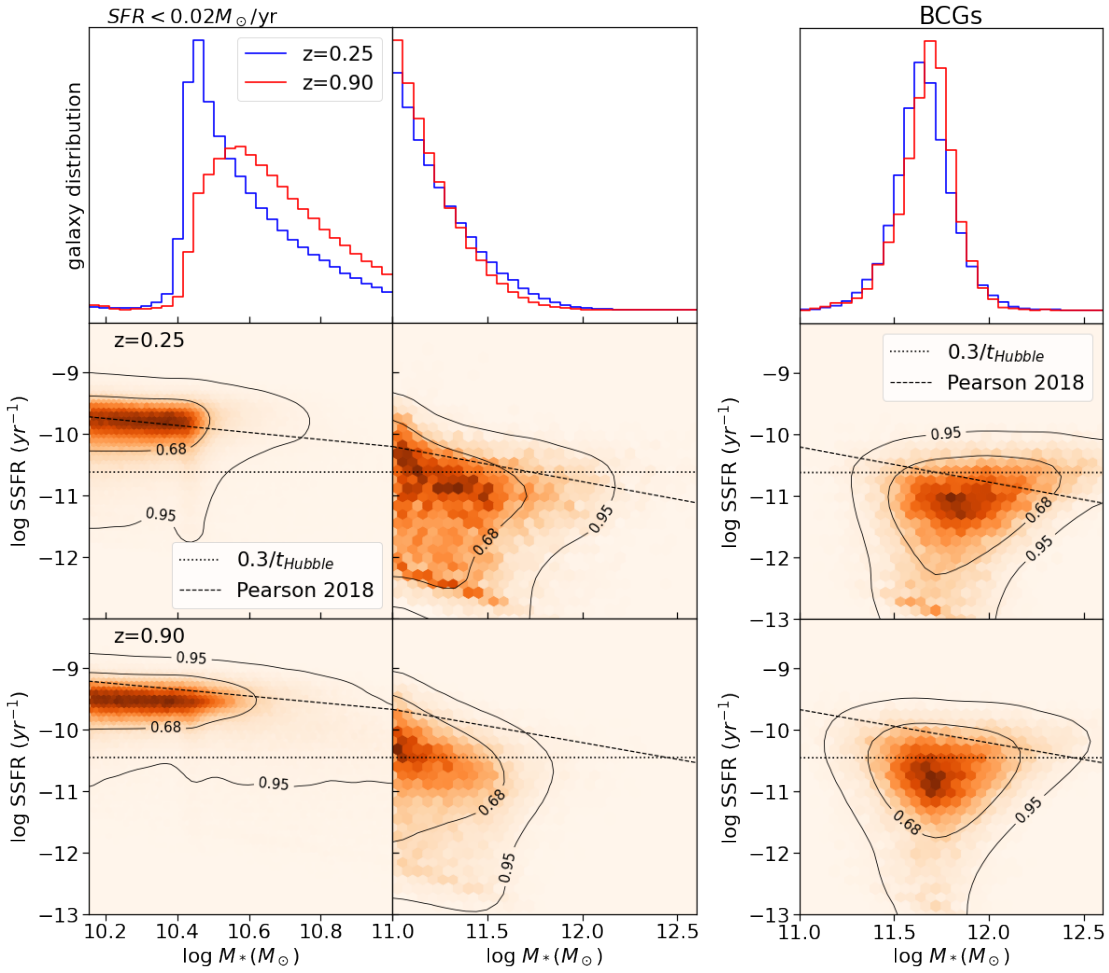

Figure 4.6: The figure contains three columns, the left column with low-mass galaxies, the middle column with massive galaxies without the BCGs and the right column only with the BCGs. Each column has three panels. The uppermost panel shows the normalized distributions of M_* of quiescent galaxies at low and high redshifts. On the middle panel, the distribution of M_* and sSFR of galaxies in extended cluster regions is shown at low redshift and on the bottom panel at high redshift. The dotted line represents the limit between the star-forming and quiescent galaxies according to the blueness criterion (equation (2.9)). The dashed line is the observational fit from Pearson et al. (2018) (the seeming slope change between the left and the middle column is a consequence of a different M_* range).

star-forming galaxies[2] close to 0 in the centre, and the decline starting far beyond the virial radius. The decline is not attributed only to different morphology of galaxies but is also found in galaxies with similar morphology (see Christlein & Zabludoff 2005, Balogh et al. 1998). This strong global environmental dependency may be a consequence of the *environmental quenching*, which is expected to dominate in low-mass galaxies (i.e., $\log M_*(M_\odot) < 10.6$, see Peng et al. 2010 and references therein, also Lotz et al. 2019 and Teklu et al. 2017), and should be largely independent of redshift and stellar mass. The possible physical mechanisms for environmental quenching and central suppression of star formation are ram pressure stripping and strangulation (section 1.7).

[2]For low values, the ratio between the number of star-forming and quiescent galaxies is approximately equal to the fraction of star-forming galaxies.

If we select only *massive* galaxies ($M_* > 10^{11} M_\odot$, right panels of figure 4.7), we find a considerably different behaviour. The number of star-forming galaxies generally *increases* towards the centre of the cluster if we consider remote galaxies not influenced by the neighbouring clusters. If we go into details, we can see that the profile consists of two local maxima, where the probability for star formation peaks. One is located in the inner cluster regions and will be examined more thoroughly later in this section. The second peak is located on the outskirts and may be connected to the increase of AGN activity at the same r, discussed in section 5.5.

In figure 4.7 we can also see how the behaviour in the inner cluster regions is reflected in the profile of the overlapping population and consequently in the combined profile. The central decline in star formation found in *low-mass* galaxies (left panels) is reflected in the decrease at very large r, where inner regions of neighbouring clusters are considered. Analogously, an excess of the star-forming ratio in *massive* overlapping galaxy population (right panels) at large r is a result of the central increase. The peak of the low-mass overlapping profile is predicted in chapter 3, and is probably a consequence of geometric overlaps of clusters and not physical effects. The same can be claimed for the maximum in the profile of massive galaxies on the right panels, although the direct comparison with chapter 3 is not straightforward since the profile is drastically affected by the neighbouring BCGs that were not considered explicitly there.

In some simulations (e.g., Hwang et al. 2019) and observations (e.g., Tran et al. 2010, Santos et al. 2015), the radial dependence of the star formation rate changes dramatically with redshift - at higher redshifts, the star formation level increases towards the centre of the cluster, whereas at low redshift, it decreases (this trend is also known as the *reversal of the SFR-density relation*). By observing the star-forming ratio in our simulations (figure 4.7) we do not notice any signs of such reversal. The profiles look qualitatively similar at redshifts 0.25 (upper panels) and 0.90 (lower panels), regardless of the stellar mass. However, the difference in redshift might not be significant enough to show any differences.

Different overall star-forming ratio of massive galaxies compared to low-mass galaxies may be a consequence of the so-called *mass quenching* (see Peng et al. 2010), which is only weakly dependent on the environment but depends strongly on the total star formation rate of the galaxy. This implies more efficient quenching in more massive galaxies if they lie along the main sequence branch. In figure 4.7 we can see that the star-forming ratio in the field (remote galaxies at large r) is around 4 times larger in low-mass galaxies (on the left) than it is in massive ones (on the right). Several reasons for this behaviour have been proposed; it may be related to the feedback processes from supernovae or to the local ionisation (Cantalupo 2010). The quenching may also be a consequence of more intense AGN activity in massive galaxies (see chapter 5 and Steinborn et al. 2015). For further discussion about environmental

and mass quenching in Magneticum simulations, see also Teklu et al. (2017) and Lotz et al. (2019).

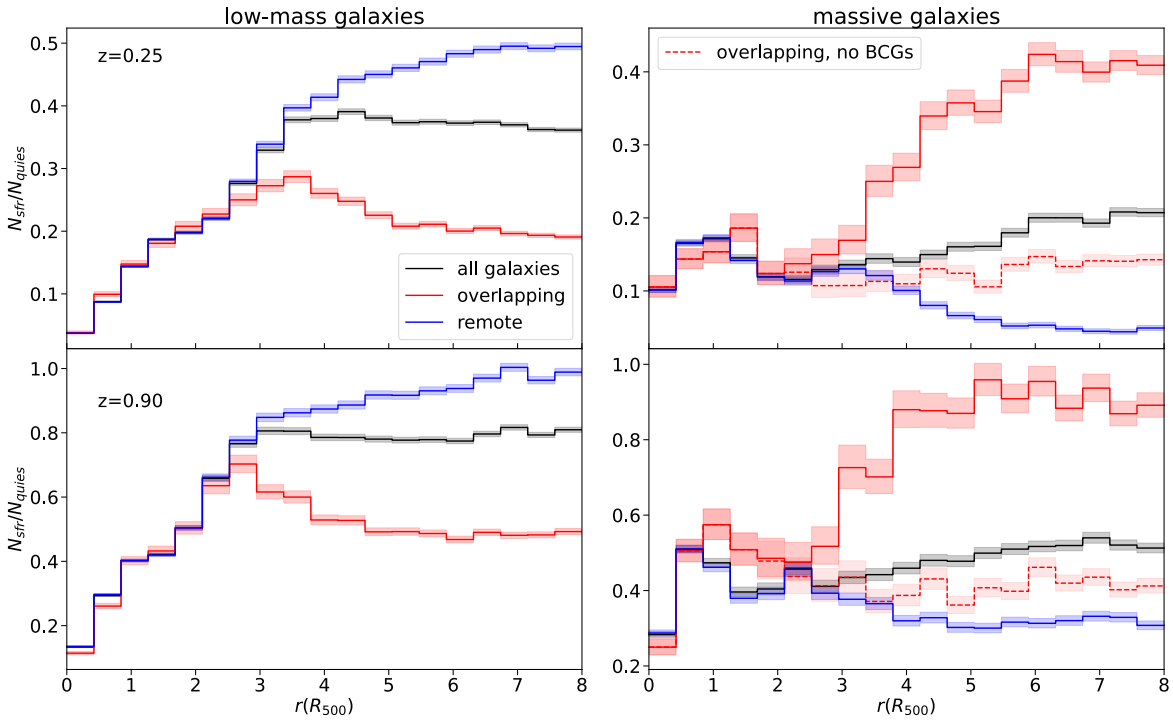

Figure 4.7: The ratio between the number of star-forming (SFR $> 0.02 M_\odot$/yr) and quiescent galaxies as a function of clustercentric distance r On the left, I show low-mass galaxies with $10.15 < \log M_*(M_\odot) < 11$, and on the right only massive galaxies with $\log M_*(M_\odot) > 11$. Results are shown at low redshift (upper panels) and high redshift (bottom panels) and for the overlapping and remote regions (with overlapping distance $6R_{500}$, refer to chapter 3). On the right panels, the dashed line represents the massive overlapping populations without the BCGs of the neighbouring groups with $M_{500} > 10^{13} M_\odot$. Errors are derived from Poisson statistics (see appendix A.1).

The star-forming ratio as a function of r in the *inner* cluster regions, shown in figure 4.8, further casts light on the behaviour inside the clusters. We can clearly see the inner peak of the star-forming ratio in massive galaxies between 0.5 and $1R_{500}$, followed by a rapid decline towards the centre. A similar tendency can be noticed in low-mass galaxies - at a distance $r \sim 1.5R_{500}$ where the star-forming ratio of massive galaxies rises with decreasing r, the ratio in low-mass galaxies levels out - the decline of the star-forming ratio towards the cluster centre is delayed for a while and only continues to drop in the inner regions (below $\sim R_{500}$). All of this is in line with what was mentioned in the previous paragraph - infalling galaxies may have star formation triggered by the pressure inside the ICM. This starburst only lasts a short amount of time, which might be why the excess of star formation is followed by a rapid decline in the centre (aside from the AGN feedback, discussed in chapter 5 and other environmental effects). This behaviour is less prominent in low-mass galaxies, which may be because low-mass galaxies are generally more susceptible to SFR suppression (they would still be star-forming in isolation), as discussed above and later in this section. Moreover, massive galaxies are more likely contained within other groups (see section 4.1) and are thus more likely to be infalling, whereas low-mass galaxies can also

orbit inside the cluster potential and might have already gone through the starburst phase. It should also be stressed that massive galaxies are much better resolved in our simulation than low-mass galaxies; it may be the case that in low-mass galaxies, we do not have large enough resolution to simulate the compression of gas clouds and produce similar starbursts. The infall of individual galaxies in our simulations was also studied in Lotz et al. (2019). They notice a distinction between rapid environmental quenching in low-mass galaxies and the gradual effects of mass quenching. No increase in the star formation rate of massive galaxies is reported during the infall (although the quantities and samples studied there are not directly comparable, as shall be discussed in the next paragraph). However, they report the delayed quenching of (probably more massive) central group satellites.

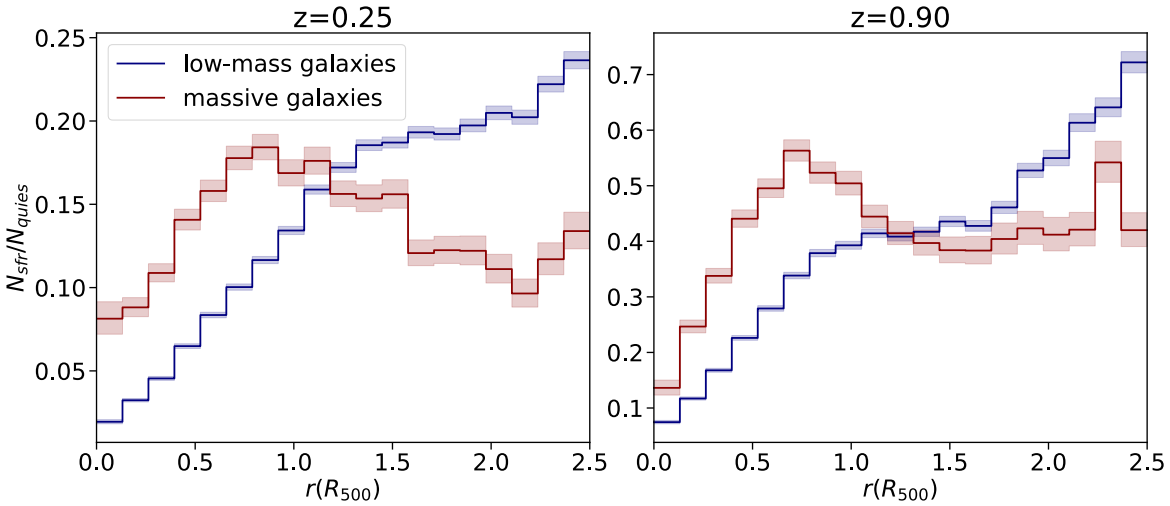

Figure 4.8: The ratio between the number of star-forming (SFR $> 0.02 M_{\odot}/\mathrm{yr}$) and quiescent galaxies as a function of clustercentric distance r shown for low-mass and massive galaxies at high redshift (right panel) and low redshift (left panel) in the *inner cluster regions*. Plots represent the zoomed-in versions of the combined plots in figure 4.7.

It is also essential to consider the possibility that the sSFR variations with r are a mere consequence of *mass segregation*. Since the expected mass of the galaxy varies with clustercentric distance r, and since the star formation rate is correlated with stellar mass, the differences in the star formation rate may be a mere reflection of different stellar masses and not attributed to environmental processes directly. This hypothesis is supported by van den Bosch et al. (2008) and argues against the significance of the environmental effects in massive halos. The evidence for mass segregation in our simulations has been shown in section 4.3. In order to determine whether the profiles in figure 4.8 are a consequence of mass segregation, I show the radial star-forming ratio profiles only for galaxies in a *narrow* M_* *range* (figure 4.9). Although the exact values of the star-forming ratio depend on the selected mass range, there are no major qualitative differences in behaviour to figure 4.8. I thus argue against the role of mass segregation, in favour of environmental effects in the profile of both low-mass and massive galaxies.

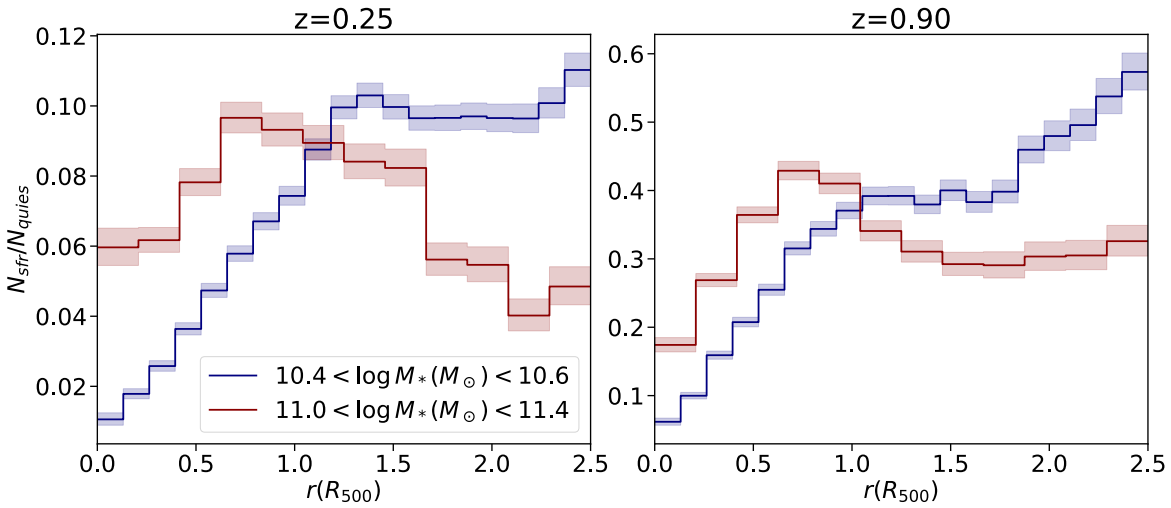

Figure 4.9: The ratio between the number of star-forming (SFR $> 0.02 M_\odot$/yr) and quiescent galaxies as a function of clustercentric distance r, shown for two *narrow* M_* *ranges* (one in the massive and one in the low-mass range). Profiles are shown at low redshift (left panel) and high redshift (right panel). The profiles are qualitatively similar to those in figure 4.8, where a wider M_* range was used.

I also investigated the effects of the *substructure* in the inner cluster regions in figure 4.10. On the left panel, it is clearly shown how the quenching in low-mass galaxies is delayed more strongly (the profile falls off at smaller r) if a galaxy is a group satellite. The overall increase of the star-forming ratio in clusters with rich substructure is also found in observations (e.g., Cohen et al. 2014). This may indicate that low-mass galaxies are shielded from the cluster environment for longer after the infall. However, it is also possible that this is a mere consequence of different kinematics - we expect most of the group satellites to be falling towards the cluster centre for the first time (see section 1.5), which is not necessarily true for the isolated satellites. The infall of isolated and group galaxies has more thoroughly been studied in Lotz et al. (2019). On the right panel of figure 4.10 the radial profiles of massive galaxies are shown. It appears that the peak of the star-forming ratio found in figure 4.8 only appears in the central galaxies of the infalling groups (and not in isolated satellites). This generally agrees with the hypothesis that the peak is produced by the gas compression while the galaxies are falling into the cluster (groups tend to be infalling). I also verified (not shown explicitly) that the difference is not a consequence of different stellar masses - it remains even if galaxies in a narrow M_* range are selected.

So far, we have only looked into how the star-forming ratio depends on the distance r. However, it is also instructive to see how the sSFR value of star-forming galaxies changes with r. If low-mass galaxies are selected, M_*-sSFR distribution remains virtually unchanged; galaxies are scattered around the main sequence, as can be seen in the left panel of figure 4.6, regardless of the global environment (I do not show the low-mass M_* – sSFR relation explicitly for different radii since it is not very informative). In other words, low-mass galaxies in the cluster environment are most likely to be quiescent, but if they manage to retain conditions for star formation, the star formation rate tends to be on the same (main sequence) level, regardless of the position r. The lack of environmental dependence of the

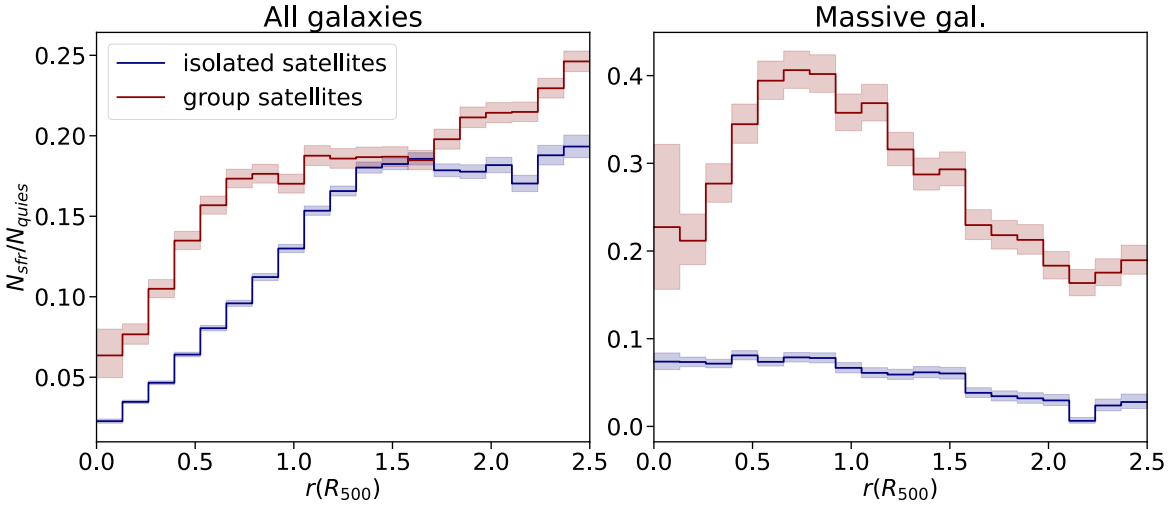

Figure 4.10: The ratio between the number of star-forming (SFR $> 0.02 M_{\odot}$/yr) and quiescent galaxies as a function of clustercentric distance r, for galaxies that belong to *groups* with multiple galaxies embedded into the central cluster halo (i.e., group satellites), and for galaxies which belong to directly to the central cluster halo (i.e., isolated satellites, see section 4). The ratio for all galaxies (mostly low-mass galaxies) is plotted on the left panel, and the ratio for massive galaxies is plotted on the right panel. The profiles are shown at low redshift ($z = 0.25$).

star formation rate of star-forming galaxies, despite the strong environmental dependence of the *star-forming ratio*, is also reported in Peng et al. (2010) and Muzzin et al. (2012). We are unlikely to observe galaxies in the transition phase over the green valley, which points to the rapid quenching of SFR after the infall, or to the so-called *delayed-then-rapid* quenching scenario, in which the effects of quenching in a galaxy become apparent only a while after the external gas supply is cut off (Wetzel et al. 2013). Here we should note that in simulation, we directly observe the star formation rate (and not colour), thus we have real-time information about the star formation properties of galaxies (further discussed in Lotz et al. 2019).

Results are, however, different for massive galaxies. The sSFR value of a galaxy with a certain M_* is environment-dependent. M_*-sSFR distributions of massive galaxies at different radii r are shown in figure 4.11. It can be seen that the expected star formation rate in the inner cluster regions (below R_{500}, leftmost panel) is slightly higher than on the outskirts (above $2R_{500}$, other panels), which is in agreement with what is found in IllustrisTNG simulations (Hwang et al. 2019). This also means that the expected star formation rate of massive galaxies seems to roughly trace the star-forming ratio, something not observed in low-mass galaxies. Since this shift happens at constant M_*, this can be seen as another argument against mass segregation having a decisive role in the radial profiles in figure 4.7. Mass segregation, however, still exists, as already shown before in figure 4.4. Remote massive galaxies (rightmost panel) are more likely to have lower M_* than cluster galaxies.

It is also intriguing to see how the star-forming ratio depends on the local density (distance to the nearest neighbour d_n). The ratio is plotted in figure 4.12 for the inner cluster regions (right panel) and for the field galaxies (left panel). A narrow radial shell was chosen to

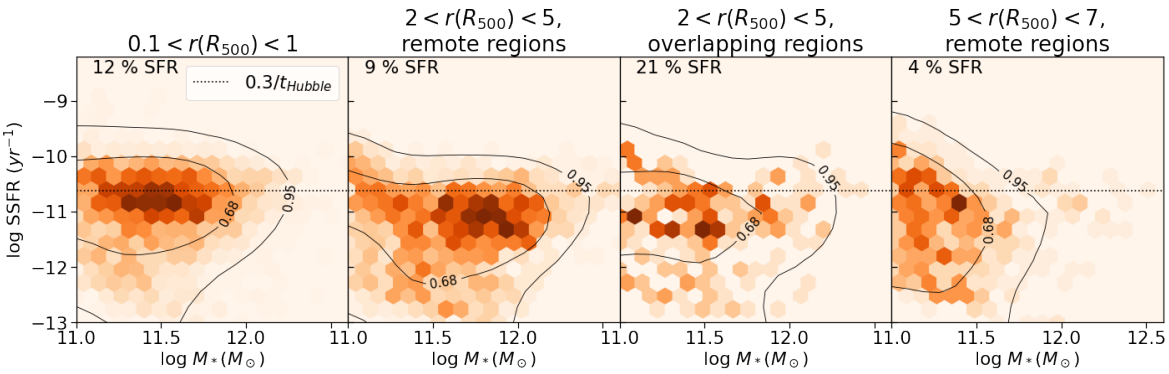

Figure 4.11: Distribution of M_* and sSFR for massive galaxies in different cluster (and field) regions. the dashed line indicates the blueness criterion (equation (2.9)). In the top left corner of each panel, I print out the fraction of star-forming galaxies (SFR > 0.02) in that cluster region. I separately show the remote and overlapping regions.

disentangle the local density effects from the global cluster environment (r). Some of the trends have already been pointed out in figures 4.2 and 4.3. The correlation between the local density and the star formation rate depends on the large-scale environment. Inside the cluster environment, *low-mass galaxies* are much more likely to form star if d_n is small (right panel of figure 4.12). This trend (in the same d_n range) is less pronounced in the field galaxies (left panel). This may be due to smaller groups and substructures having their own atmosphere, shielding the galaxies from the effects of the ICM in the cluster environment. Field galaxies (left panel), show the opposite trend; they are more likely to form stars if they are very far from their neighbours. In other words: a galaxy is more likely to form stars if it is in the field, far away from any aggregations of galaxies that generally suppress star formation (as discussed above). But if it does find itself inside a galaxy cluster, it is more protected from the environmental quenching if it is in a locally very dense environment, possibly within a smaller group. Those findings partially agree with Hashimoto et al. (1998), where they report the suppression of SFR in a denser local environment in the field. They observed a similar decrease in cluster regions; however, no comparison was made at constant distance r. Suppression of SFR in locally denser cluster regions may thus reflect high number density in the cluster centre, where SFR is very low (as seen in figure 4.7)[3].

Massive galaxies in figure 4.12 again show a different behaviour. In the cluster environment (right panel), massive galaxies are less susceptible to the environmental quenching processes than low-mass galaxies since their star-forming ratio is systematically higher. Interestingly, I find that massive galaxies show a relatively consistent behaviour in both panels - the star-forming ratio of galaxies increases with the local density, regardless of the global environment. The lowest star-forming ratio is found in very secluded galaxies around 1 Mpc away from the nearest neighbouring galaxy; the ratio there is as low as 0.01 at low redshift. This may again indicate the importance of mass quenching. In the hierarchical structure formation framework, galaxies tend to migrate from the less dense environment to denser clusters

[3]Observing local density at different r also prevents direct comparison with some other works (e.g., Cohen et al. 2014).

and groups and unlikely vice versa. That means that a galaxy in isolation has probably formed and evolved there, without being subjected to environmental quenching in the cluster environment. On the contrary, a denser environment seems to either trigger star formation in quenched massive galaxies or prevent the cessation of star formation - not just in the dense cluster environment, but wherever the local density is elevated (apart from the densest regions, where lower ratio may reflect the influence of cluster cores, as has been shown in previous paragraphs).

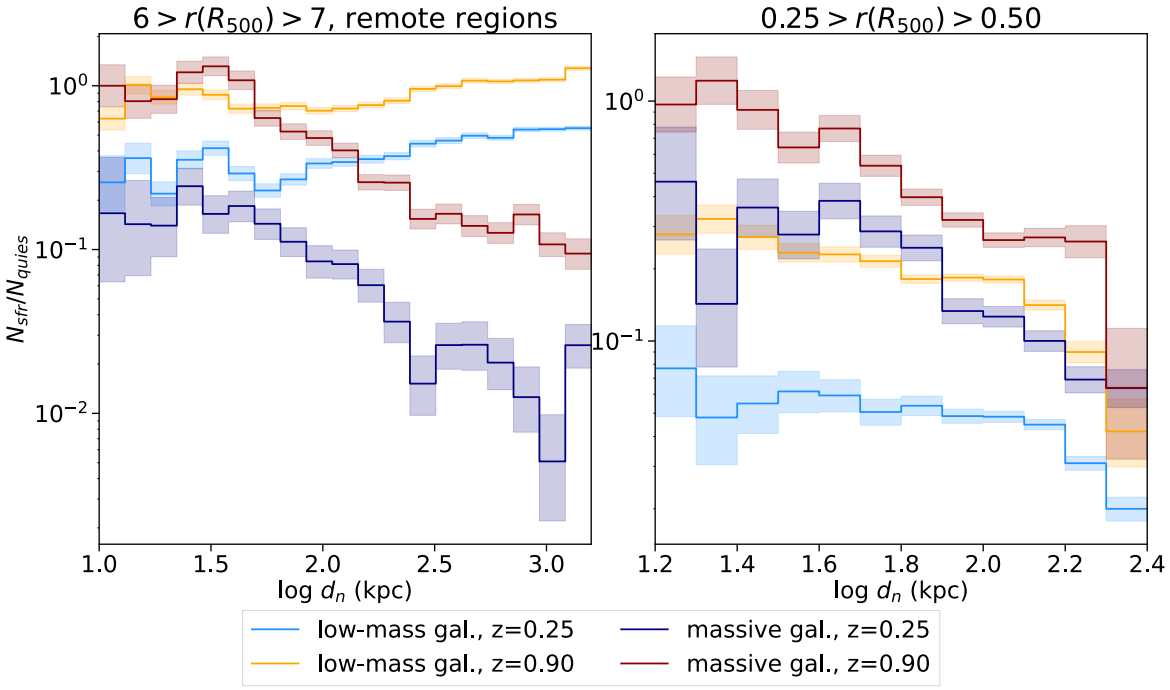

Figure 4.12: The ratio between the number of star-forming (SFR $> 0.02 M_{\odot}$/yr) and quiescent galaxies as a function of the distance to the nearest neighbour d_n. Results are shown for low and high redshift and for low-mass and massive galaxies. On the left panels, isolated regions between $6R_{500}$ and $7R_{500}$ are selected, and on the right panel, I choose the cluster regions between 0.25 and $0.5R_{500}$; narrow radial bins are chosen to distinguish the effects of the local density from the effects of the global cluster environment. Errors are derived in A.1.

4.6 Cluster Mass

In the previous sections, both low-mass clusters (above $10^{13} M_{\odot}$) and massive clusters (above $10^{14} M_{\odot}$) were considered together. In this section, I will demonstrate how the impact of the cluster environment varies with cluster mass. In figure 4.13 I show the distribution of stellar masses M_* of galaxies and masses M_{500} of their parent clusters. Stellar mass of massive galaxies appears to be correlated with M_{500}; if a galaxy is very massive, it likely resides in a cluster with higher mass. This holds for quiescent as well as star-forming galaxies. In quiescent galaxies (third panel), this correlation is less evident (and had to be verified separately) due to the low number of very massive clusters. M_{500} of star-forming galaxies is distributed somewhat more uniformly since the star-forming ratio also increases with cluster

mass (up to some M_{500}, discussed later in this section). It also seems that the correlation between M_* and M_{500} is tighter in star-forming galaxies (second panel).

The correlation itself is not that surprising. Note that the dark matter halo mass of massive galaxies ($\log M_* \approx 11.5$) is of the order of magnitude of the low-mass groups that we still consider ($\log M_{500}(M_\odot) \approx 13$). Hence it is unlikely that many massive galaxies are found in low-mass groups. For one, such an association of galaxies would probably need to form via mergers of similar-size halos, which happen much less frequently than the accretion of low-mass halos (section 1.5). Moreover, such mergers would increase the mass of the progenitor halo, bringing it out of the low-mass range. On the contrary, massive clusters are known to accrete groups containing massive galaxies. Additionally, a dense environment is expected to accelerate the evolution of very massive galaxies (e.g., see Yoon et al. 2017). In galaxy clusters, galaxy mergers and the consequential growth of very massive galaxies most likely occur in the in-falling groups where velocity dispersion of galaxies is low enough (Benavides et al. 2020). I also compared the stellar mass functions of galaxies in clusters of different mass ranges (not shown explicitly) and indeed found, that the massive tail of the M_* distribution is truncated in low-mass clusters. This, however, only explains one side of the correlation - why the *maximal* stellar mass of galaxies increases with M_{500}. However, we can also see in figure 4.13, that clusters also have some *minimal* stellar mass of *massive star-forming* galaxies, which also increases with M_{500}. This may be due to environmental effects in massive clusters, preventing star formation in galaxies that are not massive enough (discussed further in the following paragraphs).

Let me also point out the strong correlation between the M_* of the BCGs and the mass of the surrounding clusters (right-most panel in figure 4.13). I fitted the power law model $M_{500} \propto M_*^n$ to the data[4] and obtained $n \approx 1.2$ at low redshift and 1.3 at high redshift. This means that the BCGs accrete mass and grow with time almost proportionally to the cluster where they reside. The value of n is in agreement with $n = 1.3 \pm 0.1$ that is found in Stott et al. (2012), but is lower than $n = 1.6 \pm 0.2$ in Lidman et al. (2012) and most other studies (see references in Lidman et al. 2012), which is somewhat surprising considering that the stellar masses of very massive galaxies in our simulations are overestimated (Steinborn et al. 2015).

In figure 4.14 the ratio between the number of star-forming and quiescent galaxies in the inner cluster regions is plotted as a function of M_{500} of the parent cluster at low and high redshift (left and right panel respectively). We can see that *low-mass*-galaxies are less likely

[4] I used the *orthogonal distance regression* (ODR) package (Boggs & Donaldson 1989) of the *scipy* library. I accounted for the truncated M_{500} range by iteratively excluding the data points to the left of the model M_* value at the minimal M_{500}. Note that choosing such data selection may lead to a biased power-law index estimate, but this way, we do not need to discard information about low-mass clusters. By using different methods of data selection, the slope n varied by approximately 0.05, which is a more reliable estimate of error than returned by the fitting routine and shown in figure 4.13.

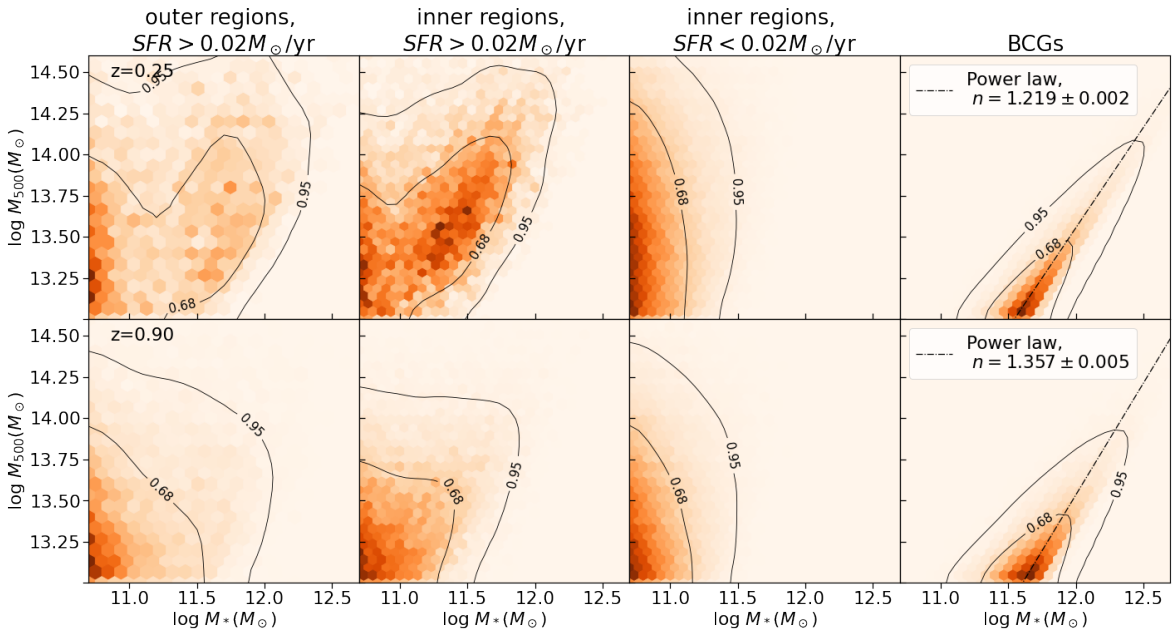

Figure 4.13: Distributions of M_{500} of the parent cluster and M_* of galaxies. Results are plotted for the outer regions (from 2 to 4 R_{500}), inner regions (below 2 R_{500}) without the BCGs, and only for the BCGs. Galaxies are divided into quiescent and star-forming populations. The first row shows the distributions at low redshift and the second row at high redshift. The power law model $M_{500} \propto M_*^n$ is plotted in the last panel with the BCGs, and the power-law index is shown in the legend.

to be star-forming if they are in more massive clusters, which reflects the effects of the ICM that are stronger in the dense atmosphere of very massive clusters. *Massive* galaxies show an even more intriguing behaviour. A massive galaxy (above $10^{11} M_\odot$) is most likely to be star-forming if it is located in the inner regions of intermediate-mass clusters (around $\log M_{500}(M_\odot) \approx 13.7$). In low-mass or very massive clusters, the star-forming ratio drops significantly. This non-monotonic behaviour may reflect an increase of stellar mass with cluster mass, shown in the previous paragraphs. In the previous section, I showed that the effects of the cluster environment are strikingly different for low-mass and massive galaxies (4.7); low-mass galaxies have their star formation quelled, whereas massive galaxies display a general increase of the star-forming ratio in the cluster environment. An increase of the ratio between $\log M_{500}(M_\odot) \approx 13$ and 13.5 in figure 4.14 might reflect the transition between the two regimes. Groups below $\log M_{500}(M_\odot) \approx 13.5$ on average host less massive galaxies (see figure 4.12) which may still be subjected to environmental quenching mechanisms. On the other hand, a decrease in the star-forming ratio in very massive clusters may again reflect what is also observed in figure 4.12 - galaxies in massive clusters need to be very massive in order to have their star formation triggered and there are not many galaxies above this mass threshold. Those two effects may then combine into the "peak" of the star-forming ratio observed in figure 4.14.

In figure 4.15 I plot the ratio between the number of star-forming and quiescent galaxies as a function of M_{500} for galaxies that belong to smaller groups within the cluster (group satellites) and for galaxies belonging directly to the main cluster halo (isolated satellites). On

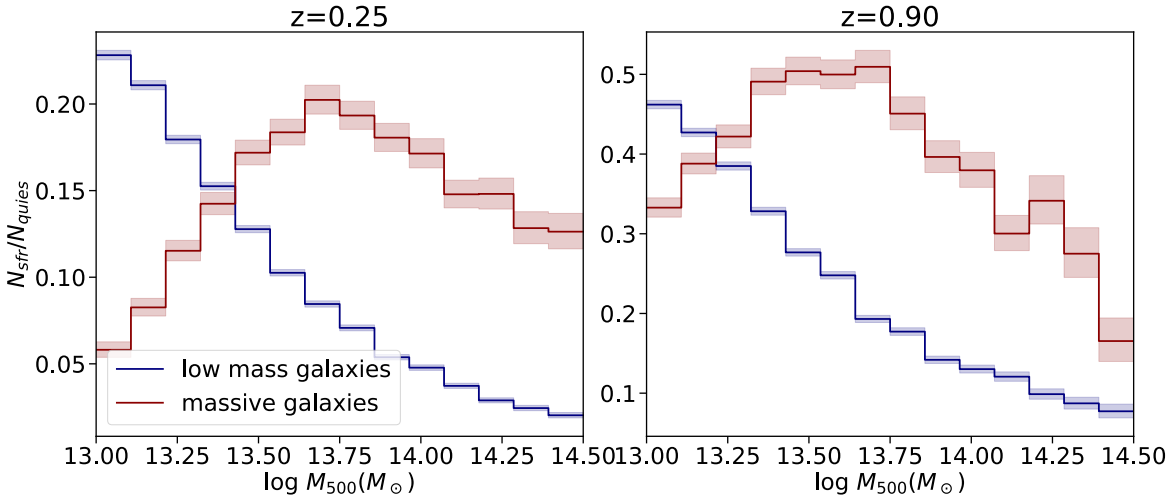

Figure 4.14: The ratio between the number of star-forming (SFR $> 0.02 M_\odot$/yr) and quiescent galaxies as a function of the cluster mass M_{500} for low-mass and massive galaxies at high redshift (right panel) and low redshift (left panel). Regions up to $2R_{500}$ are considered. The BCGs are excluded.

the left panel, I show the ratio for all (low-mass and massive) galaxies and on the right panel, only for massive galaxies only. No significant difference is found between isolated and group satellites; the peak of the star-forming ratio in massive galaxies in intermediate-mass clusters remains regardless of the substructure.

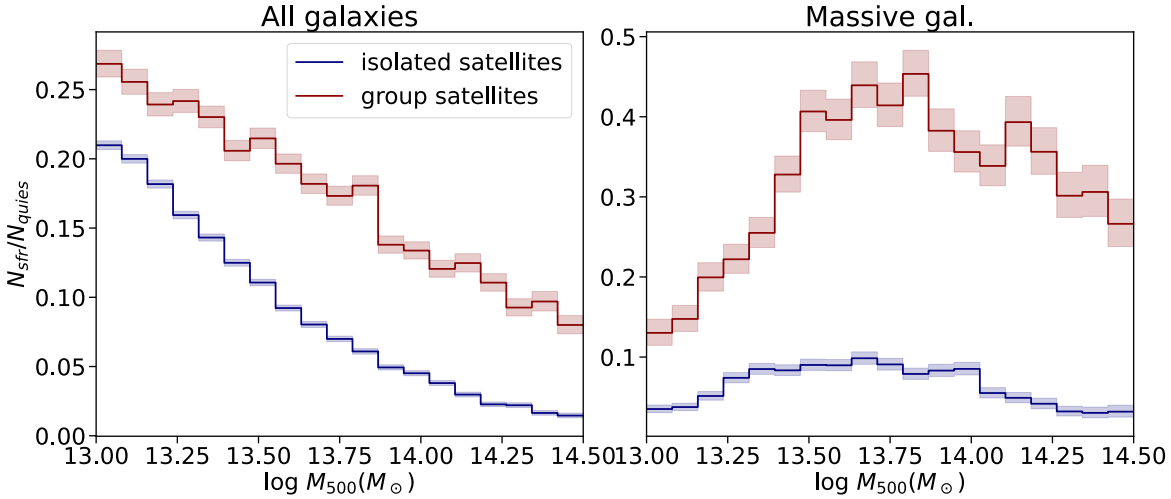

Figure 4.15: The ratio between the number of star-forming (SFR $> 0.02 M_\odot$/yr) and quiescent galaxies as a function of the cluster mass M_{500}, shown for group satellites and isolated satellites (see section 4). The ratio for all galaxies (mostly low-mass galaxies) is plotted on the left panel, and the ratio for massive galaxies is shown on the right panel. Results are shown at low redshift ($z = 0.25$). The BCGs are excluded.

Chapter 5

AGN activity

5.1 Methodology and Black Hole Selection

In this chapter, I explore the properties of black holes, AGNs and the fraction and properties of galaxies that contain them. I use the same sample of galaxies as in chapter 4, with stellar mass threshold $\log M_*(M_\odot) > 10.15$ (or $\log M_*(M_\odot) > 11$ if *massive* galaxies are selected). When I consider only *X-ray bright AGNs* (referred to only as bright AGNs or just AGNs in this chapter), I select black hole particles with X-ray luminosity (in 0.5-10 keV band) $L_X > 10^{42}$ erg/s, unless explicitly said otherwise. Luminosity is estimated from the black hole mass accretion rate, as described in section 2.4. In cases where median black hole mass is shown, I use the black hole mass selection threshold $M_\bullet > 10^8 M_\odot$ in place of the luminosity threshold. Note that one set of black holes is not the subset of the other - we have X-ray bright AGNs with black hole mass below $10^8 M_\odot$, and very massive black holes below the X-ray luminosity limit.

To examine which galaxies contain an AGN (or a SMBH), we first need to match the black hole particles in Magneticum simulations with their parent galaxies, identified by Subfind. I do this by finding the nearest galaxy (among selected) for every selected black hole particle. Since the threshold for galaxy selection is around the black hole seeding stellar mass, almost all AGN hosts are in the selected sample of galaxies. This simple criterion proved sufficiently reliable for matching black holes with their hosts. Even in the densest cluster regions below $0.1R_{500}$, only a few percent of galaxies have the black hole further than 5 kpc from their centre, perhaps meaning that instances where a galaxy is stripped of the stellar mass, falling below our selection limit, and the black hole is unrealistically assigned to other neighbours, are rare and should not drastically affect the results. Less than 0.5 % of black hole hosts contain more than one black hole, most of which are massive galaxies. A few BCGs even contain several black holes, which may be due to recent mergers or small unresolved satellites - in such cases, the central black hole is usually the brightest and often the only one considered to be a bright AGN according to our selection criteria. In a handful of cases where multiple AGNs are assigned to a massive galaxy, I consider the properties of the central one.

Throughout the following sections, I show several types of plots. In some cases, I plot the fraction of galaxies in some population (e.g., in some radial bin) that host an X-ray bright AGN as a function of different quantities (e.g., figure 5.2). The fraction of selected galaxies that are AGN hosts will be henceforth referred to as the *AGN fraction*. In the plots of the AGN fraction, I display the 68% binomial confidence intervals, derived in Appendix A.2. In some plots, the AGN fraction is shown as a function of 2 parameters (e.g., figure 5.15). To avoid plotting regions in parameter space with large statistical uncertainties, I excluded all bins where the 68% binomial confidence interval was larger than 0.2. Similar was done for plots with the median black hole mass of black holes with $M_\bullet > 10^8 M_\odot$, e.g., figure 5.16, where I included only bins with at least 10 black holes. In Appendix D, I show the AGN fraction, median black hole mass and AGN luminosity as functions of all properties of galaxies shown thus far, in the form of corner plots.

In the vast majority of figures in the following sections, I compare the behaviour in different 3-dimensional radial shells, which is particularly useful when one wants to identify processes characteristic for different distances r. However, such plots are difficult to directly compare with observations, where galaxies in 2-dimensional annuli in some redshift interval are considered. To make the results more comparable, I project the galaxies along the cylinder with the length of 7.6 Mpc, centred on the cluster, and consider annuli at different *projected* distances r (figure 5.21). The projection distance 7.6 Mpc matches $6R_{vir}$ of the most massive cluster at $z = 0.90$, which is smaller than the redshift intervals usually used in observations, but that way, the radial trends are less contaminated by the field galaxies.

In figure 5.21, I also calculate the background value of the AGN fraction. The definition of the background value is a bit ambiguous due to the large-scale inhomogeneities (see sections 1.2 and 3.1). When taking the box average, or the box average with clusters excluded, the convergence to the background value is remarkably slow - even at a distance of 20 R_{500}, the fraction is still far from the box average. Therefore, I define the background as the mean fraction in the annulus between 4.5 and 6 R_{500} in groups with $M_{500} > 10^{13} M_\odot$.

5.2 Mass - Luminosity Relation

When discussing AGN luminosity, we need to pay attention to its scaling with black hole mass and consequently with the stellar mass of the host since black hole mass is correlated with stellar mass (or at least with the mass of the bulge component, which is not resolved in our simulations, see Steinborn et al. 2015, Magorrian et al. 1998). From the Bondi model (equation (2.1)), one might expect that the AGN luminosity scales monotonically with black hole mass $M_\bullet$, but the trend is more complex since the black holes are fuelled by their galactic environment.

In figure 5.1, the distribution of black hole masses $M_\bullet$ and their bolometric luminosities is shown at redshifts 0.25 (left panel) and 0.90 (right panel). Eddington luminosity can easily be identified at both redshifts due to an excess of black holes accreting with Eddington mass accretion rate, the highest accretion rate allowed by the subgrid model (equation 2.4). By comparing the two redshifts, we can see the signs of the so-called *anti-hierarchical* growth or *downsizing*. The (comoving) number density of AGNs increases with time, peaks around $z = 1 - 2$, and then declines for $z < 1$. Luminous AGNs are observed to reach their peak of abundance before less luminous AGNs - the massive end of the black hole mass function is already in place at high redshift, while the low-mass end is still evolving[1]. This strong decline in the number of luminous AGN with time is mainly due to the decreasing cold gas content in the vicinity of massive black holes. Even mergers at low redshift tend to be "dry", involving gas-poor galaxies, and do not trigger significant AGN activity. Thus, massive galaxies tend to accrete with a low Eddington ratio and account for some of the moderately luminous AGNs, together with low-mass black holes accreting almost with Eddington mass accretion rate. Massive black holes at late times are mostly former bright AGNs that grew during their active phases. Those conclusions are taken from Hirschmann et al. (2014) where this behaviour is discussed in detail using the same simulations (see also references therein). This behaviour can be partially seen in figure 5.1. At high redshift (right panel) we can see a population of massive SMBHs ($\log M_\bullet(M_\odot) \sim 7.5$) close to the Eddington luminosity, whereas at low redshift (left panel), this population disappears and massive black holes mostly accrete with low Eddington ratios.

At very low $M_\bullet$, we can also clearly notice an excess of black holes that quickly ascend from very low luminosity to Eddington luminosity. Those are recently seeded black holes which rapidly grow with rates allowed by the Bondi model (equaton (2.1)), until the Eddington accretion rate is reached (Steinborn et al. 2015). Another remark we can make in figure 5.1 is that both rapidly accreting black holes at high Eddington ratios, as well as massive black holes with small Eddington ratios, have their expected bolometric luminosity correlated with black hole mass, roughly forming two branches in the $M_\bullet - L_{bol}$ distribution. This is not surprising since the accretion rate always scales with $M_\bullet$ (equation (2.1)). However, it has an important implication. A galaxy with sufficiently high black hole mass will likely be considered a bright AGN host, regardless of the environment. It should be kept in mind that black holes in massive galaxies, accreting with a low Eddington ratio, may, in reality, have lower bolometric luminosity than predicted by the simple model used in this work (section 2.4) since in radiatively inefficient mode, the energy is mostly released in the form of kinetic energy. Indeed, galaxies inside galaxy clusters (especially BCGs) are often radio galaxies (see section 1.6). However, many trends in this chapter are observed even in galaxies hosting black holes of the same mass and are not expected to change drastically if a more accurate model is used.

[1]This behaviour is the opposite of what is usually referred to as hierarchical growth where low-mass objects form first, see section 1.5.

In figure 5.1, I also show the environmental dependence of the $M_\bullet - L_{bol}$ distribution. I display contours where 80% of black holes are found with the largest probability in three radial shells at different r. In the centre of galaxy clusters (blue contours), the population of black holes that accrete almost with Eddington accretion rate is much smaller than on the cluster outskirts. Similar trends will be further discussed throughout this section.

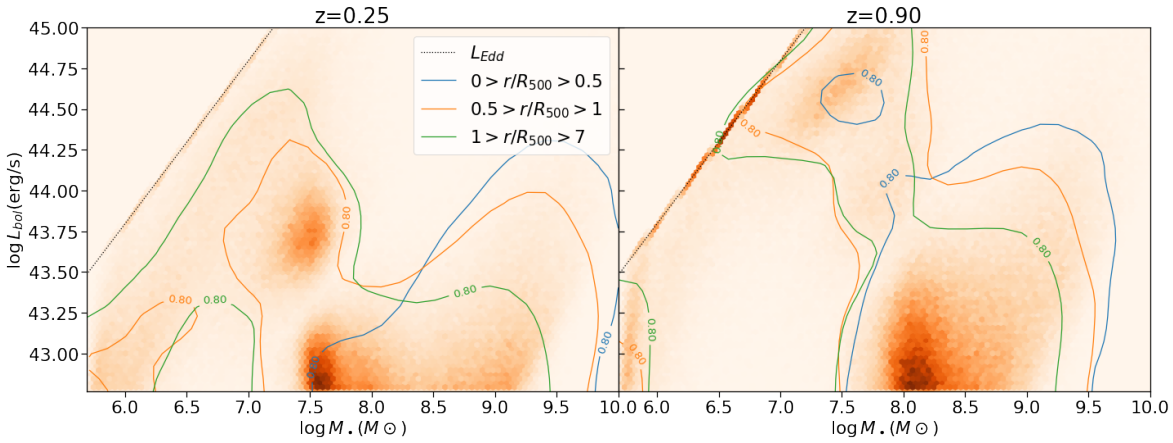

Figure 5.1: Distribution of black hole masses $M_\bullet$ and their bolometric luminosities at low redshift (left panel) and high redshift (right panel). Contours represent the 80% confidence intervals of the black hole parameter distributions in different radial shells around the clusters (radial range is shown in the legend). The 2D color histogram represents the distribution of *all* galaxies in the extended cluster regions (from 0 to 7 R_{500}). The dotted line, traced by an excess of AGNs on the top left of each panel, represents the bolometric luminosity of black holes accreting with Eddington mass accretion rate (equation 2.2). The minimal bolometric luminosity shown ($5.9 \cdot 10^{42}$ erg/s) corresponds to 10^{42} erg/s in 0.5-10 keV band, which is mostly used as the AGN selection threshold in this chapter.

It should also be stressed that very high accretion rates right after the black hole seeding mass are unrealistic and happen due to low black hole seeding mass relative to stellar mass (Steinborn et al. 2018). Nevertheless, AGN activity in low-mass galaxies will still be considered since it can provide some insight into the environmental effects inside the cluster environment, although the exact values of the AGN fraction discussed in the following sections should be taken with a grain of salt. After the first accretion phase, AGN luminosities become highly variable over time steps of ~ 0.1Myr (Steinborn et al. 2018); hence we would unlikely see many signs of environmental dependence by tracking individual black holes. By taking a large sample of black holes in similar conditions, provided by large-scale cosmological simulations, we can hope to unravel some of the tendencies that govern AGN activity in different environments.

5.3 Radial AGN Fraction Profiles

As discussed in section 1.7, SMBHs in the cluster environment are subjected to several processes that can either inhibit or trigger AGN activity, depending on the distance r. In figure 5.2, the AGN fraction is plotted as a function of r for different categories of galaxies. Considering *low-mass quiescent galaxies*, which dominate the inner cluster regions, we notice

a strong decline towards the cluster centre, which is broadly consistent with the decline of the star-forming ratio of low-mass galaxies (figure 4.8). This may imply that the processes in the cluster environment affect star formation and AGN activity similarly. The inner regions of low-mass galaxies are known to be less shielded from the ICM compared to massive galaxies (e.g., Lotz et al. 2019), and if the entire cold gas reservoir is removed, this is expected to show in star formation of the whole galaxy as well as in the central black hole accretion rate. In our numerical scheme, most low-mass galaxies are quenched by the AGN feedback right after the black hole is seeded. However, the extent of this quenching is environment-dependent. In the inner cluster regions, the galaxies can be quenched even before the black hole is seeded, and the AGN activity of newly seeded black hole particles is reduced. Hence the relative variations of the AGN fraction are still expected to reflect environmental processes, acting on both star formation and AGN activity. The plot of the AGN fraction shows us more than the star-forming ratio alone - even if a galaxy is already quenched and below the Subfind SFR resolution, the effects of the cluster environment consistently acting on what remained of its cold gas reservoir continue to be reflected in the AGN activity. Apart from this strong decline in the centre, we can also notice other details. In figure 5.3 I plot the AGN fraction of low-mass galaxies as a function of r, together with the star-forming ratio for comparison. The plateau of the star-forming ratio around and below the virial radius (hypothesized to be a consequence of the in-falling populations in chapter 4) can also be identified in the AGN fraction profiles. Nonetheless, there are some small differences; for example, this plateau seems to be absent in quiescent galaxies at high redshift (right panel of figure 5.3), but even there, it reappears if only isolated quiescent satellites are plotted (not shown explicitly). We should remind ourselves that differences may also arise from the fact that the star-forming population can be kinematically different and more likely infall dominated than the quiescent population (Lotz et al. 2019). In any case, the conclusion remains - it seems that the AGN activity and star formation rate in low-mass galaxies are affected by the cluster environment in a similar way.

The trends found in *low-mass star-forming galaxies* in figure 5.2 (and later 5.8), are also worth discussing. At low redshift (left panel, orange plot), a broad peak of the AGN fraction can be detected between 1 and $2R_{500}$, roughly centred around 1.3 R_{500}. Before discussing any environmental causes, we first need to consider something that can significantly impact the observed profiles. In chapter 4, I already pointed out the impact of mass segregation. Since the black hole masses scale with the stellar masses of the host galaxies (Steinborn et al. 2015, Magorrian et al. 1998) and since we have shown in section 5.2, that the AGN luminosity scales with black hole mass, having galaxies of different masses at different r could be reflected in the AGN fraction variations, without the need for direct environmental impact. In figure 5.4 I show the AGN fraction as a function of r for two narrow stellar mass ranges (subsets of star-forming and quiescent populations in figure 5.2). We can see that the profiles of the low-mass star-forming population in figure 5.2 are at least partially a consequence of stellar mass segregation. Low-mass galaxies are more easily quenched (shown in chapter 4), hence

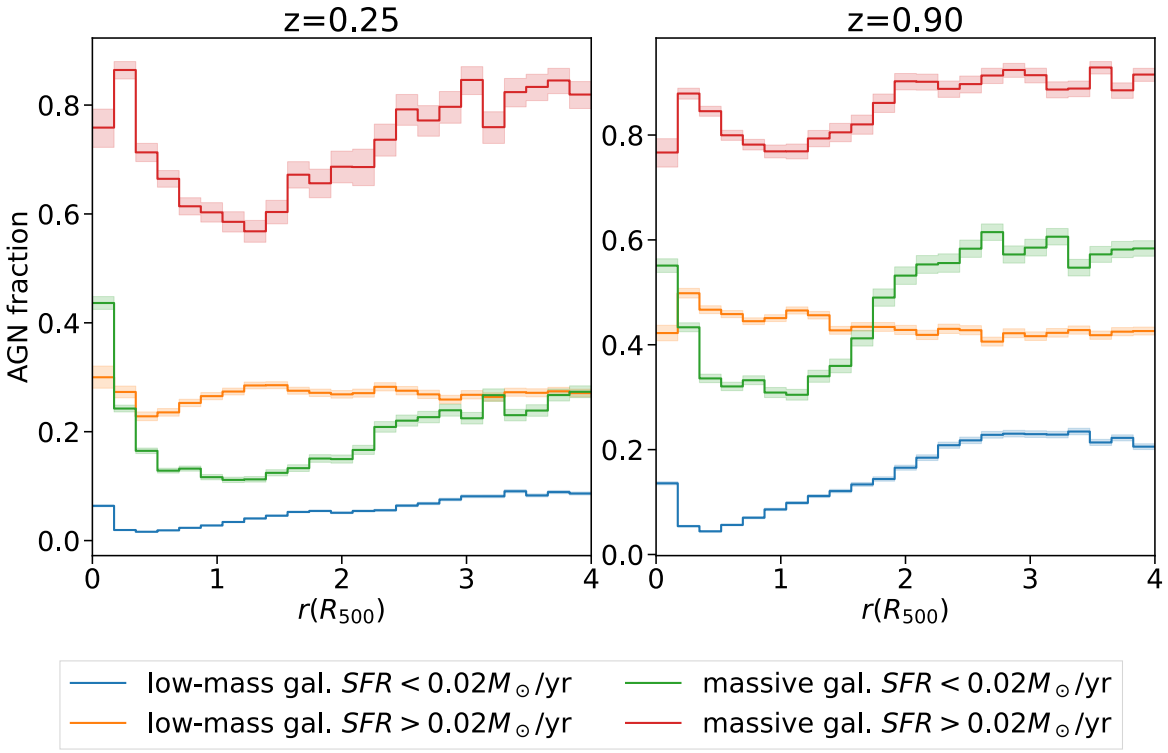

Figure 5.2: Fraction of galaxies containing an X-ray bright AGN as a function of r. Results are shown at low redshift (left panel) and high redshift (right panel), for all galaxies, only massive, quiescent and star-forming galaxies. 68% binomial confidence intervals are shown (see Appendix A.2). The BCGs are excluded.

the star-forming population in the inner regions probably consists of more massive galaxies, hosting more massive black holes, which appears as an excess of AGN activity in figure 5.2. But when selecting galaxies with constant mass (figure 5.4), we can see that the AGN activity in low-mass star-forming galaxies decreases below $2R_{500}$, similarly to quiescent galaxies. This means that the AGN activity in low-mass galaxies is suppressed in the cluster centre, even if the galaxies retain enough gas to be still considered star-forming.

Massive galaxies display a somewhat different behaviour than low-mass galaxies. In figure 5.2 we can see a gradual decline towards the inner regions, with a minimum between 1 and 2 R_{500}, followed by an increase in the centre. This shape is found in star-forming and quiescent galaxies and is not caused by different stellar masses (see figure 5.4). In figure 5.5, the AGN fraction is plotted against the star-forming ratio in massive galaxies. Curiously, the AGN activity profile does not match the star formation rate at all. It seems like one is almost a mirror image of the other; the minimum of AGN activity around $1R_{500}$ is contrasted by significantly elevated star formation in massive galaxies and vice versa. This could indicate the causal connection between the two, with AGN suppression after the infall allowing higher levels of star formation. We can also see that the profiles are slightly shifted; the minimum of AGN activity precedes the maximum of star formation (is found at higher r), which could point to the delayed effect of AGN activity on star formation rate (e.g., Florez et al. 2020). While the direct causal connection is not entirely ruled out in this work, I will show in the

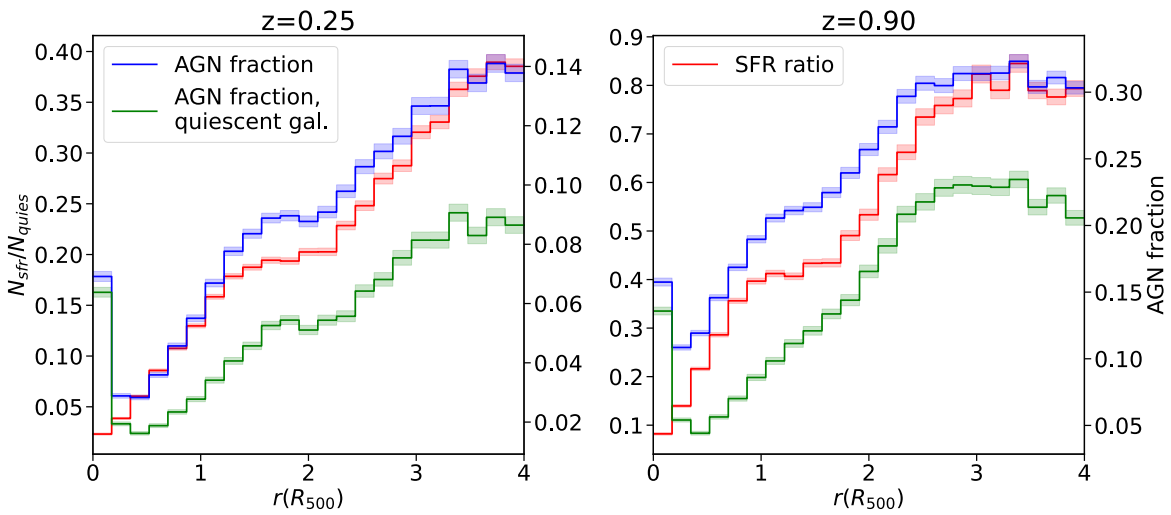

Figure 5.3: The AGN fraction of *low-mass* galaxies (all galaxies, and just quiescent galaxies, taken from figure 5.2), and the ratio between low-mass star-forming and low-mass quiescent galaxies, taken from figure 4.8, plotted against each other for comparison. The scale on the left represents the star-forming ratio, and the scale on the right the AGN fraction. The profiles are shown at low redshift (left panel) and high redshift (right panel). The BCGs are excluded.

following section that it cannot be solely responsible for the difference. The profiles in figure 5.5 probably suggest (alternatively or in addition) that the AGN activity and star formation rate are not affected by the same processes to the same extent. This is not unimaginable since, apart from the availability of cold gas (and its compression) that drives star formation, AGN activity also requires the loss of angular momentum and transport of the gas towards the galactic centre. One possible explanation would be that the abundance of galaxy mergers and interactions on the cluster outskirts keeps the AGN fraction (and star-forming ratio) high. Below the virial radius, merging activity seizes due to higher velocity dispersion, and AGN activity drops. On the other hand, ram pressure may compress the gas and trigger star formation rate in massive galaxies, as discussed in Chapter 4. Below $1R_{500}$, the expected AGN activity in galaxies increases again, which can potentially prevent or decrease star formation, in addition to the environmental effects. It should be stressed that in order to confirm this, AGN activity and star formation rate in individual galaxies should be tracked during their infall. This was partially done in Lotz et al. (2019), where no increase in star formation rate during infall is found, which proves the need for a more in-depth analysis.

The increase of AGN activity in massive galaxies from R_{500} down to the cluster centre, observed in figure 5.2, is worth examining closely. The environment in the cluster centre is densely packed with galaxies, which could lead to frequent interactions (harassment), possibly triggering the AGN. However, while this can contribute to the increase, I will try to show that this is probably not the only cause. In figure 5.6 I plot the median black hole mass $M_\bullet$, hosted by galaxies in some narrow stellar mass range. It seems that in the cluster centre, galaxies with some stellar mass M_* (and thus also galaxies *above* some M_*) on average host more massive black holes compared to galaxies with the same M_* in the outer regions. This trend could emerge due to several reasons. One is a *different co-evolution* of stellar

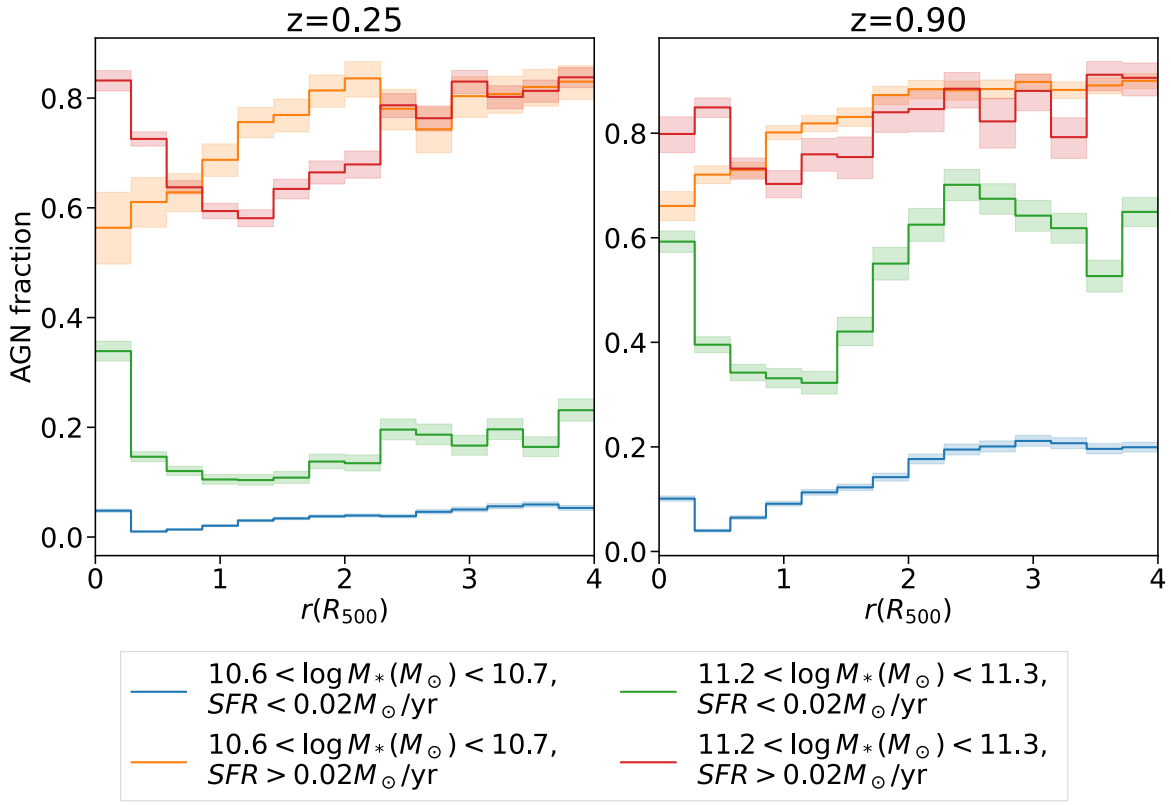

Figure 5.4: Fraction of galaxies containing an X-ray bright AGN as a function of r, shown for galaxies in two *narrow mass ranges* at low and high redshift. Galaxies are divided into star-forming and quiescent populations. The BCGs are excluded.

and black hole mass of galaxies in the inner regions. If the black hole mass accretion rate in the inner regions was on average higher than in the outer regions, relative to the star formation rate, perhaps due to environmental conditions, black holes in the inner regions would eventually outgrow their outer-region counterparts. This would then increase the mass difference further since more massive black holes in the inner regions would grow even faster. Another mechanism causing the mass difference is *tidal stripping*. I have already shown its significance in chapter 4, and will further prove it in section 5.4. Tidal stripping decreases the M_* of the galaxies while their black hole masses remain unchanged, causing an overall increase in $M_\bullet$. Considering the black hole mass-luminosity relation, discussed in section 5.2, this central increase of black hole masses could play a crucial role in the central excess of AGN activity observed in galaxies with $M_* > 10^{11} M_\odot$. Again we should remember that the central X-ray excess may not be so drastic in reality since the Eddington ratios become small, and the radiative efficiency may be smaller than assumed here.

The black hole mass increase, shown in figure 5.6, further emphasizes the strength of the environmental effects in the inner cluster regions. Despite more massive black holes, low-mass galaxies still show a decrease in the AGN fraction almost down to the cluster centre. This central suppression can be even better seen in figure 5.7, where I show the AGN fraction as a function of stellar mass M_* in the cluster centre (right panel) and in the field (left panel). Whereas galaxies in the field show significantly enhanced AGN fraction after the

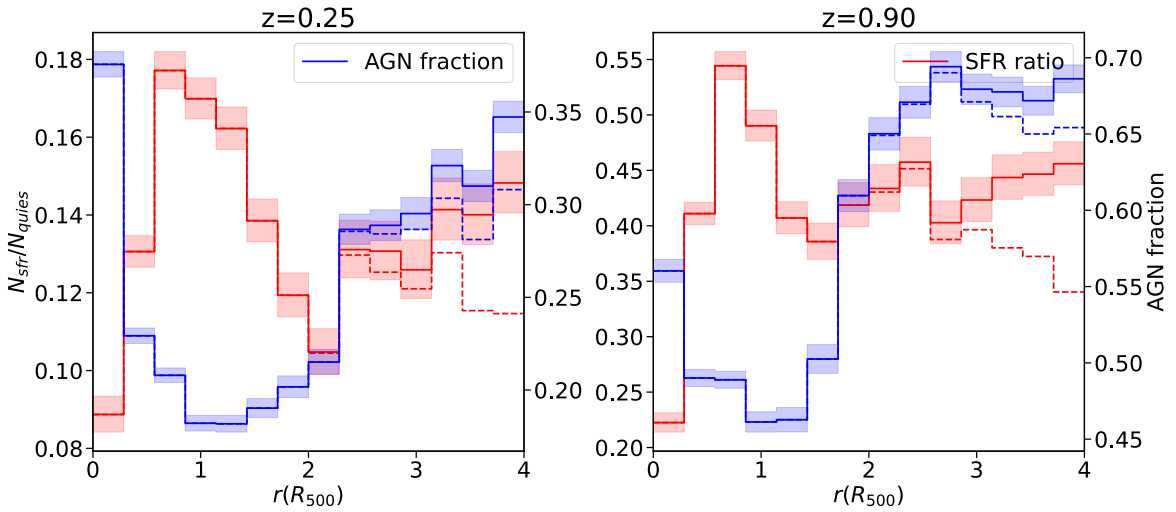

Figure 5.5: The AGN fraction of *massive* galaxies, and the ratio between the number of massive star-forming and massive quiescent galaxies, taken from figure 4.8, plotted against each other for comparison at low redshift (left pamel) and high redshift (right panel). The scale on the left represents the star-forming ratio, and the scale on the right the AGN fraction. The BCGs are excluded. The dashed lines represent the profiles where the BCGs of the neighbouring groups with $M_{500} > 10^{13} M_{\odot}$ are also excluded.

black hole seeding stellar mass, where low-mass black holes accrete almost at the Eddington ratio, galaxies in the cluster centre hardly show any enhancement. It can be noticed how black hole mass dependence becomes a decisive factor in determining the AGN fraction at larger M_*. In galaxies with $M_* > 10^{11} M_{\odot}$, even small changes in $\log M_*$ can resemble the drastic difference between the environment in the cluster cores and in the field in terms of the AGN fraction.

In figure 5.8 I plot the AGN fraction as a function of r in the innermost regions (below $0.5R_{500}$). We can again notice the central increase of the AGN fraction in quiescent low-mass and massive galaxies, probably due to the increase of black hole masses as mentioned in the paragraphs above (see figure 5.6). Interestingly, the profiles of star-forming galaxies show a different behaviour - they ascend only down to around $0.3R_{500}$, followed by a rapid decline in the cluster centre. This decline does not seem to be a consequence of different M_*; it can be noticed even if a narrow M_* range is chosen (verified separately and not shown in this work). It also goes against the median black hole mass, which increases down to the very centre. Identifying the exact reason is beyond the scope of this work; in order to do that reliably, I would perhaps first need to revise the method of matching black holes with their parent galaxies.

In figure 5.9 I explore how the substructures affect the AGN fraction as a function of r, by separately considering isolated and group satellites. In *low-mass* galaxies, the behaviour looks somewhat similar regardless of the substructure. Interestingly, the plateau in the AGN fraction is more clearly observed in isolated satellites and not in (more likely infalling) group satellites. In figure 4.10 we have seen that the central decline in SFR is delayed significantly in

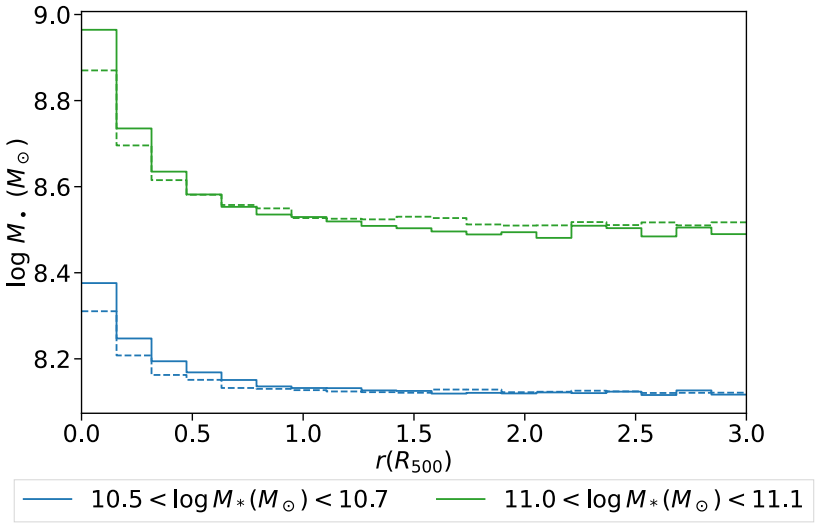

Figure 5.6: Median black hole mass, of black holes with $M_\bullet > 10^8 M_\odot$, found in galaxies in two narrow M_* ranges at different clustercentric distances r. Solid lines are used for galaxies at $z = 0.25$ and dashed lines at $z = 0.90$.

low-mass group satellites (star-forming fraction is almost constant down to $0.7R_{500}$, followed by rapid quenching in the centre). The AGN activity seems to be suppressed much more gradually towards the centre. This difference may insinuate that the processes in a locally denser group environment affect the AGN activity in the galactic centre differently than the overall star formation rate of the galaxy (e.g., harassment and mergers, see sections 1.5 and 1.7). Perhaps the shielding from the ICM inside the group atmospheres plays a more important role in star formation than in AGN activity. The exact mechanism causing the gradual decline of the AGN fraction in contrast to the extended survival of star formation in group satellites should be explored further in future works.

Focusing on *massive* galaxies in figure 5.9, we notice that the overall AGN fraction is higher in group satellites compared to isolated satellites, which agrees with what was claimed in section 1.5, the group environment with large local density and small velocity dispersion promotes galaxy interactions and mergers. I verified that the difference is not a consequence of different masses of massive group centrals and isolated satellites - the difference remains even if a very narrow mass range is chosen (not shown explicitly). Nevertheless, the profiles are qualitatively similar - massive galaxies have a minimum of AGN activity between 1 and $2R_{500}$, regardless of whether they are isolated or a part of some smaller group. This similarity is in strong contrast to the star-forming ratio of massive galaxies (figure 4.10), where substructures profoundly influence the behaviour, either due to different kinematics or due to the local environment (discussed in section 4.3). AGN activity, at least in terms of general radial trends, does not seem to be as strongly influenced by the substructure but rather by the global cluster environment; conditions on the outskirts and in the central regions seem generally more suitable for AGN activity.

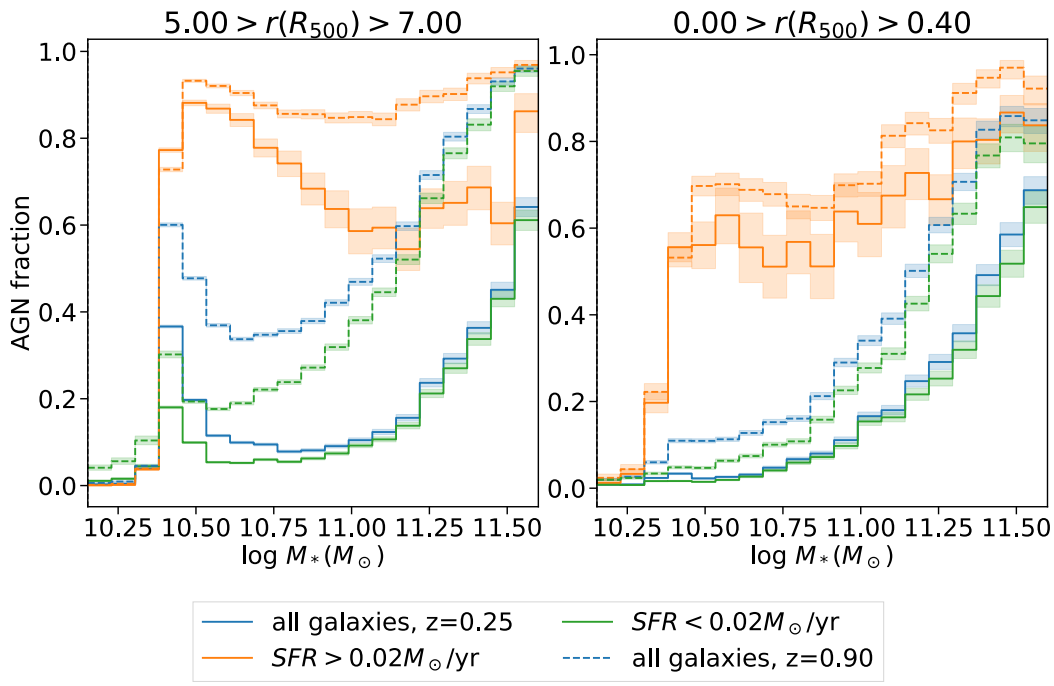

Figure 5.7: The AGN fraction as a function of stellar mass M_* of galaxies in the field (remote regions between 5 and $7R_{500}$, shown on the left panel) and in the cluster centre (below $0.4R_{500}$, right panel). The fractions are shown for star-forming, quiescent and combined samples of galaxies at low redshift (solid lines) and high redshift (dashed lines).

So far, I have considered all clusters with $M_{500} > 10^{13} M_\odot$. It is reasonable to check if this behaviour changes in more massive clusters. In figure 5.10 I show radial profiles of low-mass and massive galaxies in clusters in four M_{500} ranges in different panels. Qualitatively, the behaviour does not depend on M_{500}, except that the suppression of AGN activity is stronger in massive clusters. In clusters with $M_{500} < 5 \cdot 10^{13}$ (upper left panel) we can barely speak of the AGN activity suppression in the inner regions, whereas in most massive clusters (bottom right panel), massive galaxies are up to 4 times less likely to host an AGN around $1R_{500}$ than on the outskirts. We can add a tentative observation that the delay in the AGN fraction drop, found in the profile of low-mass galaxies around $2R_{500}$, is more pronounced in low-mass clusters below $10^{14} M_\odot$. In clusters between 10^{14} and $5 \times 10^{14} M_\odot$, the decline in the central regions is smoother.

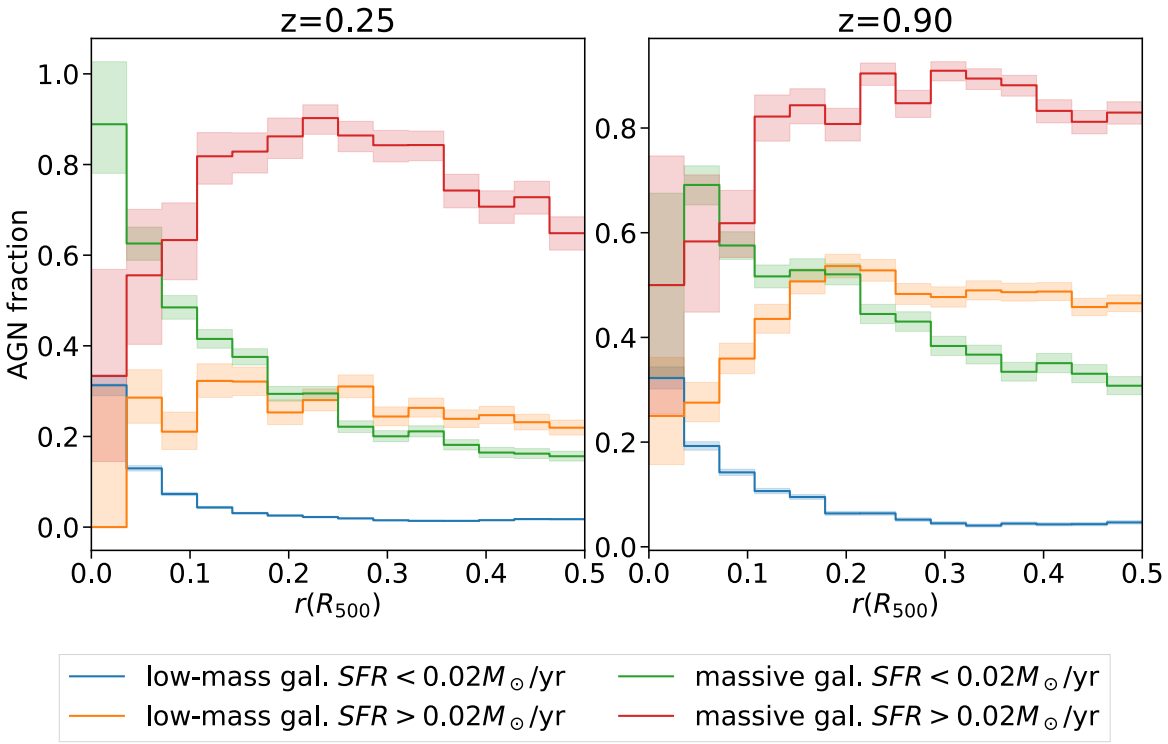

Figure 5.8: Fraction of galaxies containing an X-ray bright AGN as a function of r in the innermost cluster regions. Zoomed-in version of figure 5.2, showing low redshift profile on the left and high redshift profile on the right. The BCGs are excluded.

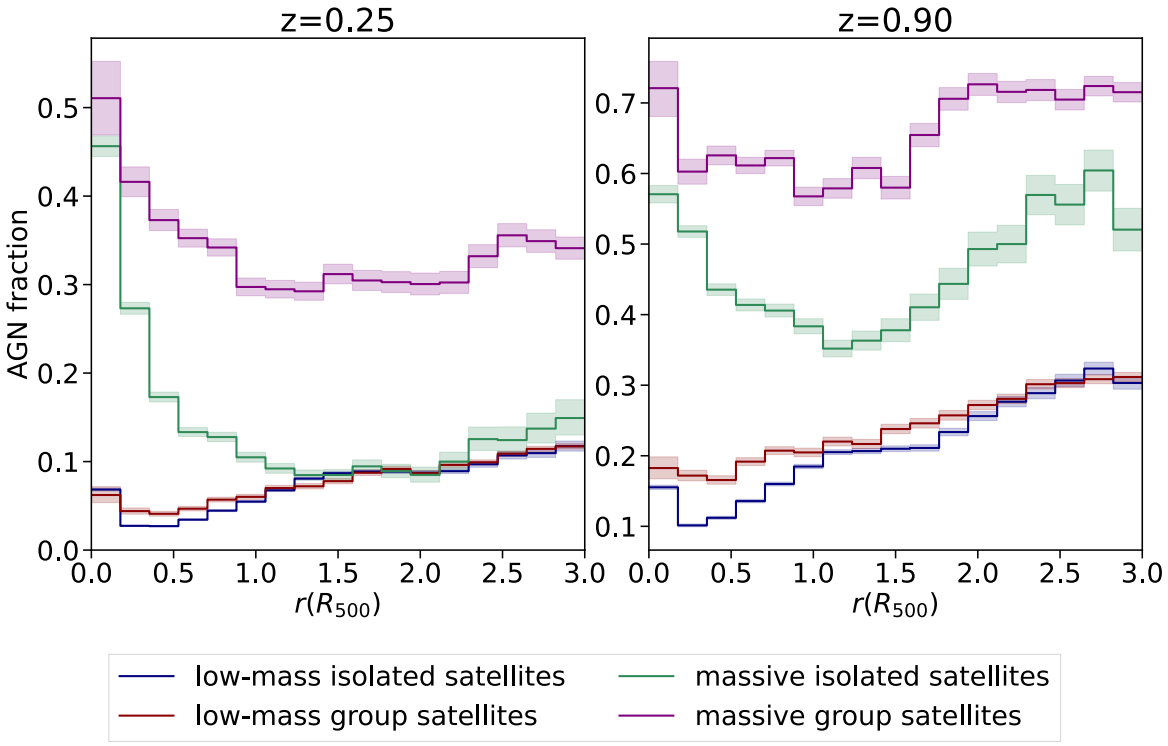

Figure 5.9: The AGN fraction as a function of r plotted for group satellites and isolated satellites (see section 4). Results are shown for low-mass and massive galaxies at low redshift (left panel) and high redshift (right panel).

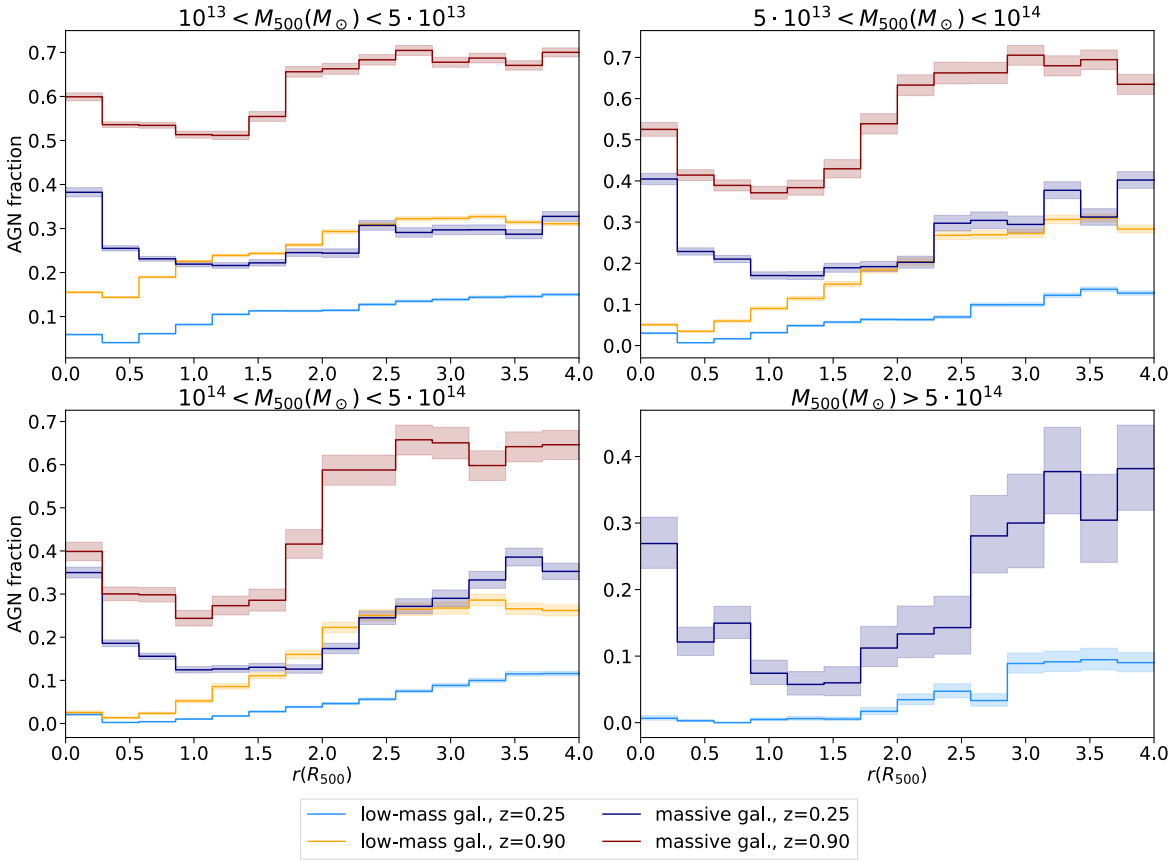

Figure 5.10: The AGN fraction as a function of r, plotted for low-mass and massive galaxies at low and high redshift. On each panel, clusters of *different masses* M_{500} are shown. Clusters with $M_{500} > 5 \cdot 10^{14} M_\odot$ at high redshift are omitted since very few are found in box 2b, and the profiles are dominated by statistical noise.

5.4 Effects of the Local Density

In figure 5.11, the AGN fraction as a function of the distance to the nearest neighbour d_n is shown in the inner cluster regions (right panel) and in the field (left panel). There are many similarities between the effects of the local density on the AGN fraction and the star-forming ratio, shown in figure 4.12. Inside the clusters, galaxies in the denser environment seem to have increased both star formation rate and AGN activity. Similar can be seen in the field. There are, however, some subtle differences. In *low-mass* field galaxies, the proximity of another galaxy (d_n below 30 kpc) can increase the probability for AGN activity much more steeply than it increases in the star-forming ratio. Very closely interacting galaxies have the highest AGN fraction - even higher than secluded galaxies at large d_n, where the star-forming ratio is the highest. In *massive* galaxies, the behaviour in both the field and in the cluster resembles the star-forming ratio, which is interesting, considering how differently they depend on position r (figure 5.5). That means that it is not the change in the local density with r, that causes the difference between star formation and AGN activity profile in massive galaxies - it is probably the global conditions at some r (ICM density, velocity dispersion, tidal stripping), influencing the AGN activity and star formation differently.

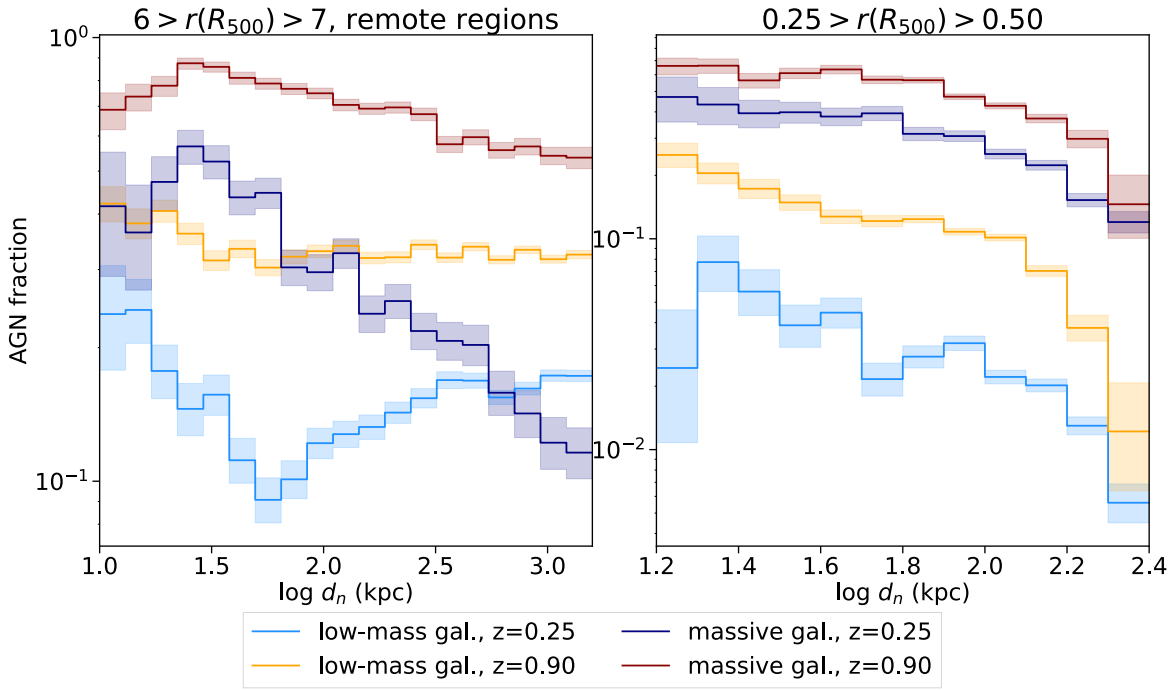

Figure 5.11: The AGN fraction as a function of the distance to the nearest neighbour d_n at low and high redshift for low-mass and massive galaxies. On the left panel, remote regions between $6R_{500}$ and $7R_{500}$ of considered groups are selected, and on the right panel, I choose the regions between 0.25 and $0.5R_{500}$. Parameters match the figure 4.12, to allow for direct comparison to star formation.

The large variations in the AGN fraction with local density, seen in figure 5.11, may indicate the crucial role of harassment and galaxy interactions in AGN triggering, but as before, there are other factors to consider. I first verified that the profiles look qualitatively similar if galaxies in narrow M_* ranges were selected (not shown explicitly), thus ruling out

the significant impact of the stellar mass segregation. In figure 5.12 I show the median black hole mass of galaxies with constant stellar mass M_* as a function of d_n in the inner cluster regions (right panel) and in the field (left panel). We can see that the galaxies of the same mass host more massive black holes if they are in a locally denser environment, probably due to the environmental effects mentioned in section 5.3. This difference is not as drastic as the increase in the cluster centre (seen in figure 5.6), and in some cases, barely noticeable (e.g., in massive field galaxies at low redshift). Thus I do not believe it can explain all of the trends alone; the direct environmental effects and galaxy interactions could still play a decisive role. This is further supported by the similar trends in the star-forming ratio (figure 4.12), which are not directly affected by the black hole mass.

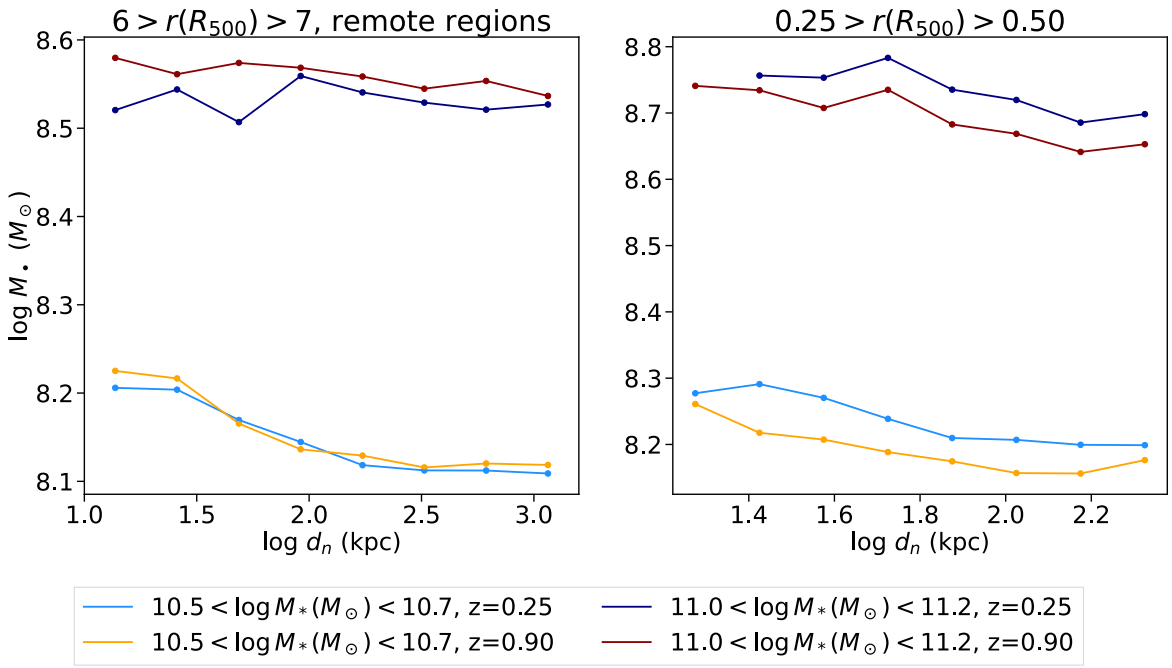

Figure 5.12: Median mass of black holes (with $M_\bullet > 10^8 M_\odot$), hosted by galaxies in two narrow stellar mass M_* ranges, as a function of the distance to the nearest neighbour d_n. Data points are placed at the centres of bins in which the median mass was computed. I do not show the bins containing less than 10 black holes. Results are shown for the field galaxies (left panel) and the inner cluster regions (right panel) at low and high redshift. The figure can be compared with the AGN fraction as a function of d_n shown in figure 5.11.

We should also remember that the fraction of group satellites is larger at a smaller distance to the nearest neighbour d_n. So it may be possible that the variations of the AGN fraction in figure 5.11 with d_n reflect the substructure membership. In figure 5.13, I show the AGN fraction and star-forming ratio as functions of d_n for *massive group* satellites and *massive isolated* satellites. The relatively narrow d_n range was chosen so that both populations are sufficiently abundant to form statistically meaningful trends (note that at lower d_n almost all massive galaxies are group satellites). Generally speaking, if a galaxy is found in a group environment, both the star-forming ratio and the AGN fraction increase drastically with the local density, both on the outskirts and in the inner cluster regions. The isolated satellites behave differently - it is clear that they are less susceptible to the local density, traced with d_n,

than group satellites. This has several possible explanations. As mentioned before, groups of galaxies have their own atmosphere, which can shield the galaxies from the effects of the ICM, and the local density inside groups could be a proxy for the gas density inside the group halo and the degree of shielding from the ICM. Alternatively (or additionally), the galaxies bound together in a smaller group have a lower velocity dispersion (see section 1.5), meaning that they can interact more strongly compared to the unbound galaxies with low d_n due to coincidental flybys. Note that coincidental flybys at a distance of almost Mpc are not expected to cause any significant gravitational interaction.

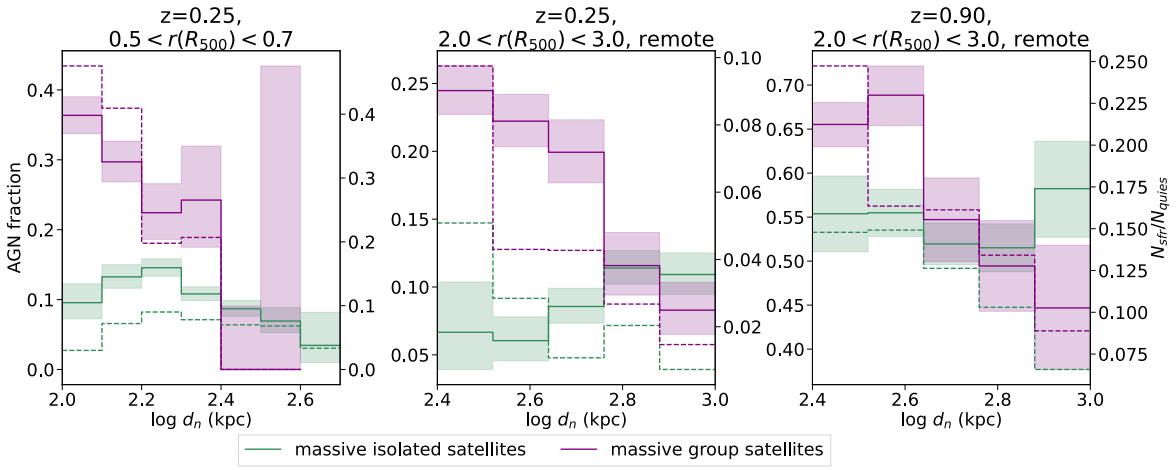

Figure 5.13: The AGN fraction in massive galaxies (solid lines and confidence intervals, scale on the left side of the panels) and the ratio between massive star-forming and quiescent galaxies (dashed plot, scale on the right side) as functions of the distance to the nearest neighbour d_n, plotted for isolated and group satellites. Galaxies are taken from two narrow radial shells, one inside the cluster (left panel) and the other on the outskirts (middle and right panel). Remote regions are chosen so that the profiles are not disturbed by the vicinity of other massive groups and clusters. The left two panels show the profiles at low redshift and the panel on the right at high redshift.

To once again demonstrate which of the radial features are a consequence of the local density and which are a consequence of the global environment, I again plot the star-forming ratio and the AGN fraction of massive galaxies as a function of r, like in figure 5.5, but this time I display only galaxies with a constant distance to the nearest neighbour d_n, around 70 kpc (figure 5.14). We can see that both the decline of AGN activity inside the cluster and the increase in the star-forming ratio can still be identified, with amplitudes of features not drastically different from those in figure 5.5. However, the central rise of the AGN fraction is almost absent, again pointing to the importance of the local density and related processes that increase black hole mass (e.g., tidal stripping).

In figure 5.15, the AGN fraction is shown as a function of r and d_n at low and high redshift and for low-mass and massive galaxies. Here, we can even better see the competition between the higher local density enhancing the AGN activity and the suppression of AGN activity at smaller r due to the global cluster environment. As the local density of galaxies increases towards the inner regions, the resulting radial profile results from the trade-off between both

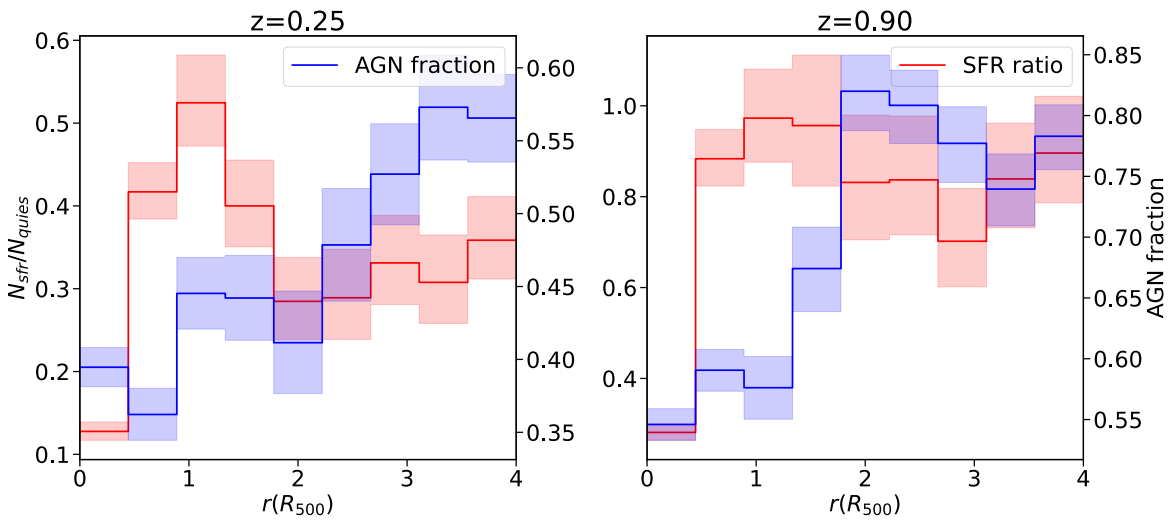

Figure 5.14: The AGN fraction of massive galaxies with *constant local density* ($1.8 < \log d_n\,(\mathrm{kpc}) < 1.9$), and the ratio between massive star-forming and massive quiescent galaxies. The figure can be compared with figure 5.5, where no d_n selection is made.

trends. In low-mass galaxies (left panels), suppression due to the cluster environment prevails, resulting in the declining radial profiles seen above. In massive galaxies (right panels), the effects of the local density appear to be stronger - the radial suppression is outweighed by the strong AGN activity at low d_n, causing the ascending profile with decreasing r in the inner regions of figure 5.2. As we have seen, this may be due to higher black hole masses countering the environmental suppression in the centre.

In figure 5.16 I plot the AGN fraction and the median black hole mass as functions of r and stellar mass M_*. Here we can see further evidence for tidal stripping. Even galaxies very close to the black hole seeding stellar mass already host relatively massive black holes (see bottom panels). The lack of gas and heavily suppressed AGN activity in the cluster centre, shown throughout this chapter, make it improbable that the central increase of the black hole mass happens due to faster black hole growth relative to stellar mass growth. The excess observed in figure 4.5 and discussed in section 4.3 further indicates that those black holes had already reached the $M_\bullet - M_*$ relation (Steinborn et al. 2015, Magorrian et al. 1998) in the past and had quenched the host galaxy. The generally increasing $M_\bullet$ in the centre thus probably reflects the stripping of the stellar mass. I also verified that this is not simply a consequence of the Subfind algorithm, falsely assigning parts of the galaxy to some other halos in the dense central environment, which could also appear as an increase of the black hole mass. However, even if I use the maximal circular velocity as a proxy for the mass of the galaxy (not shown explicitly), which is less susceptible to spurious particle membership, I find that the black hole masses of galaxies with the same M_*, are larger in the cluster centre, by the same order of magnitude as in figures 5.6 and 5.16. This further proves that the galaxies in the centre indeed have their mass stripped, causing the apparent increase of AGN activity. In figure 5.16, we can also see some of the trends discussed in this chapter, such as the effect of the increased black hole mass in the centre on AGN activity. It seems that the

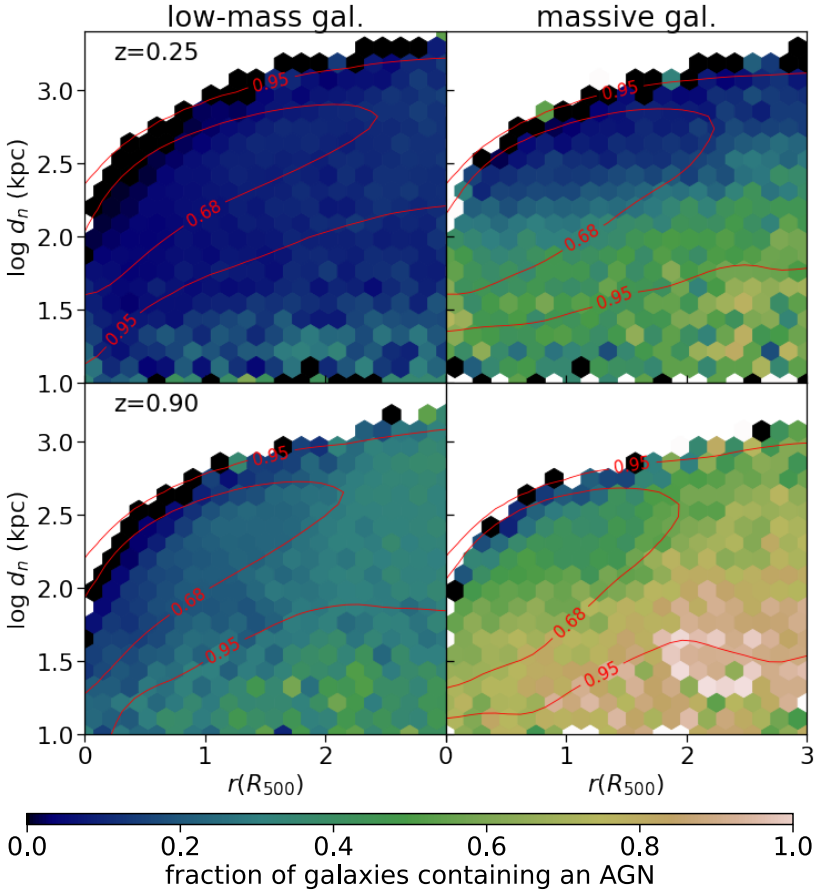

Figure 5.15: The AGN fraction as a function of the clustercentric distance r and the distance to the nearest neighbour d_n. The fraction is shown for low-mass galaxies (left panels) and massive galaxies (right panels) at low redshift (upper panels) and high redshift (bottom panels). Red contours represent the distribution of galaxies, also shown in figure 4.2.

AGN fraction very accurately traces the black hole mass, proving its dominant influence on the central rise of the AGN fraction in massive galaxies. We can also verify that the black hole mass segregation cannot explain trends at higher r.

We can obtain further insight into the effects of d_n if we plot it together with stellar mass M_*. In figure 5.17 I show the AGN fraction as a function of d_n and stellar mass M_* in the inner cluster regions (left panels), on the outskirts (middle panels) and in the field (right panels). Here, the immense impact of the local density on the AGN fraction can be seen especially clearly. While the environment entirely suppresses low-mass galaxies in the inner regions, the increase of AGN activity with local density and stellar mass in very massive galaxies qualitatively does not change. d_n and M_* seem to be the driving factors in AGN activity of massive galaxies, affecting it universally and not just in the central regions, whereas the global environment and the cluster atmosphere probably dominate AGN activity in low-mass galaxies. Again, note that apart from the central regions, most of the galaxies with d_n below a few hundred kpc are bound to smaller groups of galaxies.

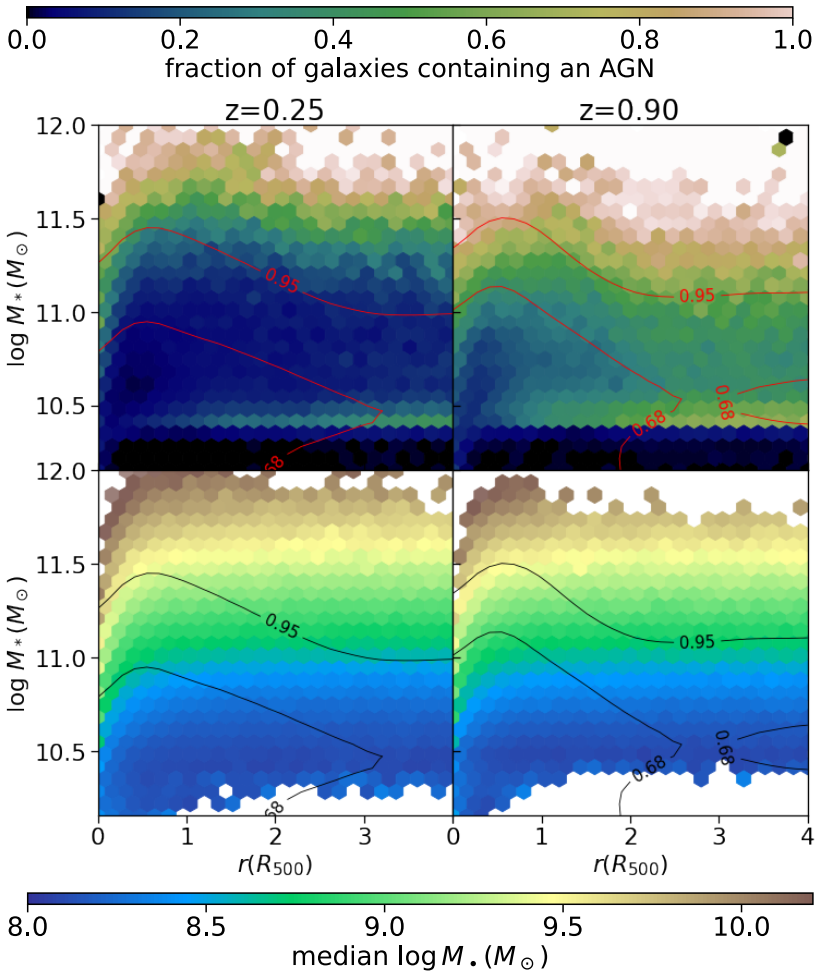

Figure 5.16: The AGN fraction (upper panels) and the median black hole mass (bottom panels) as functions of the clustercentric distance r and stellar mass M_* at low redshift (left panels) and high redshift (right panels). The contours represent the distribution of galaxies.

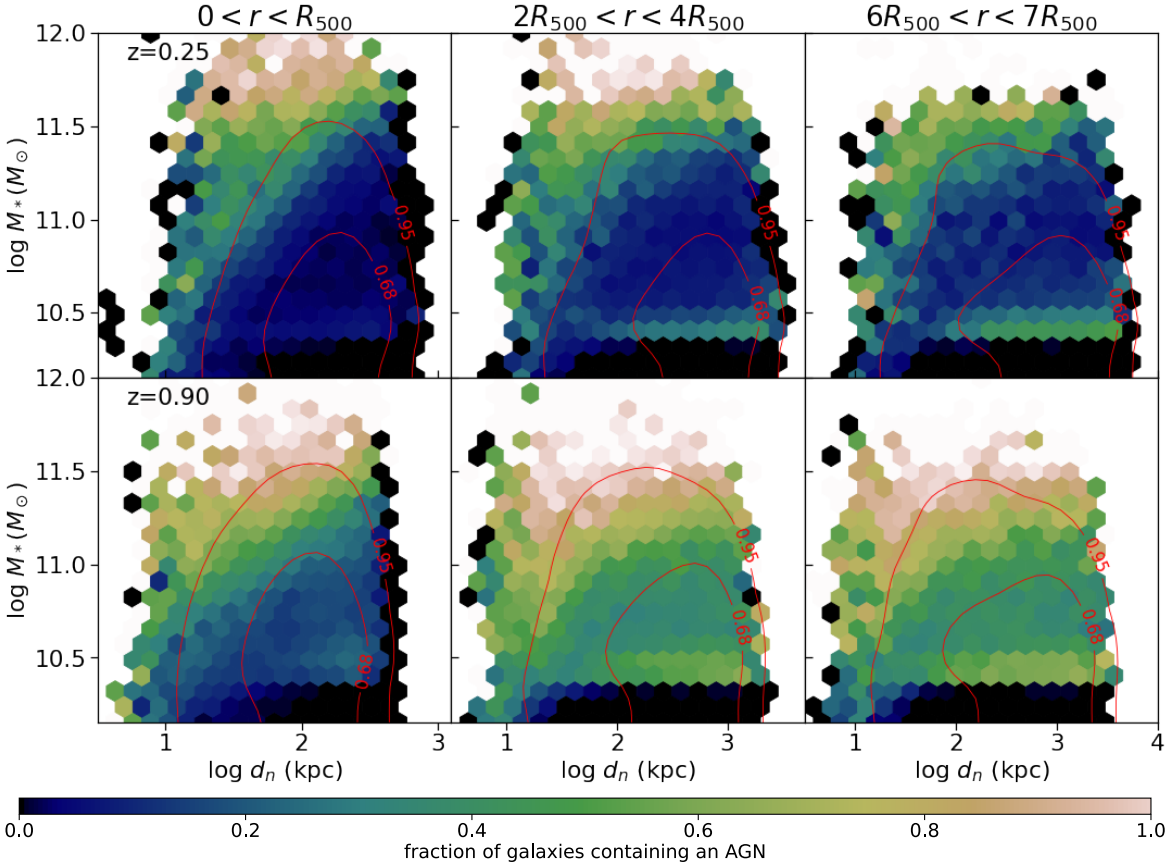

Figure 5.17: The AGN fraction as a function of the distance to the nearest neighbour d_n and stellar mass M_*. The contours represent the distribution of galaxies. Results are displayed for different radial ranges (different columns). In the outer regions (rightmost panels), only remote regions were selected to remove the contributions of other neighbouring massive groups and clusters. The upper row shows the fraction at low redshift and the lower row at high redshift. Mind that the d_n range of each panel is adjusted to show the bulk of the galaxies.

5.5 Extended Radial Profiles

Thus far, we mostly focused on the inner cluster regions below the virial radius and only briefly mentioned the behaviour far away from the cluster regions. When talking about the radial profiles beyond $2R_{500}$, we need to consider the large-scale surroundings of the clusters containing other neighbouring groups and clusters. As outlined in chapter 3 and already done with the star-forming ratio in figure 4.7, I separate the radial AGN fraction profile of the *overlapping* regions containing the neighbouring cluster regions, and the *remote* regions, far from the neighbouring clusters. The AGN fraction as a function of r up to $8R_{500}$ is shown in figure 5.18. The profile of *low-mass* galaxies (left panels) is almost identical to the profile of the star-forming ratio in figure 4.7, with central suppression of AGN activity, which is reflected in a drop of AGN activity at large r in the overlapping population. The excess of AGN activity between 2 and $4R_{500}$ can be explained with geometric overlaps, as shown in chapter 3, and does not necessarily require different physics on the outskirts of clusters. This excess is also the reason for the subtle peak in the combined profile (it is absent in the profile of remote regions).

Considering *massive* galaxies (right panels), we can notice similar behaviour in the overlapping population, especially when the contribution of the neighbouring BCGs is removed. Interestingly, the isolated population also clearly shows an excess of AGN activity on the outskirts. The question may arise whether this excess appears due to geometric overlaps with smaller groups ($M_{500} < 10^{13} M_{\odot}$) in remote regions, but in figure 5.19 I show that this is not the case (I plot the radial profile of isolated massive satellites in remote regions). Even galaxies that do not belong to any group with several galaxies show signs of an AGN excess on the outskirts. Hence, this excess most likely shows that the outskirts of clusters are a particularly suitable environment for AGN activity (as proposed in section 1.7). We should also remember that at the same r, an excess of the star-forming ratio was found (figure 4.8), meaning that unlike in the inner regions, the conditions in the outer regions may trigger both AGN activity and star formation. We expect this excess of AGN activity to be particularly noticeable in relaxed clusters in isolation that do not contain massive groups in their vicinity. If the profiles of all clusters are combined (black plots in figure 5.18), the excess of AGN activity is not discernible anymore at low redshift (upper right panel); the profiles of overlapping and remote regions have their peaks at different r, and the physical excess in remote population is countered by the rapid ascent of the AGN fraction in the overlapping population (probably due to geometric overlaps). Tentative signs of the AGN excess can still be identified in the combined profile at high redshift (bottom right panel), since the peak due to geometric overlaps coincides with the excess in the isolated population, but even so, we might not have put much attention to it had the large scale environment not been carefully taken into account.

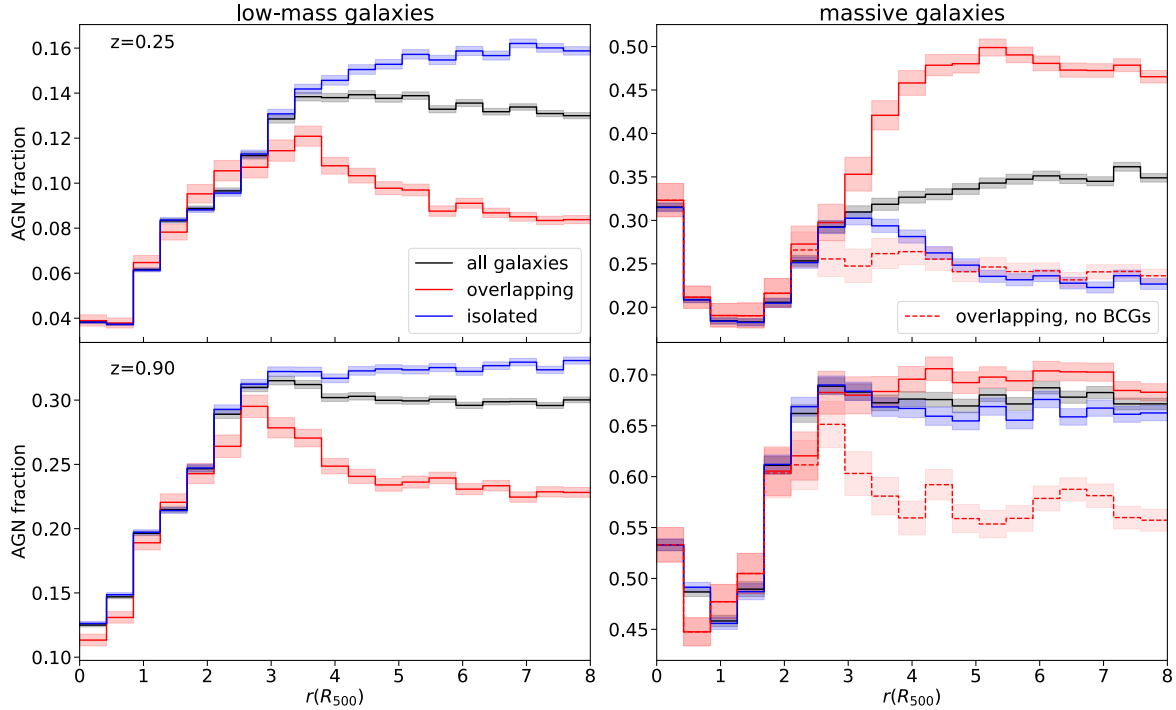

Figure 5.18: Fraction of galaxies hosting an X-ray bright AGN as a function of clustercentric distance r. Low-mass galaxies with $10.15 < \log M_*(M_\odot) < 11$ are plotted on the left, and on the right, only galaxies with $\log M_*(M_\odot) > 11$ are shown. Results are shown for low and high redshift and for overlapping and remote regions (with overlapping distance $6R_{500}$, refer to section 3). On the right panels, the dashed line represents the massive overlapping population without the BCGs of the neighbouring clusters. Errors are derived in A.2.

In figure 5.20 I show the AGN fraction as a function of r in extended *massive cluster* regions. The profiles look qualitatively similar to figure 5.18. In massive clusters, the features due to geometric overlaps are less pronounced than in low-mass clusters. In the profile of massive galaxies at low redshift (upper right panel), the peaks of remote and overlapping populations coincide, resulting in a much faster rise to the background value than seen in figure 5.18. At high redshift (bottom right panel), the profiles of the remote regions and of the overlapping regions are almost indistinguishable.

5.6 Radial Profiles in Other Studies

In figure 5.21, a fraction of cluster galaxies, hosting an X-ray bright AGN as a function of *projected* r is shown for all galaxies with $\log M_*(M_\odot) > 10.15$ and only massive galaxies with $\log M_*(M_\odot) > 11$, normalized to the background value. The results are compared with several observational studies. Since the studies used different redshift ranges, cluster mass ranges, and galaxy and AGN selection criteria (summarized in Table 5.1), the comparison should be done cautiously and should focus on general trends rather than on the exact values. Large errors in observations further prevent any definite conclusions. It is also unclear which profiles should be compared with the observational data. By doing an order of magnitude estimate, it can be seen that many studies in table 5.1 use stellar mass limit

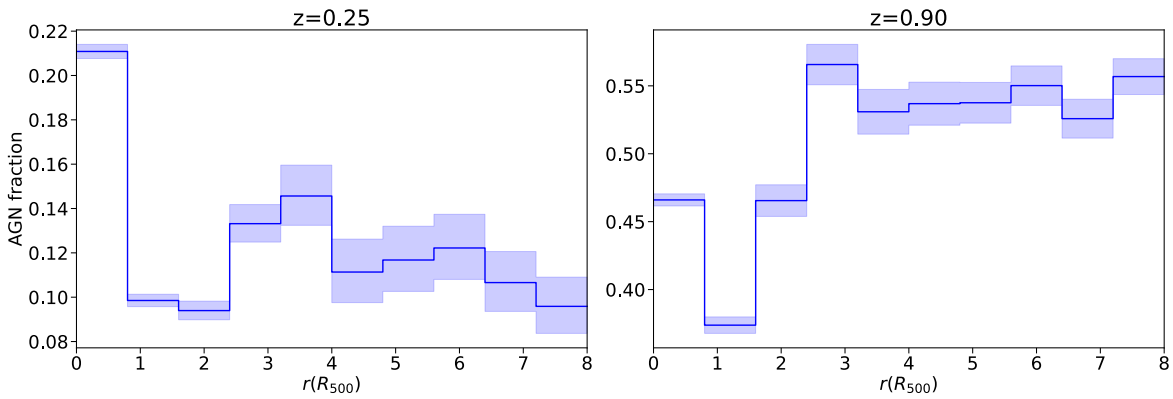

Figure 5.19: Fraction of massive *isolated* galaxies in remote regions (galaxies that are far away from any massive neighbouring clusters and do not belong to groups with several galaxies) hosting an X-ray bright AGN as a function of clustercentric distance r. The fraction is shown at low redshift (left panel) and at high redshift (right panel).

close to $10^{10} M_{\odot}$, which corresponds to the low-mass galaxies in this work. However, we know that the behaviour around the black hole seeding stellar mass in our simulations is somewhat unrealistic and that more massive galaxies are better resolved and more reliable. Thus some of the features found in massive galaxies might also appear in low-mass galaxies to a greater extent if the resolution was higher. Furthermore, stellar masses of massive galaxies in Magneticum appear to be overestimated, probably due to the AGN feedback implementation (Hirschmann et al. 2014), which means that massive galaxies in this work may be more suitable for comparison with low-mass galaxies in observations, than it may seem at first glance.

Almost all studies in figure 5.21 report a significant decrease in AGN activity in the inner cluster regions (Koulouridis et al. 2018, Ehlert et al. 2014, Haines et al. 2012, Koulouridis & Plionis 2010, Martini et al. 2007), which is also found in the profiles in our simulations, proving that the AGN suppression inside the cluster environment, thoroughly discussed throughout this chapter, is realistically described. As for other features, we have seen in previous sections that they are pronounced only in certain populations of galaxies and are barely visible in the combined profiles. Furthermore, projecting the galaxies and thus summing the contributions of different radial shells further blurs any features. The following comparison will thus refer to the trends noticed in the previous sections and not to the profiles in figure 5.21. In the profile from Ehlert et al. (2014), we can see a slight increase of the AGN fraction (although it is not statistically significant) in the inner regions, below $0.5 R_{500}$, which may reflect the increase found in figure 5.8, and was attributed to the increased local density and increasing black hole masses. The profile of *low-mass clusters* from Koulouridis et al. (2018) (where the galaxy magnitude selection criteria, roughly corresponding to our low-mass galaxies, are used) shows an absence of strong central decline and an excess of AGN activity between 1 and $2 R_{500}$. This could be in rough agreement with the profiles of low-mass galaxies in low-mass clusters found in the simulations (see figure 5.10), where the central decline is shallower compared to massive clusters. Although no excess is found between

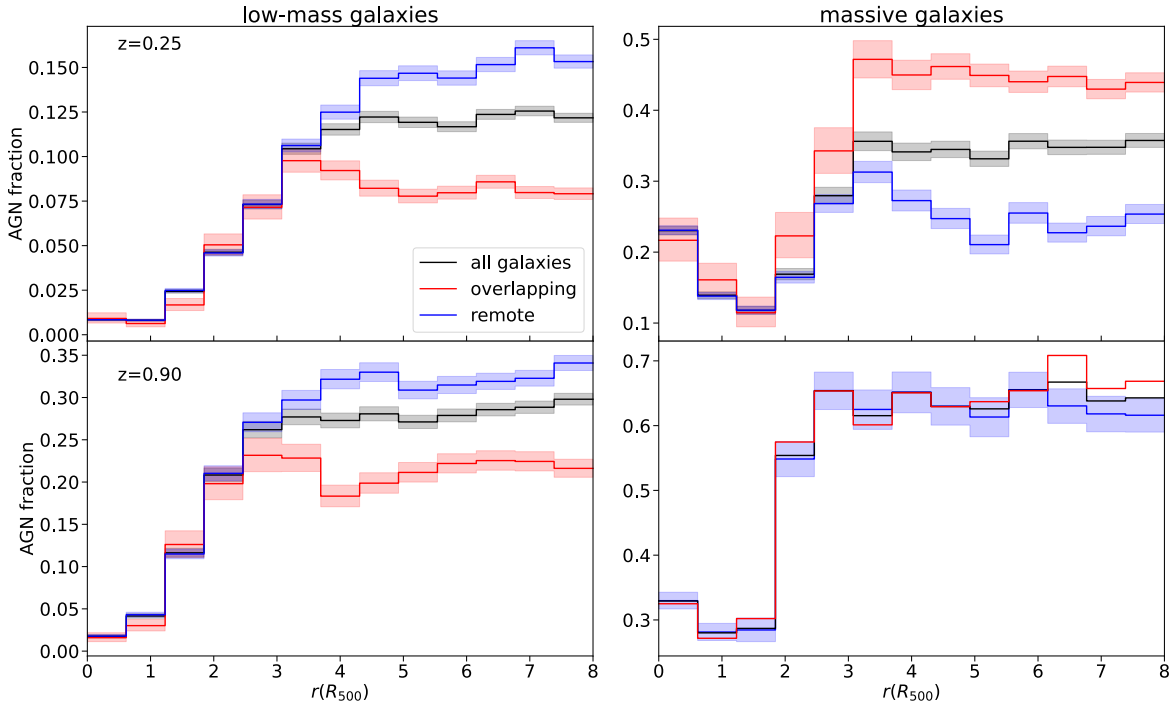

Figure 5.20: Fraction of galaxies hosting an X-ray bright AGN as a function of clustercentric distance r in *massive clusters* ($M_{500} > 10^{14} M_{\odot}$) for low-mass and massive galaxies at low and high redshift. The rofiles are shown separately for the remote and overlapping regions. For clarity, the errorbars on the bottom right panel are only shown for the isolated regions.

1 and $2R_{500}$, there is a plateau of AGN activity (which could be interpreted as an excess *with respect to the overall decline*), that is less apparent in massive clusters. Particularly interesting are the results of Koulouridis & Bartalucci (2019), featuring a clear excess of AGN activity on the outskirts of massive clusters at high redshift, between 2 and $3R_{500}$ (for more details and for the original profile, see Appendix C). This excess may be related to what I find in the profile of massive galaxies at high redshift in figure 5.18, where the peaks of the profile in remote regions (due to the environmental conditions) and in the overlapping regions (due to geometric overlaps) coincide and produce a noticeable excess in the combined profile around the same r. Note that the profile of galaxies used in Koulouridis & Bartalucci (2019) corresponds to our low-mass galaxies, so the direct comparison may not be meaningful. But even the profile of low-mass galaxies in figure 5.18 shows signs of excess around $3R_{500}$, primarily due to geometric overlaps. If studied further, our simulations may be able to provide further insight into the behaviour on the cluster outskirts, reported in Koulouridis & Bartalucci (2019).

5.7 AGN Luminosity

I also checked whether the observed profiles depend on the X-ray luminosity threshold used for the AGN selection (10^{42}ergs^{-1} in 0.5-10 keV band). In figure 5.22 I show the AGN fraction as a function of r, using different X-ray luminosity thresholds. The shape of the profiles of low-mass galaxies does not depend on the X-ray luminosity. Massive galaxies,

Study	z range	$M_{500}(M_\odot)$	AGN X-ray selection	galaxy selection
Koulouridis 2019	0.93-1.13	$5 \cdot 10^{14}$– $9 \cdot 10^{14}$	$L_X(0.5-8\text{keV}) >$ 3×10^{42} erg s $^{-1}$	$R < 23$, SuprimeCam R-band, $M_* \gtrsim 10^{10} M_\odot$
Koulouridis 2018	0.1-0.5	10^{13}– $5 \cdot 10^{14}$	$L_X(0.5-10\text{keV}) >$ 10^{42} erg s $^{-1}$	$-23.75 \lesssim M_i^* \lesssim -20.75$
Ehlert 2014	0.2-0.7	$4.7 \cdot 10^{14}$– $2.2 \cdot 10^{15}$	$F_X(0.5-8.0\text{keV}) >$ 10^{-14} erg cm^{-2} s^{-1}	$R < 23$, SuprimeCam R-band, $M_* \gtrsim 10^{10} M_\odot$
Haines 2012	0.15-0.3	$\gtrsim 5 \cdot 10^{14}$	$L_X(0.3-7\text{keV}) \gtrsim$ 10^{42} erg s $^{-1}$	$M_k < -23.1$
Koulouridis 2010	0.07-0.28		$L_X(0.5-8\text{keV}) >$ 10^{42} erg s $^{-1}$	$m_r^* - 0.5 < m_r < m_r^* + 0.5$
Martini 2007	0.06-0.31		$L_X > 10^{42}$erg s $^{-1}$ and $L_X > 10^{41}$erg s $^{-1}$	$M_R < -20$

Table 5.1: Redshift range, cluster mass range, AGN luminosity L_X (or flux F_X) of the AGNs, and magnitudes of optically selected galaxies from different studies, shown in figure 5.21. Refer to original papers and references therein for descriptions of the magnitude thresholds R, M_i^*, M_k and m_r, and details about the selected clusters where their mass was not given explicitly.

on the other hand, show slight variations. It seems that very bright AGNs (with luminosity above 10^{43}ergs^{-1}) prefer inner cluster regions. The minimum of the profile shifts to higher r, and the central rise of AGN activity begins already at around $2R_{500}$. This difference may have something to do with the different mass distribution of galaxies with different masses, but this investigation is beyond the scope of this work. In some studies (e.g., Martini et al. 2007), observational evidence is provided that brighter AGNs are distributed more centrally in galaxy clusters.

In figure 5.23 I show the median AGN bolometric luminosity of black holes hosted in low-mass and massive galaxies, as a function of the local density d_n, in the inner cluster regions (right panel) and on the outskirts (left panel). We can make some interesting observations when comparing the luminosity to the median black hole mass (figure 5.12). In low-mass galaxies, the expected AGN luminosity *increases* drastically with d_n in spite of smaller black hole masses $M_\bullet$. This may be because in undisturbed galaxies, far away from their neighbours, accreting gas may have a lower velocity relative to the black hole, which means a higher mass accretion rate from the Bondi model (equation (2.1)). In massive galaxies, on the other hand, black hole mass again becomes the dominant factor, and the AGN luminosity scales accordingly.

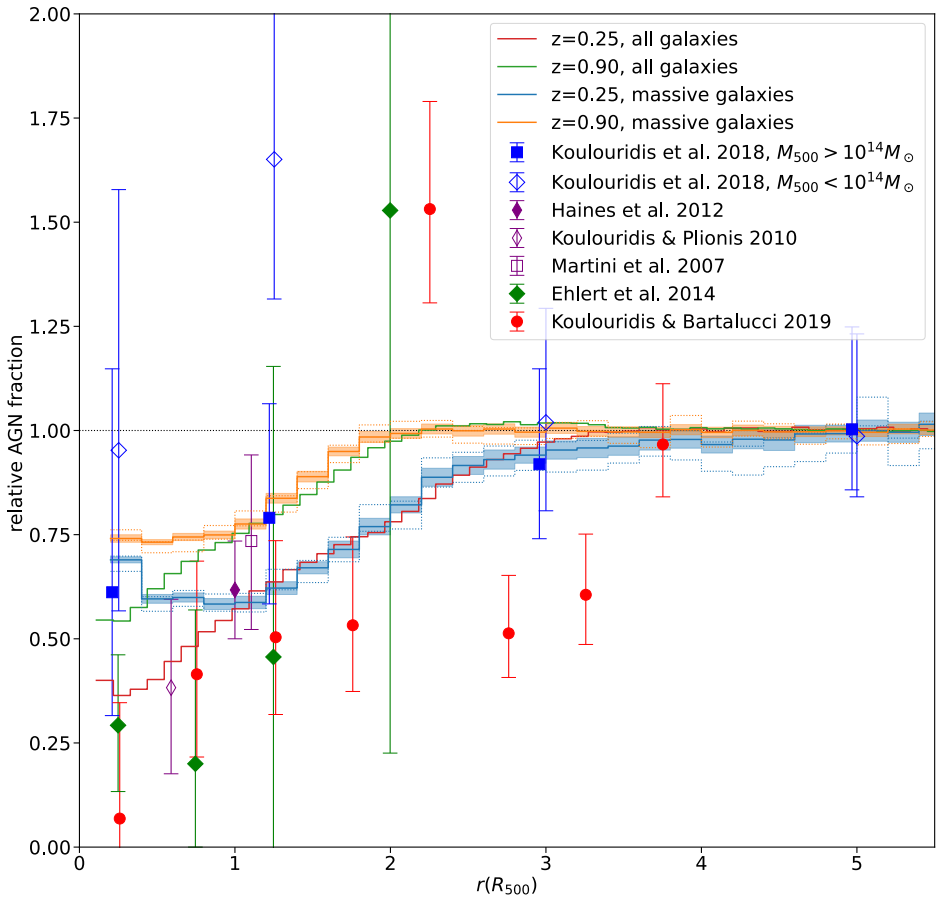

Figure 5.21: Fraction of galaxies containing an X-ray bright AGN, divided with the background fraction, as a function of *projected* clustercentric distance r. Magneticum results are shown at low and high redshift, using all clusters with $M_{500} > 10^{13} M_\odot$ and using all galaxies with $\log M_*(M_\odot) > 10.15$ and only massive galaxies. Projection depth is 7.6 Mpc (see section 5.1). The plot represents the mean profile of many lines of sight and the coloured interval ± standard deviation of different lines of sight. Dotted lines mark the 68% binomial confidence interval when only one LOS is considered. The central-most bin, influenced by the BCGs, is omitted. Confidence intervals are only displayed for massive galaxies. For the background calculation, see section 5.1. Results are compared with those of Koulouridis et al. (2018), from where I also obtained the measurements of Martini et al. (2007), Koulouridis & Plionis (2010) and Haines et al. (2012). I added the measurements of Ehlert et al. (2014) and Koulouridis & Bartalucci (2019). The redshifts, cluster masses and selection parameters of those studies are summarized in table 5.1. The data from Koulouridis & Bartalucci (2019) had to be manipulated (see Appendix C) to be comparable and should be taken with a grain of salt. For original measurements, see figure C.1. The data points are placed at the centre of radial bins. For clarity, I do not display the radial errorbars (bin sizes).

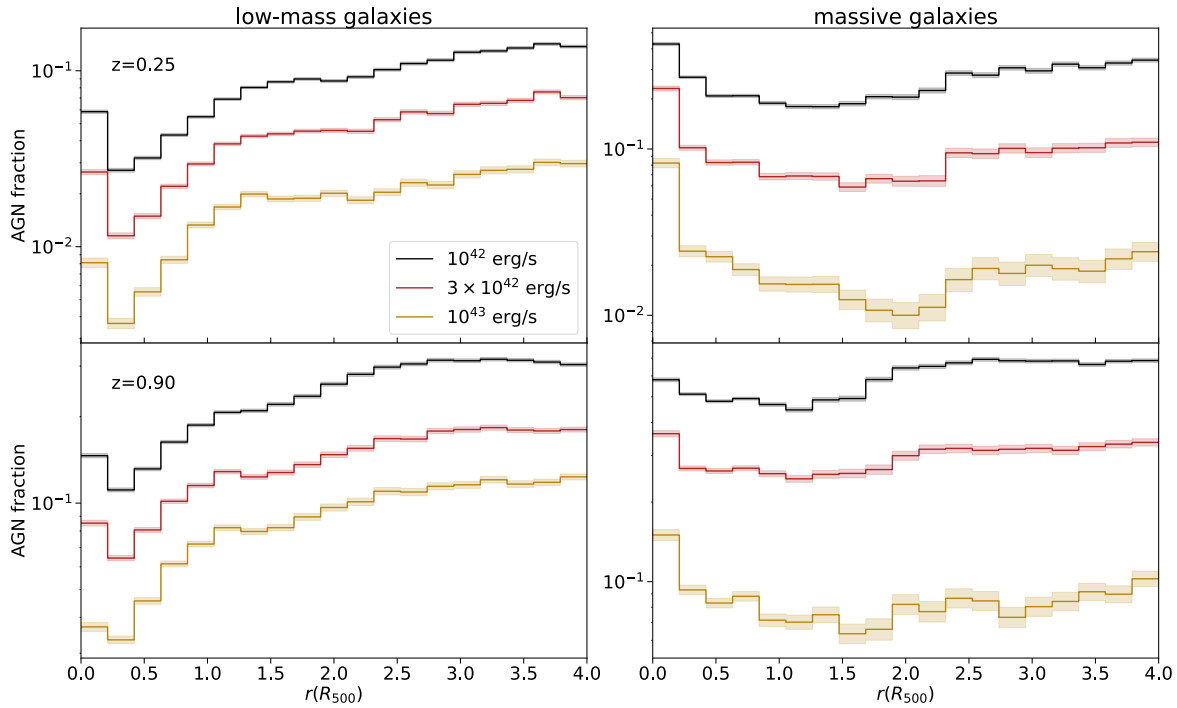

Figure 5.22: Fraction of galaxies hosting an X-ray bright AGN as a function of clustercentric distance r, if different AGN luminosity thresholds are used (luminosities are given in 0.5-10 keV band, derived in section 2.4). Results are shown for low-mass galaxies (left panels) and massive galaxies (right panels) at low and high redshift (upper and lower panels, respectively). The BCGs are excluded.

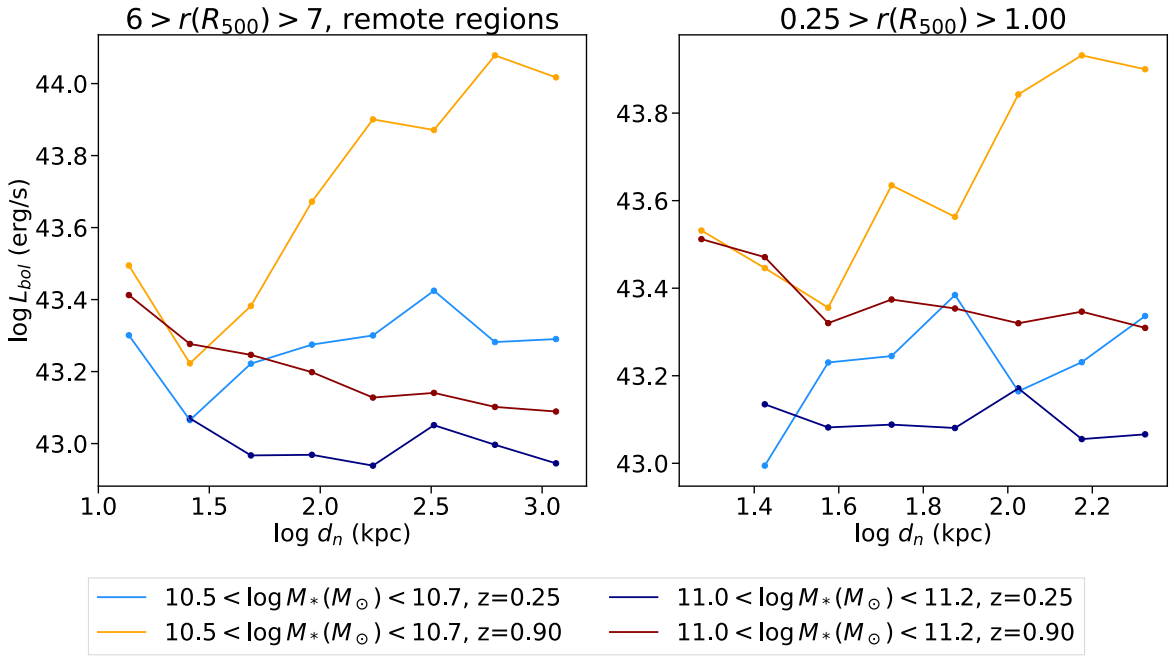

Figure 5.23: Median AGN bolometric luminosity (of AGNs with $L_X > 10^{42}$ergs^{-1} in 0.5-10 keV band), hosted by galaxies in two narrow stellar mass M_* ranges as a function of the distance to the nearest neighbour d_n. Data points are placed at the centres of bins in which the median luminosity was computed. I do not show the bins containing less than 10 AGNs. Results are shown for the field galaxies (left panel) and for the inner cluster regions (right panel) at low and high redshift. The figure can be compared with AGN fraction as a function of d_n shown in figure 5.11, and with the median black hole mass as a function of d_n, shown in figure 5.12.

Chapter 6

Conclusion

In this work I investigated the properties of cluster galaxies in *box2b* of the Magneticum suite of cosmological hydrodynamical simulations.

I investigated the distribution of cluster galaxies by fitting the NFW profile to their number density and concluded that low-mass galaxies are more concentrated at high redshift. The drastic change in the concentration found in the profile of galaxies is not found in dark matter profiles, indicating that galaxies may not be reliable tracers of dark matter. This work demonstrates that the NFW profile is not very suitable for describing the distribution of galaxies. Massive galaxies in particular clearly deviate from the NFW profile and the distribution of low-mass galaxies, displaying a relative overdensity around $r = 0.5R_{500}$.

I analysed the fraction of galaxies hosting an X-ray bright AGN in different populations of galaxies. Since AGN activity is fueled by the same cold gas reservoir as star formation, I focused on the comparison between the fraction of galaxies hosting an AGN and the ratio between the number of star-forming and quiescent galaxies. In *low-mass* galaxies, a drastic suppression of AGN activity and star formation in the cluster environment towards the cluster centre is found. This decline probably reflects the processes in the cluster atmosphere, depleting the cold gas reservoir. The exact mechanisms reducing star formation and AGN activity may differ; the galaxies in smaller groups, embedded in the cluster environment, show a significantly delayed central quenching compared to isolated galaxies, while the impact of the substructure and the local group environment on AGN activity is less evident. That could indicate the importance of the group atmosphere in shielding star formation from the effects of the ICM, while demonstrating that the inner regions are generally less suitable for AGN activity. The profiles of the star-forming ratio and AGN fraction in low-mass galaxies both level out around $2R_{500}$ before dropping again at small r, which may indicate the infalling population having the AGN activity and star formation triggered by ram pressure.

Massive galaxies ($M_* > 10^{11} M_\odot$) show an excess of star formation and AGN activity on the outskirts of clusters, which is also found in observations in Koulouridis & Bartalucci (2019) and is in line with the hypothesis that the cluster outskirts are a particularly suitable

environment for galaxy interactions and mergers due to lower velocity dispersion. In the inner cluster regions, the AGN profile departs from the profile of the star-forming ratio. While the AGN fraction displays a gradual decrease down to R_{500}, regardless of the star formation rate or substructure membership of the host galaxies, the star-forming ratio shows a secondary excess around R_{500}, caused mainly by the galaxies contained in the infalling groups. This peak is more pronounced than the excess on the outskirts and may be caused by the gas compression in massive mass-quenched galaxies during their infall. In the innermost regions, below $0.5R_{500}$, the AGN fraction of all galaxies increases due to higher median black hole masses in the cluster centre. This may be a consequence of different co-evolution of stellar and black hole masses of central galaxies or the tidal stripping in a very dense environment. Broadly speaking, I found that in low-mass galaxies, AGN fraction is more susceptible to global environmental influences, while in massive galaxies, local density and black hole mass play a dominant role.

I also investigated the direct effects of the local density, defined with the distance to the nearest neighbouring galaxy and found that the star-forming ratio and AGN fraction increase in locally dense environments. The increasing black hole masses in a denser environment contribute to this trend but are probably not the only cause. Low-mass galaxies are most likely to be star-forming in isolation, far from any clusters, which illustrates the impact of the environmental quenching in denser environments. On the other hand, the probability of hosting a bright AGN is the highest in the locally densest environment, perhaps indicating the importance of galaxy interactions. Interestingly, the AGNs in low-mass galaxies still tend to be brighter in isolation, which may be a consequence of smaller velocities of the accreting gas relative to the black hole. Massive galaxies are significantly more likely to host an AGN or form stars if they are in a locally denser environment. The absence of star formation in secluded massive galaxies shows the importance of mass quenching.

This work also demonstrates that the large-scale surroundings of clusters need to be carefully considered. The clusters tend to be located in dense environments, surrounded by other groups and clusters, which can affect the radial profile with their central suppression of AGN activity and star formation. The radial profiles of AGN activity and star formation of the overlapping cluster regions can combine into a profile, which appears to have an excess on the cluster outskirts, but this excess can be explained with geometric overlaps and does not require additional physical effects. In order to prove that the AGN activity is indeed elevated on the cluster outskirts with respect to the field value, I separately investigated the radial profile of regions far from any neighbouring massive groups. I also demonstrated that at low redshift, the geometric overlaps with other groups may prevent us from identifying the excess on the outskirts.

This work points out several interesting trends, found in Magneticum simulations, but hardly provides conclusive explanations, hence it is meant to encourage further exploration

of the topic. One of the major shortcomings is that it does not consider the kinematics of galaxies. Separating the infalling population from other satellites may provide additional insight into the processes governing star formation and AGN activity.

Appendix A

Errors

Despite using a relatively large cosmological box, the samples of galaxies and bright AGNs used in this work are often scarce. On the other hand, some of the radial features and trends reported in Chapters 4 and 5 are barely discernible. In order to determine their significance, it is crucial to estimate the deviations due to statistical noise. The derivations in the following sections were inspired by Gehrels (1986) and Park et al. (2006).

A.1 Ratio of Poisson variables

In Chapter 4, the ratio between the number star-forming galaxies (N_1) and quiescent galaxies (N_2) is investigated in different populations of galaxies. While the ratio N_1/N_2 can be instructive if the counts are high, the quantity that we are truly interested in, is the ratio of the *expected* N_1 and N_2:

$$\mathcal{R} \equiv \frac{\lambda_1}{\lambda_2}, \tag{A.1}$$

where λ_i is the expected number of galaxies N_i. The probability for measuring some N_i is given by the Poisson distribution:

$$P\left(N_i|\lambda_i\right) = \frac{\lambda_i^{N_i} e^{-\lambda_i}}{N_i!}. \tag{A.2}$$

We can briefly motivate this by considering the galaxies selected from a small volume in parameter space (r, M_*, d_n ...), so that their properties and the properties of the environment are approximately constant in that volume. Now imagine dividing this volume into infinitesimally small sub-volumes, each having the same properties and thus the same small probability of containing a galaxy. If this probability is independent of the contents of other volumes[1], the number of galaxies N_i follows Poisson statistics. This reasoning can be generalized to larger volumes in parameter space, covering regions with different properties, since the sum of independent Poisson variables is also a Poisson variable (Haight 1967). In the following

[1]Not necessarily the case, but in this work, where even narrow radial shells cover a large volume, it is a good approximation.

derivation it is assumed that the count N_1 *is independent of* N_2. If this is not true, see section A.2. The main goal of this section is to obtain the posterior probability density distribution of the ratio $\mathcal{R}$ (equation (A.1)). In other words, we want to use the measured counts N_1 and N_2 to infer what would be the ratio N_1/N_2 if a much larger cosmological volume with countless galaxies were available. Following the Bayes theorem and assuming the independence of both distributions, we can write the posterior probability for λ_1 and λ_2:

$$P\left(\lambda_1, \lambda_2 | N_1, N_2\right) \propto P\left(\lambda_1\right) P\left(N_1 | \lambda_1\right) P\left(\lambda_2\right) P\left(N_2 | \lambda_2\right), \tag{A.3}$$

where $P\left(\lambda_1\right)$ and $P\left(\lambda_2\right)$ are the prior distributions of λ parameters. In order to obtain unbiased results, an uninformative prior is chosen, parameterized by ϕ:

$$P(\lambda_i) \propto \lambda_i^{\phi-1}, \tag{A.4}$$

where $\phi = 1$ yields uniform prior in linear scale and $\phi = 0$ uniform prior in logarithmic scale. To emphasise the impact of prior, I continue the derivation with an arbitrary ϕ parameter; however, throughout this work, I only use $\phi = 1$. In equation (A.3) the posterior of λ_1 and λ_2 is shown, however, we are interested in $\mathcal{R}$ distribution. The probability density can be converted:

$$\begin{aligned} P(\mathcal{R}, \lambda_2 | N_1, N_2) &\propto P\left(\mathcal{R}\lambda_2, \lambda_2 | N_1, N_2\right) \left|\frac{\partial\left(\lambda_1, \lambda_2\right)}{\partial(\mathcal{R}, \lambda_2)}\right| \\ &\propto P\left(\mathcal{R}\lambda_2, \lambda_2 | N_1, N_2\right) \lambda_2. \end{aligned}$$

We can then marginalize the posterior over λ_2 to obtain marginal $\mathcal{R}$ posterior distribution. Note that despite the fact that Poisson distribution is a discrete probability mass function, λ_i parameters are continuous, and so are the posterior distributions, which we can integrate:

$$\begin{aligned} P(\mathcal{R} | N_1, N_2) &\propto \int_0^\infty P(\mathcal{R}, \lambda_2 | N_1, N_2) \mathrm{d}\lambda_2 \\ &\propto \int_0^\infty P\left(\mathcal{R}\lambda_2\right) P\left(N_1 | \mathcal{R}\lambda_2\right) P\left(\lambda_2\right) P\left(N_2 | \lambda_2\right) \lambda_2 \mathrm{d}\lambda_2 \\ &\propto \int_0^\infty P\left(\mathcal{R}\lambda_2\right) P\left(\lambda_2\right) \left(\mathcal{R}\lambda_2\right)^{N_1} e^{-\mathcal{R}\lambda_2} \lambda_2^{N_2} e^{-\lambda_2} \lambda_2 \mathrm{d}\lambda_2. \end{aligned} \tag{A.5}$$

We can then plug in the prior (equation (A.4)). The integral can be calculated analytically and expressed with the gamma function.

$$\begin{aligned} P(\mathcal{R} | N_1, N_2) &\propto \mathcal{R}^{N_1+\phi-1} \int_0^\infty \lambda_2^{N_1+N_2+2\phi-1} e^{-(\mathcal{R}+1)\lambda_2} \mathrm{d}\lambda_2 \\ &\propto \Gamma(N_1 + N_2 + 2\phi) \frac{\mathcal{R}^{N_1+\phi-1}}{(\mathcal{R}+1)^{N_1+N_2+2\phi}} \end{aligned} \tag{A.6}$$

The gamma function is not a function of $\mathcal{R}$, hence we do not need to calculate it explicitly. The part with $\mathcal{R}$ dependence can be integrated and expressed with Gauss hypergeometric function

${}_2F_1(a, b; c; z)$ and gamma function, the values of which can be obtained from function tables allowing us to avoid numeric integration.

$$P(\mathcal{R}_a < \mathcal{R} < \mathcal{R}_b|N_1, N_2) \propto \int_{\mathcal{R}_a}^{\mathcal{R}_b} \frac{\mathcal{R}^{N_1+\phi-1}}{(\mathcal{R}+1)^{N_1+N_2+2\phi}} \mathrm{d}\mathcal{R} \tag{A.7}$$
$$\propto \frac{\Gamma(N_1+\phi)}{\Gamma(N_1+\phi+1)} \left(\mathcal{R}^{N_1+\phi}\, {}_2F_1(N1+\phi, N_1+N_2+2\phi; 1+N_1+\phi; -\mathcal{R})\right)_{R_a}^{R_b}.$$

Normalization constant is obtained with integration from 0 to ∞ and can be expressed with beta function.

$$P(0 < \mathcal{R} < \infty|N_1, N_2) \propto \int_0^{\infty} \frac{\mathcal{R}^{N_1+\phi-1}}{(\mathcal{R}+1)^{N_1+N_2+2\phi}} \mathrm{d}\mathcal{R} \tag{A.8}$$
$$\propto B(N_2+\phi, 1-N_1-N_2-2\phi).$$

The results were verified with numeric integration. Equations (A.7) and (A.8) are very useful for quick calculations of confidence intervals if the numbers N_1 and N_2 are small. However, the values of hyper-geometric functions and the beta function become very small if N_1 and N_2 become large, making it hard to calculate values where N_1 and N_2 become of the order 100 (note that they are functions of the sum of N_1 and N_2). We can avoid calculations with small numbers if we rescale the integrand and then numerically integrate. The maximum of the posterior distribution (equation (A.6)) can be calculated:

$$\mathcal{R}_{max} = \frac{N_1+\phi-1}{N_2+\phi+1}. \tag{A.9}$$

We can immediately see that for a large number of objects, $\mathcal{R}_{max}$ goes to N_1/N_2, however for small numbers, simply calculating the ratio of counts would yield a biased estimate of the posterior mode. The prior choice (ϕ) also becomes increasingly important with a smaller count.

It is useful to derive the Gaussian approximation of the posterior (equation (A.6)). We express the posterior with the exponent of the logarithm and then expand the logarithms into the Maclaurin series around $\mathcal{R}_{max}$. For convenience, we define $\beta \equiv (\mathcal{R} - \mathcal{R}_{max})/\mathcal{R}_{max}$. We want to find the approximation for small β, which describes the probability density function where the peak is narrow and sufficiently far from $\mathcal{R} = 0$; note that for this condition, all N_1, N_2 and N_1/N_2 need to be large.

$$P(\mathcal{R}|N_1, N_2) \propto \exp\left((N_1+\phi-1)\ln\mathcal{R} - (N_1+N_2+2\phi)\ln(\mathcal{R}+1)\right) \tag{A.10}$$
$$\propto \exp\left((N_1+\phi-1)\ln(\beta+1) - (N_1+N_2+2\phi)\ln\left(\frac{\mathcal{R}_{max}}{\mathcal{R}_{max}+1}\beta+1\right)\right)$$
$$\propto \exp\left((N_1+\phi-1)\ln\left(\beta - \frac{\beta^2}{2} + \frac{\beta^3}{3} + O(\beta^4)\right) -\right.$$

$$(N_1 + N_2 + 2\phi) \ln\left(\frac{\mathcal{R}_{max}}{\mathcal{R}_{max}+1}\beta - \left(\frac{\mathcal{R}_{max}}{\mathcal{R}_{max}+1}\right)^2 \frac{\beta^2}{2} + \left(\frac{\mathcal{R}_{max}}{\mathcal{R}_{max}+1}\right)^3 \frac{\beta^3}{3} + O(\beta^4)\right).$$

Maclaurin series used for expansion converges if $|\beta| < 1$. After plugging in the expression for $\mathcal{R}_{max}$ (equation (A.9)), the linear β term in the exponent cancels out, and we are left with the second order approximation:

$$P(\mathcal{R}|N_1, N_2) \propto \exp\left(-\frac{(N_1 + \phi - 1)(N_2 + \phi + 1)}{N_1 + N_2 + 2\phi}\frac{\beta^2}{2} + O(\beta^3)\right). \tag{A.11}$$

It can be shown that the coefficient in the third order term is of a similar order of magnitude to the coefficient of the second order term for most N_1, N_2; the ratio between the second order and third order coefficient goes with $\sim \frac{N_1+N_2}{N_2+2N_1}$, hence the Gaussian approximation is only valid for small β. The posterior starts resembling a Gaussian pdf where its value falls off while still in the small β regime - this is true where $\sigma/\mathcal{R}_{max} \ll 1$, where σ is defined:

$$P(\mathcal{R}|N_1, N_2) \propto \exp\left(-\frac{(\mathcal{R} - \mathcal{R}_{max})^2}{2\sigma^2} + O\left((\mathcal{R} - \mathcal{R}_{max})^3\right)\right). \tag{A.12}$$

From equation (A.11), we can see that σ is much larger than $\mathcal{R}_{max}$ only if $N_1 \gg 1$ and $N_2 \gg 1$. In the limit of large counts, we can simplify further:

$$\sigma \approx \frac{N_1}{N_2}\sqrt{\frac{1}{N_1} + \frac{1}{N_2}}. \tag{A.13}$$

This expression for σ can also be obtained if we assume the Gaussian limit for both Poisson distributions $P(N_1|\lambda_1)$ and $P(N_2|\lambda_2)$, where σ goes to $\sqrt{N_1}$ and $\sqrt{N_2}$ respectively, and then calculate the ratio of random variables N_1 and N_2 with Gaussian error propagation. In the limit of large numbers, equation (A.9) simplifies to $\mathcal{R}_{max} \approx N_1/N_2$.

The Poisson posterior probability density function (equation (A.6)) for 3 different pairs of N_1 and N_2 is plotted in figure A.1. We can see that although all three pairs have the same ratio N_1/N_2, the expected ratio $\mathcal{R}$ is different, depending on the count. For example, if we consider a small population of galaxies with $N_1 = 1$ and $N_2 = 2$, that means that in a larger cosmological box (and larger population of galaxies with the same properties), the ratio N_1/N_2 would most likely be around 0.2 and not 0.5, as we might naively expect from N_1/N_2 of the smaller sample. This rather unintuitive behaviour can be verified with a simple test. I generated a large uniformly distributed set of pairs (λ_1, λ_2) and with each pair generated N_1 and N_2, according to the Poisson distribution (equation (A.2)). I checked that the distribution of the ratios $\mathcal{R}$ of those pairs (λ_1, λ_2) that yielded some N_1 and N_2, agreed with equation (A.6).

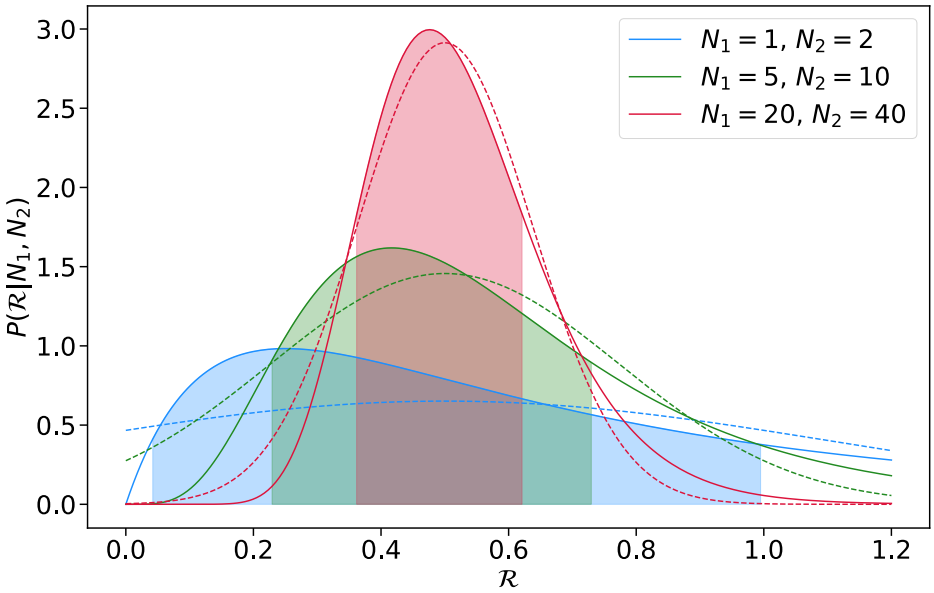

Figure A.1: Posterior probability density function of the ratio of Poisson probabilities $\mathcal{R}$ (equation (A.6)), shown for three pairs of N_1 and N_2. Shaded areas represent the 68% highest posterior density interval. Dashed lines represent the Gaussian approximations (equation A.11).

A.2 Binomial Distribution

The key assumption in section A.1 was, that N_1 and N_2 are independent, each following Poisson distribution with parameters λ_1 and λ_2 respectively. However, this may not be a good assumption in some cases. In chapter 5 I investigate the fraction of galaxies hosting an X-ray bright AGN. The number of AGNs/AGN hosts (N_1) is not independent of the total number of galaxies N_2. Instead, we can assume that each galaxy hosts an AGN with probability $\mathcal{P}$. The number of AGNs N_1 thus depends on N_2, following binomial distribution:

$$P(N_1|N_2, \mathcal{P}) = \binom{N_2}{N_1} \mathcal{P}^{N_1} (1-\mathcal{P})^{N_2-N_1} . \tag{A.14}$$

The quantity of interest (referred to as the fraction of galaxies hosting an AGN in Chapter 5) is the probability $\mathcal{P}$, which we want to infer from the measured N_1 and N_2. Similarly to equation (A.4), the prior is parameterized with ϕ:

$$P(\mathcal{P}) \propto \mathcal{P}^{\phi-1}, \tag{A.15}$$

and the posterior probability density of the $\mathcal{P}$ parameter can be expressed:

$$\begin{aligned} P(\mathcal{P}|N_1, N_2) &\propto P(\mathcal{P}) P(N_1|N_2, \mathcal{P}) \\ &\propto \mathcal{P}^{\phi+N_1-1} (1-\mathcal{P})^{N_2-N_1}. \end{aligned} \tag{A.16}$$

Unlike the Poisson ratio $\mathcal{R}$ (equation (A.6)), probability $\mathcal{P}$ is restricted to [0,1] interval. Despite not writing it explicitly, binomial coefficient $\binom{N_2}{N_1}$ requires that $N_1 \leq N_2$; each galaxy

can only host a single AGN. The mode of the posterior probability is at

$$\mathcal{P}_{max} = \frac{N_1 + \phi - 1}{N_2 + \phi - 1}. \tag{A.17}$$

If a uniform prior is chosen ($\phi = 1$), the count ratio N_1/N_2 gives a precise value of $\mathcal{P}_{max}$, even for small counts N_1, N_2, in contrast to the mode of the Poisson ratio (equation (A.9)). If we want to determine the confidence intervals of the posterior, it is useful to calculate the integrated probability. The integral between two arbitrary values $\mathcal{P}_1$ and $\mathcal{P}_2$ can be expressed with the incomplete beta function

$$\begin{aligned} P(\mathcal{P}_1 < \mathcal{P} < \mathcal{P}_1 | N_1, N_2) &\propto \int_{\mathcal{P}_1}^{\mathcal{P}_2} \mathcal{P}^{\phi+N_1-1}(1-\mathcal{P})^{N_2-N_1} \mathrm{d}\mathcal{P} \\ &\propto B(\mathcal{P}_1; N_1 + \phi, 1 - N_1 + N_2) - B(\mathcal{P}_2; N_1 + \phi, 1 - N_1 + N_2), \end{aligned} \tag{A.18}$$

and the normalization constant can be expressed with gamma function:

$$\begin{aligned} P(0 < \mathcal{P} < 1) &\propto \int_0^1 \mathcal{P}^{\phi+N_1-1}(1-\mathcal{P})^{N_2-N_1} \mathrm{d}\mathcal{P} \\ &\propto \frac{\Gamma(1 - N_1 + N_2)\Gamma(N_1 + \phi)}{\Gamma(N_2 + 1 + \phi)}. \end{aligned} \tag{A.19}$$

Both functions are available in libraries like *scipy*, which can speed up computations for small N_1, N_2, however for large counts, it becomes numerically more feasible to rescale the integrand and integrate numerically or to use approximations. As before, we try to find a Gaussian approximation of the posterior (equation (A.16)). We define $\beta \equiv (\mathcal{P} - \mathcal{P}_{max})/\mathcal{P}_{max}$ and use the Maclaurin series to approximate the logarithms in the vicinity of $\mathcal{P}_{max}$:

$$\begin{aligned} P(\mathcal{P}|N_1, N_2) &\propto \exp\left((N_1 + \phi - 1)\ln\mathcal{P} + (N_2 - N_1)\ln(1-\mathcal{P})\right) \\ &\propto \exp\left((N_1 + \phi - 1)\ln(\beta+1) + (N_2 - N_1)\ln\left(1 - \frac{\mathcal{P}_{max}}{1-\mathcal{P}_{max}}\beta\right)\right) \\ &\propto \exp\left((N_1 + \phi - 1)\ln\left(\beta - \frac{\beta^2}{2} + \frac{\beta^3}{3} + O(\beta^4)\right) + \right. \\ &\left. (N_2 - N_1)\ln\left(-\frac{\mathcal{P}_{max}}{1-\mathcal{P}_{max}}\beta - \left(\frac{\mathcal{P}_{max}}{1-\mathcal{P}_{max}}\right)^2\frac{\beta^2}{2} + \left(\frac{\mathcal{P}_{max}}{1-\mathcal{P}_{max}}\right)^3\frac{\beta^3}{3} + O(\beta^4)\right)\right). \end{aligned} \tag{A.20}$$

The expansion of the logarithms converges if $|\beta| < \frac{1-\mathcal{P}_{max}}{\mathcal{P}_{max}}$. After plugging in the expression for $\mathcal{P}_{max}$ (equation (A.17)), the linear β term in the exponent cancels out, and we are left with the second order approximation:

$$P(\mathcal{P}|N_1, N_2) \propto \exp\left(-\frac{(N_1 + \phi - 1)(N_2 + \phi - 1)}{N_2 - N_1}\frac{\beta^2}{2} + O(\beta^3)\right). \tag{A.21}$$

The approximation is useful if the posterior falls off to low values while still in low β regime: where $\sigma/\mathcal{R}_{max} \ll 1$ (σ is defined analogously to equation (A.12)). From equation (A.21), we can see that this means that $\frac{N_2-N_1}{N_1N_2} \ll 1$ (if neglecting $\phi - 1$). From this condition alone, the Gaussian approximation would also be valid for the low count if $N_1 \approx N_2$. However (as can be inferred from the condition for the Maclaurin series convergence), as N_1 and N_2 become similar, higher order terms in the exponent become increasingly important. Indeed, the ratio between the second order and third order coefficient scales (for large N_1 and N_2) with $(N_2(N_2 - N_1))/(2N_1^2 + N_2^2 - 2N_1N_2)$. To summarize, if $N_1 \gg 1$, $N_2 \gg 1$ and N_1 is sufficiently smaller than N_2, posterior can be approximated with a Gaussian with

$$\sigma \approx \frac{N_1}{N_2}\sqrt{\frac{1}{N_1} - \frac{1}{N_2}}, \tag{A.22}$$

which simplifies to $\sigma \approx \sqrt{N_1}/N_2$ if $N_1 \ll N_2$. This limit can also be obtained if considering that for $N_1 \ll N_2$, binomial likelihood $P(N_1|N_2, \mathcal{P})$ converges to Poisson likelihood with $\lambda = N_2\mathcal{P}$. If $N_1 \gg 1$, Poisson distribution can then be approximated with Gaussian with $\sigma = \sqrt{N_1}$, centered at N_1/N_2. Note that under those conditions, Poisson ratio $\mathcal{R}$ (section A.1) converges to the same Gaussian curve (equation (A.13)).

The errorbars and confidence intervals, shown in plots throughout this work, are the 68% *highest posterior density intervals*; they are the smallest intervals where the ratio $\mathcal{R}$ or the fraction $\mathcal{P}$ are found with 68% probability. It should also be pointed out that in some cases, it may not be entirely clear which of the two methods for calculating the errors to use. For example, if N_1 represents the number of AGNs, regardless of their host galaxies, and N_2 is the number of very massive galaxies, the binomial approach is not sufficient anymore since the number of AGNs can exceed the number of very bright galaxies. On the other hand, the assumptions of Poisson statistics are also not justified anymore - since many AGNs are hosted by very massive galaxies, N_1 is highly correlated with N_2. In such cases (and also in general, to reduce the influence of our choice of prior), the bin sizes should be large enough so that the conclusions do not rely on the exact width of confidence intervals.

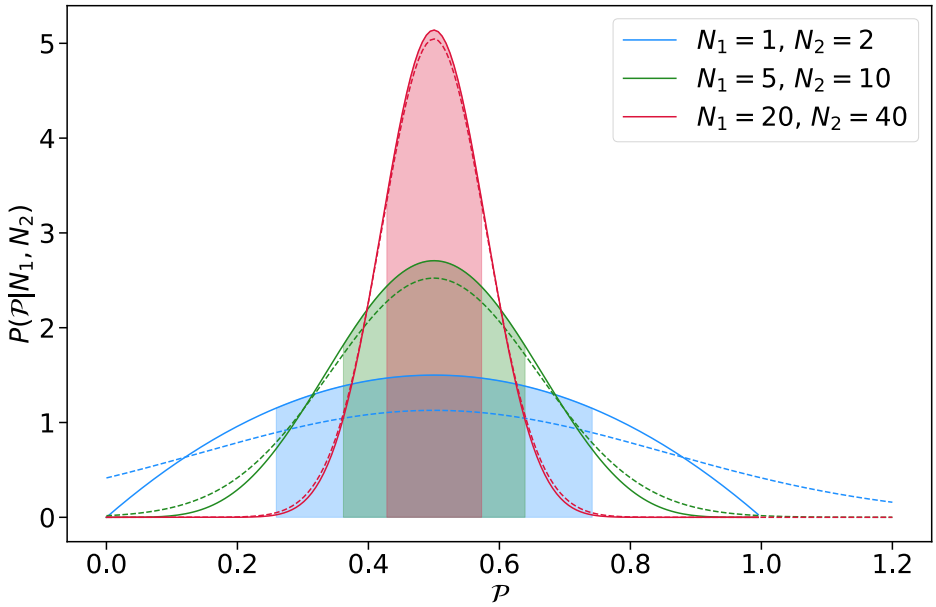

Figure A.2: Posterior probability density function of parameter $\mathcal{P}$ of the binomial distribution (equation (A.16)), plotted for three pairs of N_1 and N_2. Shaded areas represent the 68% highest posterior density interval. Dashed lines represent the Gaussian approximations (equation A.21).

Appendix B

Fitting the NFW Profile

B.1 Integrated Profile

In this section, I describe the procedure of fitting the NFW profile (equation (1.11)) to the distribution of galaxies in groups and clusters in Magneticum simulations. As a proof of concept, I will avoid making the assumption of large numbers and follow Poisson statistics.

The number density as a function of r in equation (1.11) is the probability density function which cannot be directly fitted to a finite discrete sample of galaxies (at least not without some crude assumptions). In order to compare it to the discrete sample, it needs to be integrated over some finite volume. Since I am interested in the radial dependence, I calculate the expected number of galaxies λ_i (notation is chosen for consistency with section A.1) in the spherical shell between the distance $\tilde{r}_{i-1/2}$ and $\tilde{r}_{i+1/2}$ from the center of the cluster:

$$\begin{aligned}
\lambda_i =& \int_{\tilde{r}_{i-1/2}}^{\tilde{r}_{i+1/2}} \frac{n_0}{\left(\tilde{r}/\tilde{r}_g\right)\left(1+\tilde{r}/\tilde{r}_g\right)^2} 4\pi\tilde{r}^2 \mathrm{d}\tilde{r} = \\
=& 4\pi n_0 \tilde{r}_g^3 \left(\frac{1}{1+\frac{\tilde{r}_{i+1/2}}{\tilde{r}_g}} - \frac{1}{1+\frac{\tilde{r}_{i-1/2}}{\tilde{r}_g}} + \ln\left(\frac{1+\frac{\tilde{r}_{i+1/2}}{\tilde{r}_g}}{1+\frac{\tilde{r}_{i-1/2}}{\tilde{r}_g}} \right) \right) = \\
=& 4\pi R_{500}^3 N_0 \underbrace{\left(\frac{1}{1+\frac{r_{i+1/2}}{r_g}} - \frac{1}{1+\frac{r_{i-1/2}}{r_g}} + \ln\left(\frac{1+\frac{r_{i+1/2}}{r_g}}{1+\frac{r_{i-1/2}}{r_g}} \right) \right)}_{\mathcal{N}_i},
\end{aligned} \tag{B.1}$$

where we remembered that $r/r_g = \tilde{r}/\tilde{r}_g$ (equation (1.8)), and where we define:

$$N_0 = n_0 r_g^3. \tag{B.2}$$

The integral was calculated with partial integration. If we assume that the scale radius $\tilde{r}_g$ scales with size of the cluster R_{500}, and thus that r_g is constant, $\mathcal{N}_i$ in equation (B.1) is independent of the size of the cluster R_{500}, i.e., the shape of the density profile looks identical

if rescaled to R_{500} of each cluster. For clusters A and B and radial shells i and j, we can write

$$\frac{\lambda_i^A}{\lambda_j^A} = \frac{\lambda_i^B}{\lambda_j^B} = \frac{N_i}{N_j}, \tag{B.3}$$

from which it follows that we can stack the relative shells of multiple clusters together and still obtain the same profile:

$$\frac{\lambda_i^A + \lambda_i^B}{\lambda_j^A + \lambda_j^B} = \frac{\lambda_i^A \left(1 + \frac{\lambda_i^B}{\lambda_i^A}\right)}{\lambda_j^A \left(1 + \frac{\lambda_j^B}{\lambda_j^A}\right)} = \frac{\lambda_i^A}{\lambda_j^A}. \tag{B.4}$$

In a single cluster, the parameter n_0 represents the fourfold number density at r_g, and is proportional to the mean number density of the shell N_i/V_i, where V_i is the volume of the shell, proportional to R_{500}^3 of the cluster. If we stack shells i of multiple clusters together, n_0 is proportional to the mean number density of all shells combined:

$$n_0 \propto \frac{\lambda_i^A + \lambda_i^B}{V_i^A + V_i^B}. \tag{B.5}$$

From equation (B.1) we can see that λ_i is proportional to $n_0 r_g^3$. In order to avoid large degeneracy of parameters, we use parameter N_0 as a free parameter (equation (B.2)), instead of n_0. We fit the parameters N_0 and r_g after stacking the shells (counts N_i) of many clusters and groups.

B.2 Fitting the Probability Density Function

With equation (B.1), I calculate the expected number of galaxies in the i-th shell λ_i, which I can then compare to the measured number of galaxies in the i-th shell N_i. The measured number of galaxies N_i is drawn from the Poisson distribution with expectation value λ_i:

$$P\left(N_i|\lambda_i\right) = \frac{\lambda_i^{N_i} e^{-\lambda_i}}{N_i!}. \tag{B.6}$$

For each bin we can then apply the Bayes theorem to calculate the posterior for λ_i.

$$P\left(\lambda_i|N_i\right) \propto P\left(N_i|\lambda_i\right) P\left(\lambda_i\right), \tag{B.7}$$

where we choose a uniform prior $P(\lambda_i) = const$ if $\lambda_i \geq 0$ and $P(\lambda_i) = 0$ for negative values of λ_i. We then assume that the measured number of galaxies N_i in the i-th bin is independent of the measured number in the j-th bin N_j. We can then write the logarithm of the posterior

probability for the profile $\{\lambda_i\}$ as a function of the measured set $\{N_i\}$ in all bins:

$$\ln P\left(\{\lambda_i\}|\{N_i\}\right) = const + \sum_i \left(N_i \ln \lambda_i - \lambda_i + \ln P\left(\lambda_i\right)\right), \tag{B.8}$$

where the profile $\{\lambda_i\}$ can be expressed with parameters r_g and N_0 with equation (B.1).

If we intended to use the Gaussian approximation of the Poisson statistics and the conventional least squares regression method, we would need to carefully choose the number of bins; the bins would need to be large enough to contain enough galaxies to justify the Gaussian approximation, while not being too large - by binning the data we lose some information about the exact position of the data points. If an even more crude approximation is made, and the number density $n(r)$ is fitted directly to the binned data (without integrating over bins), the bias can be even larger since $n(r)$ is expected to match the histogram bin values, only if the bins are small. By using Poisson statistics (and integrating over bins), such trade-off is avoided; equations above hold even for very low values of λ_i, so the number of bins can be (and should be) large. I verified that our procedure gives reliable results even in the limit of the very high number of bins, where we have only a few galaxies per bin and where many bins are empty - the case where Gaussian approximation fails completely.

B.3 Stacked Profiles

For fitting, I used the radial range between $0.05R_{500}$ and $2R_{500}$. I excluded the innermost regions since the BCGs produce a large excess in the innermost radial bin (especially in low-mass groups with fewer satellites), which can significantly deteriorate the fit. I used 2000 radial bins. For clarity, I use fewer bins for plotting (e.g., in figure B.2). For estimating the shape of the posterior distribution (equation (B.8)), MCMC could be in principle used; however, since I only need to evaluate two parameters, I resort to numerical integration.

In figure B.1, I show an example of the posterior distribution at low and high redshift. We can see that parameters N_0 and r_g are highly correlated (correlation is still much weaker than if n_0 is used instead of N_0). For each marginal posterior distribution I calculated the expectation values $\langle r_g \rangle$, $\langle N_0 \rangle$, standard deviations σ_{r_g}, σ_{N_0}, concentration c_{200}, which was obtained from $\langle r_g \rangle$ and equation (1.11), and the Pearson correlation coefficient, defined as

$$\rho_{r_g,N_0} = \frac{\sigma_{r_g N_0}}{\sigma_{r_g}\sigma_{N_0}}, \tag{B.9}$$

where $\sigma_{r_g N_0}$ is the covariance. The posterior distributions closely resemble Gaussian distributions. I verified that the 68.27% confidence interval corresponds to $\left[\langle r_g \rangle - \sigma_{r_g}, \langle r_g \rangle + \sigma_{r_g}\right]$ and $\left[\langle N_0 \rangle - \sigma_{N_0}, \langle N_0 \rangle + \sigma_{N_0}\right]$ and that the expectation values of marginal distributions corresponds to the maximum of the two dimensional posterior probability density.

In tables B.1 and B.2 the results of the regression at different redshifts and in different cluster and galaxy mass ranges are shown. Number density profiles and best models are shown in figure B.2. I also fitted the model only to the inner regions (up to R_{500}, table B.3). Standard deviations of both parameters are, however, very small; their meaning can be deceiving (discussed later in the chapter).

In figure B.2 we can see that the number density of low-mass and massive galaxies combined is described by the NFW profile much better than the number density of massive galaxies alone. The fact that massive galaxies are not the ideal tracers of the dark matter distribution is not surprising since they are likely to be located in the centres of subgroups (briefly shown in chapter 4).

In massive clusters I find c_{200} in the range between 3.5 and 5.9, which is similar to what is found in dark matter profiles of various simulations and observations (for an overview, see Ragagnin et al. 2019). We can also notice a general decrease of concentration with increasing halo mass, which is also in agreement with dark matter profiles in other simulations (Jing 2000, Bullock et al. 2001) and in Magneticum simulations (Ragagnin et al. 2019), however, the conclusion should be taken with a grain of salt, since the mass range I am using is narrow and the values not significantly different.

In terms of redshift evolution, however, results seem to be in tension with the literature (Bullock et al. 2001). Instead of an increase of concentration with time due to R_{200} growth, I find a significant decrease in concentration; this controversial redshift dependence is stronger than mass dependence. It seems that not only does the core radius $\tilde{r}_g$ increase with time, it increases faster than the scale of the cluster (defined with respect to the critical density). This redshift dependence differs from what is found in dark matter profiles (section B.5), and might be the reason why in chapters 4 and 5, the radial profiles at low redshift seem more extended compared to high redshift.

The fitting method described above has some noteworthy shortcomings. First, we should keep in mind that we define the core radius relative to R_{500} instead of R_{200} (and only then convert to c_{200} using obtained profile). The former is less susceptible to any accretion to the cluster outskirts, which could change the concentration defined with R_{200}. Furthermore, the stacked profile of all clusters may not give the best estimate of the individual cluster profiles. The clusters used here may have significantly different profiles (e.g., we have unrelaxed and merging halos) and the errors obtained with this method do not reflect the scatter of the parameters of individual clusters. The method above can be seen as a mere description of the combined profile - if we selected another sample of clusters that is statistically equivalent to the sample used here (e.g., containing clusters with the same properties but different discrete realisations of galaxy distribution), we would expect the parameters of the combined distribution to be in line with the posterior probability found here. In some papers, the cluster

z	$\log M_{500}(M_\odot)$	$\langle r_g \rangle\,[R_{500}]$	$\langle N_0 \rangle\,\left[(\mathrm{kpc}/h)^{-3}\right]$	σ_{r_g}	σ_{N_0}	ρ_{r_g,N_0}	c_{200}
0.25	[13,14]	3.87e-01	1.26e-08	1.9e-03	4.8e-11	0.90	3.96
	[14,15.3]	4.48e-01	1.23e-08	4.3e-03	9.7e-11	0.91	3.46
	[13,15.3]	3.99e-01	1.25e-08	1.7e-03	4.2e-11	0.90	3.86
0.90	[13,14]	2.99e-01	6.72e-09	1.9e-03	3.0e-11	0.88	5.06
	[14,14.7]	3.31e-01	5.95e-09	7.0e-03	9.4e-11	0.89	4.59
	[13,14.7]	3.01e-01	6.65e-09	1.8e-03	2.9e-11	0.88	5.02

Table B.1: Posterior expectation value, standard deviation, Pearson correlation coefficient and the concentration of the NFW parameters r_g and N_0. All galaxies between 0.05 and $2R_{500}$ with $\log M_*(M_\odot) > 10.15$ at low and high redshift and in low-mass and massive clusters were used. c_{200} is obtained from $\langle r_g \rangle$ and the NFW profile (equation (1.11)).

z	$\log M_{500}(M_\odot)$	$\langle r_g \rangle\,[R_{500}]$	$\langle N_0 \rangle\,\left[(\mathrm{kpc}/h)^{-3}\right]$	σ_{r_g}	σ_{N_0}	ρ_{r_g,N_0}	c_{200}
0.25	[13,14]	4.64e-01	1.47e-09	6.8e-03	1.8e-11	0.91	3.35
	[14,15.3]	3.90e-01	1.63e-09	9.6e-03	3.2e-11	0.90	3.94
	[13,15.3]	4.43e-01	1.50e-09	5.6e-03	1.6e-11	0.91	3.50
0.90	[13,14]	2.84e-01	9.15e-10	4.5e-03	1.0e-11	0.87	5.31
	[14,14.7]	2.56e-01	9.76e-10	1.2e-02	3.2e-11	0.86	5.85
	[13,14.7]	2.81e-01	9.20e-10	4.2e-03	9.9e-12	0.87	5.37

Table B.2: Analogous table to table B.1 for massive galaxies. Galaxies between 0.05 and $2R_{500}$ with $\log M_*(M_\odot) > 11$ at low and high redshift and in low-mass and massive clusters were used.

z	$\log M_{500}(M_\odot)$	$\langle r_g \rangle\,[R_{500}]$	$\langle N_0 \rangle\,\left[(\mathrm{kpc}/h)^{-3}\right]$	σ_{r_g}	σ_{N_0}	ρ_{r_g,N_0}	c_{200}
0.25	[13,14]	4.49e-01	1.46e-08	2.8e-03	9.6e-11	0.94	3.45
	[14,15.3]	5.54e-01	1.56e-08	7.0e-03	2.2e-10	0.95	2.84
	[13,15.3]	4.67e-01	1.47e-08	2.6e-03	8.8e-11	0.95	3.33
0.90	[13,14]	3.94e-01	8.87e-09	3.1e-03	7.0e-11	0.94	3.90
	[14,14.7]	4.49e-01	8.19e-09	1.2e-02	2.3e-10	0.94	3.46
	[13,14.7]	3.98e-01	8.80e-09	3.0e-03	6.7e-11	0.94	3.87

Table B.3: Analogous table to table B.1 for the inner cluster regions. Galaxies between 0.005 and $1R_{500}$ with $\log M_*(M_\odot) > 10.15$ at low and high redshift and in low-mass and massive clusters were used.

sample is further divided into relaxed and disturbed halos (e.g., see Klypin et al. 2016), in order to get a better estimate of the profile of individual clusters.

B.4 Individual Profiles

To get a better insight into how the individual profiles look like and what are the actual uncertainties of the parameters, I fitted the NFW profile (equation (1.11)) to the profiles of individual clusters (note that here, the high count assumption would not be justified anymore, and the full Poisson description from section B.2 is required). For each cluster, I obtained the r_g and N_0 in the maximum of posterior. The posterior distribution of a single cluster is

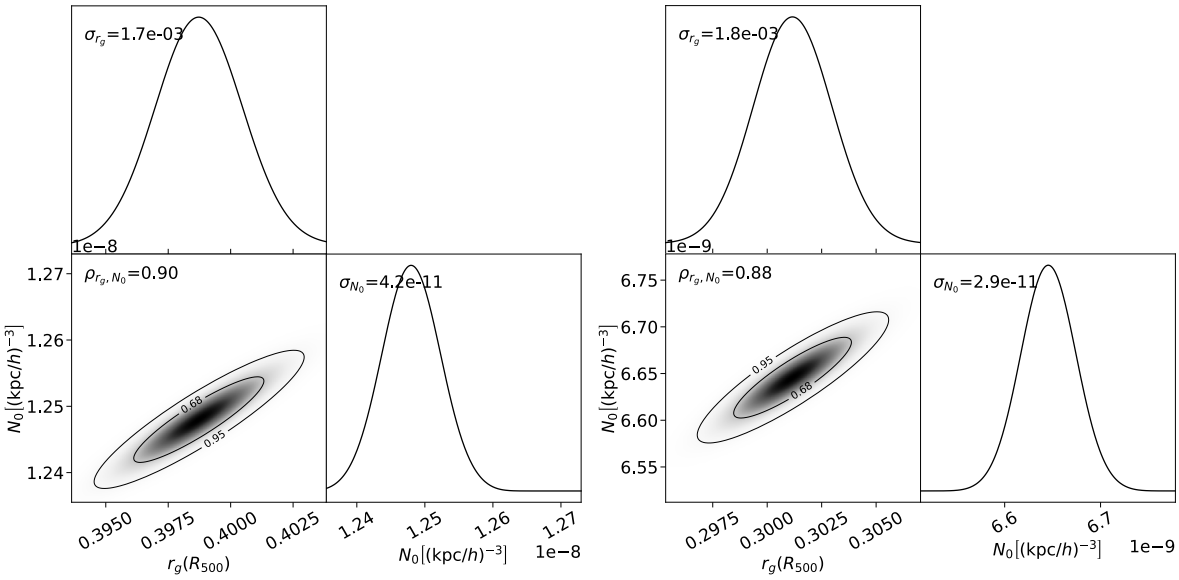

Figure B.1: Posterior probability densities for parameters N_0 and r_g at low redshift ($z = 0.25$) on the left panel, and high redshift ($z = 0.90$) on the right panel. All galaxies with $\log M_*(M_\odot) > 10.15$ and all groups with $\log M_{500}(M_\odot) > 13$ were used. I used 2000 radial bins between 0.05 and $2R_{500}$, and verified that using more bins did not alter the outcome.

plotted on the left panel of figure B.3 - the uncertainties of parameters in a single halo are very large due to only a handful of bright galaxies residing in a single cluster. Note that the posterior distributions are asymmetric and we discard much information by only taking the maximum of the posterior. But nonetheless, we can look at the distribution of the parameter values of individual clusters (right panel in figure B.3). In the scatter plot of figure B.3, we can notice that the clusters with low N_0 tend to have discrete r_g values, which I found to be a consequence of binning; if the number of bins is increased, the distribution gets smoother, which is a nice demonstration of why the number of bins should be kept high.

In table B.4, I calculated the median, standard deviation, covariance and concentration of the best fit parameters of individual halos (the sample of galaxies and clusters is the same as in table B.1). I excluded a small fraction of clusters, which yielded unreasonable parameter values and had especially large uncertainties of parameters. By comparing the tables B.4 and B.1, we can see that the median values do not differ drastically from the expectation values of the stacked profile; the general trends discussed in section B.3, remain the same. The agreement between the two is slightly better at higher redshift.

Both methods, used in this and previous sections have the same limitation. Each bin of the radial distribution is essentially weighted according to the number of galaxies it contains, meaning that the innermost regions tend to be traced better than the outer regions due to the rapid decline in the number density. But if we wanted to obtain a profile which describes the distribution of galaxies reasonably well over the entire radial range, it would be more reasonable for example to assign some constant error to each bin and use the least squares method. However, in that case, we would lose some of the statistical rigour and results for

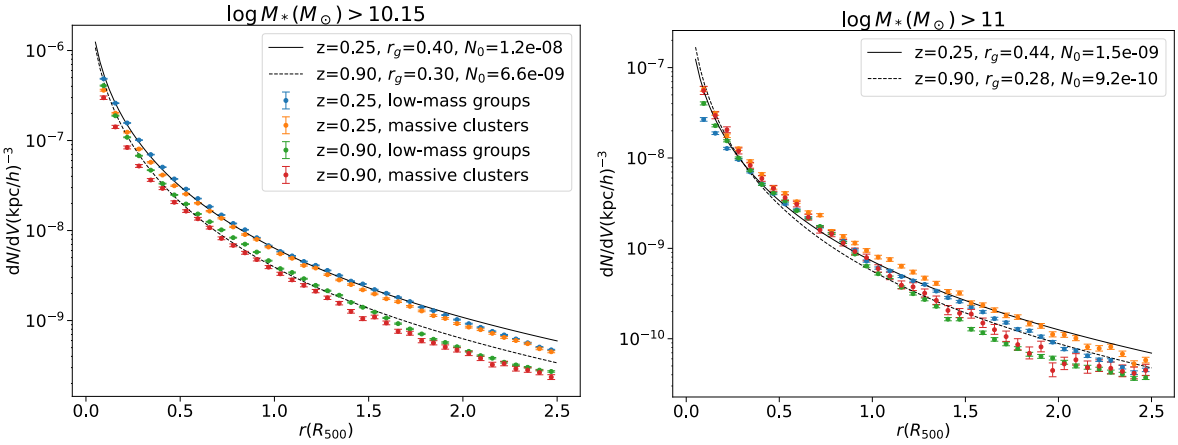

Figure B.2: Radial distribution of galaxies in low-mass ($13 < \log M_{500}(M_\odot) < 14$) and massive clusters ($\log M_{500}(M_\odot) > 14$) at low and high redshift. Combined data of low-mass groups and massive clusters (between 0.05 and $2R_{500}$) were used for fitting. On the left panel, all galaxies were used, while on the right panel, only massive galaxies were selected.

z	$\log M_{500}(M_\odot)$	med. r_g $[R_{500}]$	med. N_0 $\left[\left(\frac{\text{kpc}}{h}\right)^{-3}\right]$	σ_{r_g}	σ_{N_0}	ρ_{r_g,N_0}	c_{200}
0.25	[13,14]	3.7e-01	1.2e-08	2.5e+00	3.9e-07	0.85	4.14
	[14,15.3]	4.4e-01	1.2e-08	5.2e-01	2.8e-08	0.88	3.53
	[13,15.3]	3.7e-01	1.2e-08	2.5e+00	3.9e-07	0.85	4.09
0.90	[13,14]	3.0e-01	6.8e-09	2.2e+00	2.5e-07	0.83	5.04
	[14,14.7]	3.3e-01	6.0e-09	2.7e-01	5.1e-09	0.93	4.65
	[13,14.7]	3.0e-01	6.8e-09	2.2e+00	2.5e-07	0.83	5.02

Table B.4: The median value, standard deviation, Pearson correlation coefficient and concentration of the NFW parameters r_g and N_0, which are obtained by fitting the *individual* halos and obtaining the maximum of the posterior for each halo. The pairs of the best parameter values (r_g, N_0) are then used as a sample with which we obtain the medians and the variance. All galaxies between 0.05 and $2R_{500}$ with $\log M_*(M_\odot) > 10.15$ at low and high redshift and in low-mass and massive clusters were used. c_{200} is obtained from the median r_g and NFW profile (equation (1.11)).

individual clusters would be hardly meaningful anymore. I decided not to try alternative methods since the models in figure B.2 already seem to describe the range between 0.5 R_{500} and 2 R_{500} reasonably well.

B.5 Dark Matter Profiles

To better understand whether the difference between the redshift evolution of concentration, found in the literature (Bullock et al. 2001), and in simulations, is a consequence of using galaxies as dark matter tracers or is it merely a consequence of the statistical analysis, I did the same analysis with dark matter particles. In each dark matter halo, I randomly selected dark matter particles, so that their number matched the number of (all) galaxies, found in the same radial range (2 R_{500}) of the same cluster. I then stacked the profiles and calculated the expectation values $\langle r_g \rangle$ and $\langle N_0 \rangle$. Results are plotted in table B.5.

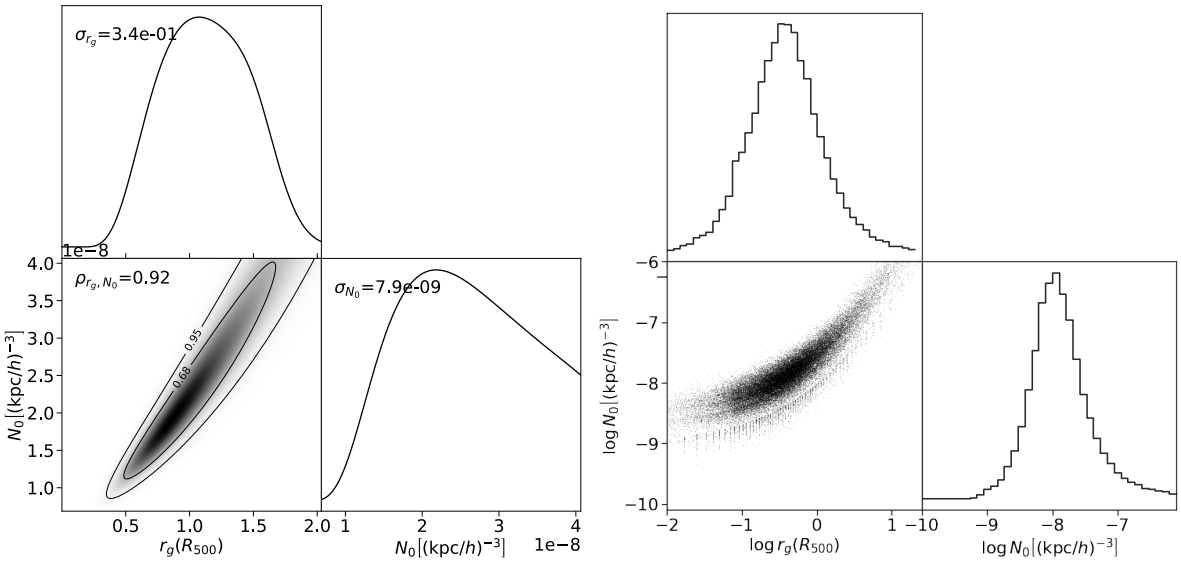

Figure B.3: Left panel: posterior probability density of parameters N_0 and r_g obtained with 243 galaxies in a single cluster with $\log M_{500}(M_\odot) = 14.4$ at low redshift. Riht panel: distribution of the best parameter values r_g and N_0, obtained from all galaxies in clusters above $\log M_{500}(M_\odot) > 13$ (each data point represents a cluster). 100 radial bins were used for fitting the individual profiles. Note that the distribution on the right panel is plotted in logarithmic scale.

In terms of redshift evolution, we now find the expected decrease of concentration with redshift in low-mass clusters, although an increase is only minor. In massive clusters, the concentration again seems to slightly increase with redshift. The concentration values generally agree with what is found by Ragagnin et al. (2019) using the same data. The redshift and mass dependence seem to be a bit discrepant in some cases, but it is important to point out that the redshift range and the mass range used here are very narrow, whereas in Ragagnin et al. (2019), the entire range from galaxy-size halos to very massive clusters from redshift 2 to redshift 0 is explored. In that sense, the almost constant concentration found here is not surprising. It also helps to put the concentration obtained with galaxies (table B.1) into perspective. The increase of the concentration of galaxies with redshift indeed is significant and is not found in dark matter distribution.

In figure B.4 I show the profiles of dark matter particles together with the NFW model. The model (obtained by considering regions up to $2R_{500}$) traces the dark matter density even beyond $2R_{500}$, which is not observed in the profile of galaxies (figure B.2). This indicates that the NFW model is more appropriate for describing the dark matter density and is only a crude approximation for the galaxy distribution.

z	$\log M_{500}(M_\odot)$	$\langle r_g \rangle\,[r_{500}]$	$\langle N_0 \rangle\,[(\mathrm{kpc}/h)^{-3}]$	σ_{r_g}	σ_{N_0}	ρ_{r_g,N_0}	c_{200}
0.25	[13,14]	4.08e-01	1.38e-08	1.9e-03	5.2e-11	0.91	3.77
	[14,15.3]	4.22e-01	1.18e-08	4.1e-03	9.2e-11	0.91	3.66
	[13,15.3]	4.11e-01	1.33e-08	1.7e-03	4.5e-11	0.91	3.75
0.90	[13,14]	4.26e-01	9.14e-09	2.6e-03	4.5e-11	0.91	3.63
	[14,14.7]	3.86e-01	6.68e-09	8.2e-03	1.1e-10	0.90	3.97
	[13,14.7]	4.23e-01	8.91e-09	2.5e-03	4.2e-11	0.91	3.65

Table B.5: Posterior expectation value, standard deviation, Pearson correlation coefficient and concentration of the NFW parameters r_g and N_0, fitted to the *dark matter* particles. In each cluster, we randomly select dark matter particles, so that their number corresponds to the number of (all) galaxies in that cluster. c_{200} is obtained from $\langle r_g \rangle$ and NFW profile (equation (1.11)).

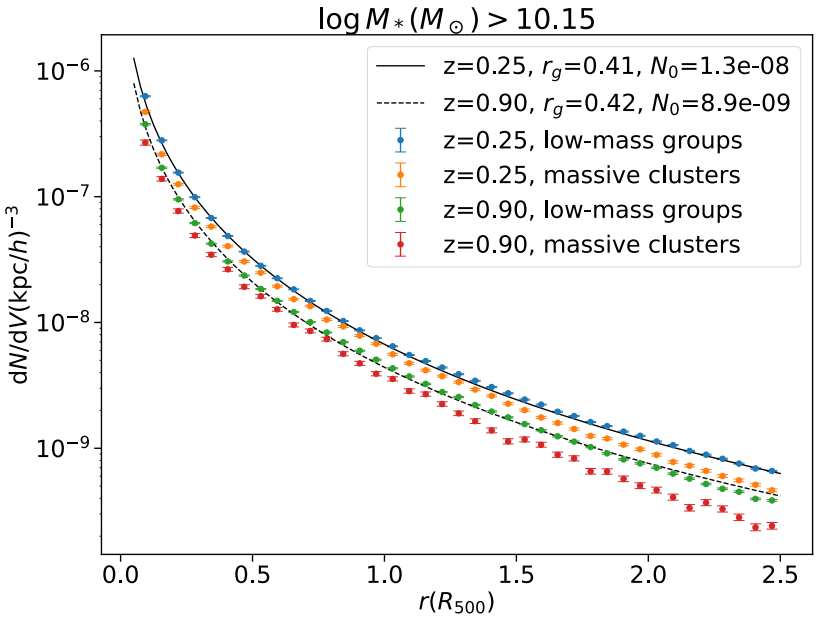

Figure B.4: Radial distribution of dark matter particles in low-mass groups ($13 < \log M_{500}(M_\odot) < 14$) and massive clusters ($\log M_{500}(M_\odot) > 14$) at low and high redshift. Combined data of low-mass groups and massive clusters (between 0.05 and $2R_{500}$) were used for fitting.

Appendix C

Koulouridis & Bartalucci (2019) results

In figure 5.21, I compare the results of this work to the results of the Koulouridis & Bartalucci (2019) paper, where a study of the distribution of X-ray selected AGNs in 5 massive clusters (above $M_{500} > 10^{14} M_{\odot}$) at redshift $z \sim 1$ is presented. They report an excess of AGNs with X-ray luminosity above $3 \cdot 10^{42}$ erg/s in [0.5-8] keV band between $2R_{500}$ and $2.5R_{500}$. Results are shown in figure C.1, where Σ is the total surface density of X-ray point sources in excess of the field value, divided by the optical galaxy profile:

$$\Sigma_i = \sum_{j=1}^{5} \left(X_{ij} - F_{ij} \right) / w_i A_{ij}. \tag{C.1}$$

The sum in equation (C.1) runs over 5 massive cluster, index i refers to the i-th annulus. X_{ij} is the number of AGNs in the i-th annulus of the j-th cluster, A_{ij} is the surface area of the annulus, F_{ij} is the number of AGNs in the field, per surface area A_{ij}, and the weights w_i are defined as $w_i = G_i / G_f$, where G_i is the surface density of optical galaxies in annulus i and G_f is the respective density in the field. Note that different cluster regions in Koulouridis & Bartalucci (2019) are chosen at slightly different redshifts (and the AGNs with the same luminosity have different X-ray flux), which means that the number densities of AGNs in the cluster regions X_{ij}/A_{ij} and in the field F_{ij}/A_{ij} vary between clusters. However, since they are expected to vary by the same factor, this can be also seen as the variation in the effective surface area of the annulus A_{ij} and should not drastically affect the following definitions.

In Chapter 5, I plot the fraction of galaxies, containing an X-ray bright AGN, relative to the background value, which is similar but not equivalent to quantity Σ_i shown here. In the fraction calculations, the background is not subtracted and the ratio goes to 1 for large r (and not 0). In notation above, the fraction of X-ray bright AGNs is expressed:

$$f = \left(\frac{\Sigma_{j=1}^{5} X_{ij}}{G_i \, \Sigma_{j=1}^{5} A_{ij}} \right) \left(\frac{\Sigma_{j=1}^{5} F_{ij}}{G_f \, \Sigma_{j=1}^{5} A_{ij}} \right)^{-1} = \frac{G_f}{G_i} \left(\frac{\Sigma_{j=1}^{5} X_{ij}}{\Sigma_{j=1}^{5} F_{ij}} \right). \tag{C.2}$$

This cannot be derived directly from quantity Σ_i, since in equation (C.1), the count only appears as a number density; the sum goes over X_{ij}/A_{ij} and not separately over X_{ij} and A_{ij}

which is required in the calculation of the mean number density. To get the AGN fraction f, some approximations have to be made. The mean number density can be expressed as $\Sigma_{j=1}^{5}\left(\frac{X_{ij}}{A_{ij}}\right)/5$, if the contributions of different clusters to the average are weighted equally, and if we neglect the different number densities due to the redshift variations. The fraction f is then defined:

$$f = \left(\sum_{j=1}^{5}\frac{X_{ij}}{A_{ij}}\frac{1}{5G_i}\right)\left(\sum_{j=1}^{5}\frac{F_{ij}}{A_{ij}}\frac{1}{5G_f}\right)^{-1} = \\ = \Sigma_i\left(\sum_{j=1}^{5}\frac{F_{ij}}{A_{ij}}\right)^{-1} + w_i^{-1}, \tag{C.3}$$

where the fraction f was expressed with Σ_i according to equation (C.1). Assuming that w_i follows the NFW profile that increases towards the centre, the w_i^{-1} term introduces the central decline, seen in other studies in figure 5.21. For w_i I assume the NFW profile with $r_g = 5$ (see Appendix B), the normalization is chosen so that the background value (1) is reached at $r = 4R_{500}$. The value of the factor $\left(\Sigma_{j=1}^{5} F_{ij}/A_{ij}\right)^{-1}$ is set to 1 Mpc^{-2}, based on the order of magnitude estimate from the data in Koulouridis & Bartalucci (2019). Note that the Koulouridis & Bartalucci (2019) data in figure 5.21 are not meant for direct comparison but rather to guide the eye.

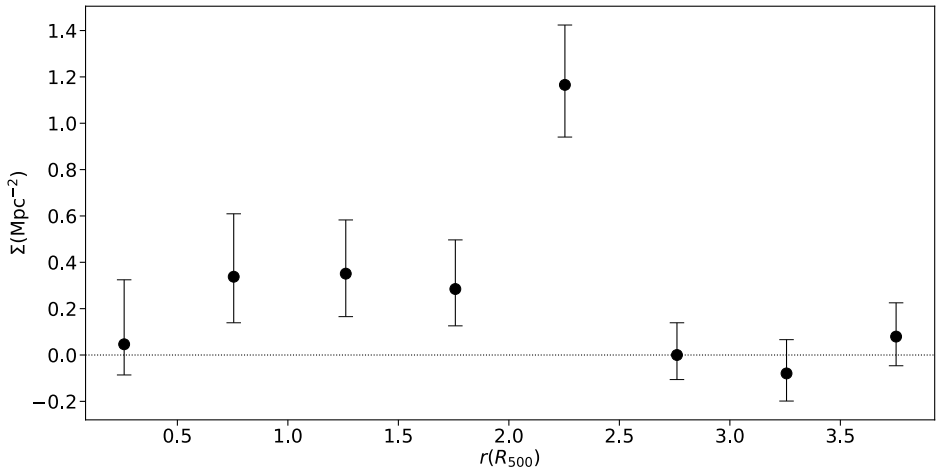

Figure C.1: Total surface density of X-ray point sources in massive galaxy clusters at high redshift, in excess of the field value, divided by the optical galaxy profile (equation (C.1)), as a function of r. Data taken from Figure 1 in Koulouridis & Bartalucci (2019).

Appendix D

Corner Plots

In this section, I plot the AGN fraction, median black hole mass of black holes with $M_\bullet > 10^8 M_\odot$ and median X-ray luminosity of AGNs with $L_x > 10^{42}$ erg/s, as functions of the clustercentric distance r, stellar mass M_*, parent cluster mass M_{500}, specific star formation rate sSFR, and the distance to the nearest neighbour d_n. The figures are arranged into concise corner diagrams, which allow us to quickly identify the populations of galaxies displaying interesting behaviour. The contours on the diagrams represent the distribution of galaxies, while the color depicts the fraction, median black hole mass or luminosity. The bins with low count are excluded (see section 5.1). In the uppermost panels, the fraction, mass or luminosity are plotted as functions of a single property, for all galaxies, star-forming, quiescent and very massive galaxies (despite different labels, the definition of star-forming galaxies is the same as used throughout this work and described in section 2.6). In the panels with sSFR, the horizontal dotted line represents the "blueness criterion" threshold, defined in section 2.6. The main parameters, used for galaxy selection, are printed out in the title of each plot. Despite not being shown in the main body of the thesis, such corner plots have been instrumental in directing the presented analysis, and are hence included here in hopes of providing additional insight for the reader.

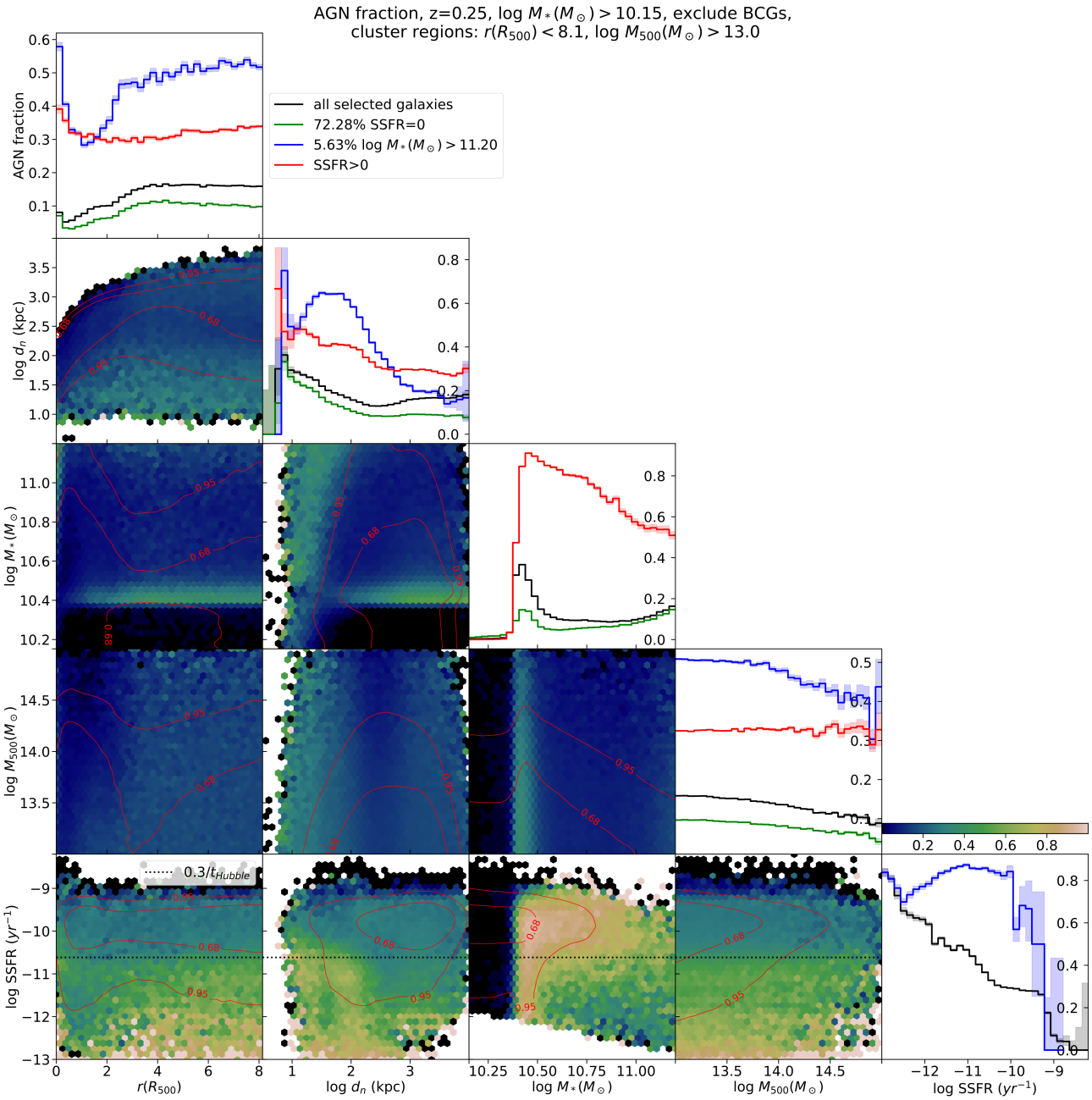

Figure D.1: Fraction of galaxies hosting an X-ray bright AGN as a function of d_n, M_*, M_{500} and sSFR.

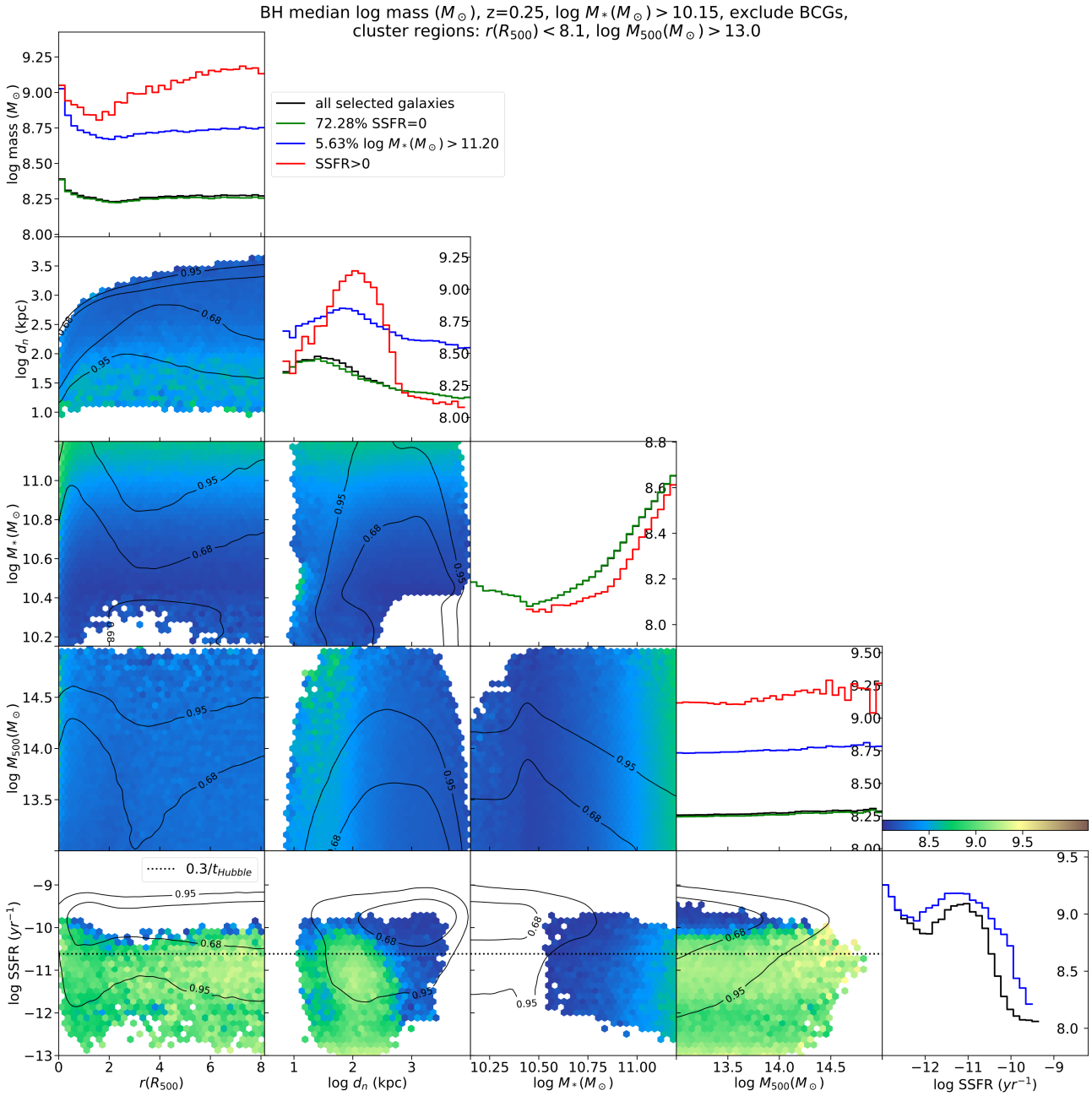

Figure D.2: Median mass of supermassive black holes as a function of d_n, M_*, M_{500} and sSFR of the host galaxy. Colorbar represents the logarithm of the mass of black holes with mass above $10^8 M_\odot$ in $M_\odot$.

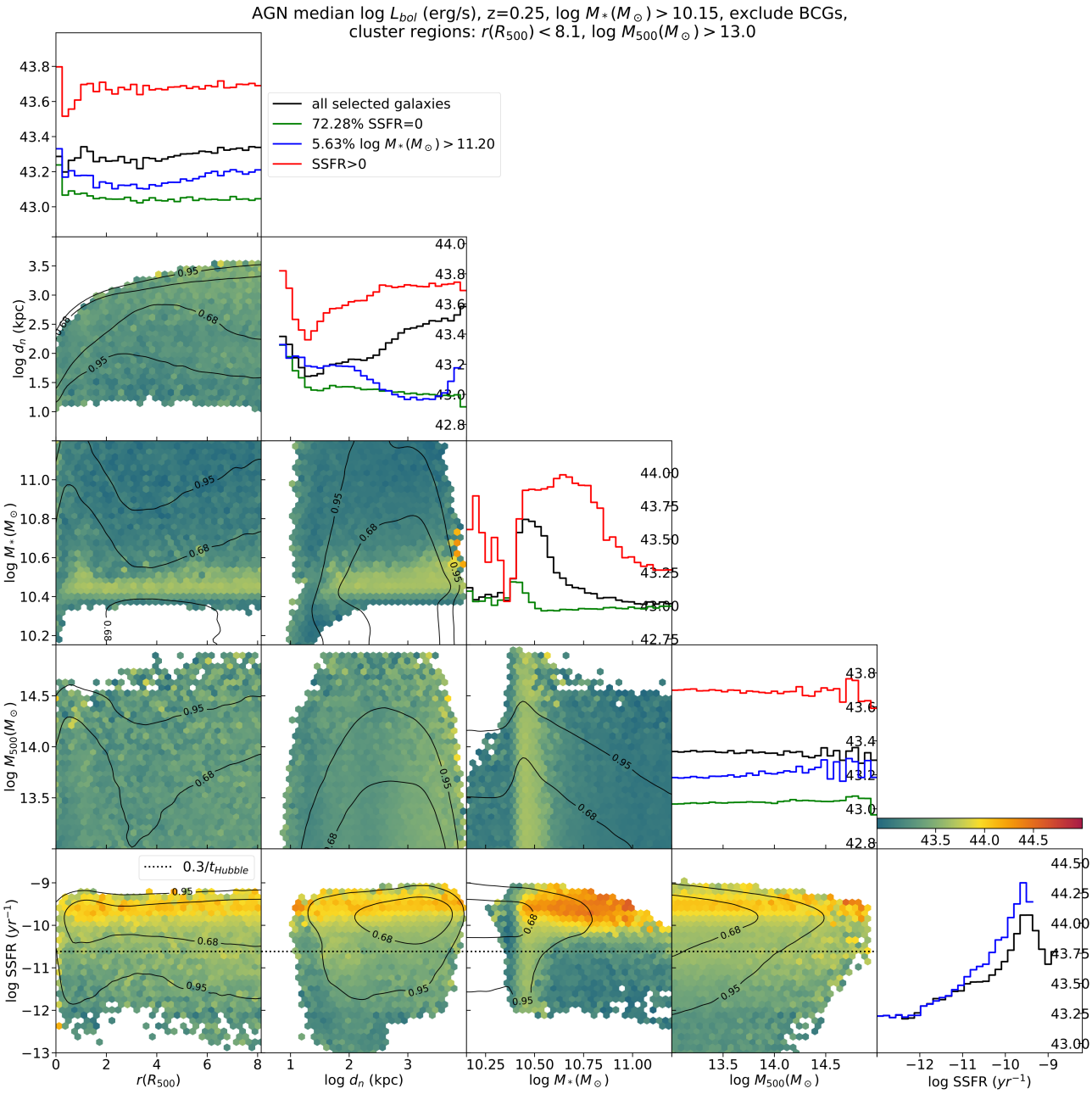

Figure D.3: Median X-ray luminosity as a function of d_n, M_*, M_{500} and sSFR of the host galaxy. Colorbar represents the logarithm of X-ray luminosity in erg/s ([0.5, 10] keV), of AGNs, brighter than 10^{42} erg/s.

References

Abramson, L. E., Kelson, D. D., Dressler, A., Poggianti, B., Gladders, M. D., Oemler, J., Augustus, & Vulcani, B. (2014). The Mass-independence of Specific Star Formation Rates in Galactic Disks. *ApJ*, *785*(2), L36.

Arth, A., Dolag, K., Beck, A. M., Petkova, M., & Lesch, H. (2014). Anisotropic thermal conduction in galaxy clusters with MHD in Gadget. *arXiv e-prints*, (p. arXiv:1412.6533).

Bahcall, N. A., & Kulier, A. (2014). Tracing mass and light in the Universe: where is the dark matter? *MNRAS*, *439*(3), 2505–2514.

Balick, B., & Brown, R. L. (1974). Intense sub-arcsecond structure in the galactic center. *ApJ*, *194*, 265–270.

Balogh, M. L., Schade, D., Morris, S. L., Yee, H. K. C., Carlberg, R. G., & Ellingson, E. (1998). The Dependence of Cluster Galaxy Star Formation Rates on the Global Environment. *ApJ*, *504*(2), L75–L78.

Basilakos, S., & Plionis, M. (2004). Modelling the two-point correlation function of galaxy clusters in the Sloan Digital Sky Survey. *MNRAS*, *349*(3), 882–888.

Beck, A. M., Murante, G., Arth, A., Remus, R. S., Teklu, A. F., Donnert, J. M. F., Planelles, S., Beck, M. C., Förster, P., Imgrund, M., Dolag, K., & Borgani, S. (2016). An improved SPH scheme for cosmological simulations. *MNRAS*, *455*(2), 2110–2130.

Bekki, K., & Couch, W. J. (2003). Starbursts from the Strong Compression of Galactic Molecular Clouds due to the High Pressure of the Intracluster Medium. *ApJ*, *596*(1), L13–L16.

Benavides, J. A., Sales, L. V., & Abadi, M. G. (2020). Accretion of galaxy groups into galaxy clusters. *MNRAS*, *498*(3), 3852–3862.

Biffi, V., Dolag, K., & Böhringer, H. (2013). Investigating the velocity structure and X-ray observable properties of simulated galaxy clusters with PHOX. *MNRAS*, *428*(2), 1395–1409.

Biffi, V., Dolag, K., Böhringer, H., & Lemson, G. (2012). Observing simulated galaxy clusters with PHOX: a novel X-ray photon simulator. *MNRAS*, *420*(4), 3545–3556.

Biffi, V., Dolag, K., & Merloni, A. (2018). AGN contamination of galaxy-cluster thermal X-ray emission: predictions for eRosita from cosmological simulations. *MNRAS*, *481*(2), 2213–2227.

Boggs, P. T., & Donaldson, J. R. (1989). Orthogonal distance regression.

Bolton, C. T. (1972). Identification of Cygnus X-1 with HDE 226868. *Nature*, *235*(5336), 271–273.

Bond, J. R., Cole, S., Efstathiou, G., & Kaiser, N. (1991). Excursion Set Mass Functions for Hierarchical Gaussian Fluctuations. *ApJ*, *379*, 440.

Bondi, H. (1952). On spherically symmetrical accretion. *MNRAS*, *112*, 195.

Borgani, S., & Kravtsov, A. (2011). Cosmological Simulations of Galaxy Clusters. *Advanced Science Letters*, *4*(2), 204–227.

Boselli, A., & Gavazzi, G. (2006). Environmental Effects on Late-Type Galaxies in Nearby Clusters. *PASP*, *118*(842), 517–559.

Boylan-Kolchin, M., Ma, C.-P., & Quataert, E. (2008). Dynamical friction and galaxy merging time-scales. *MNRAS*, *383*(1), 93–101.

Bradač, M., Clowe, D., Gonzalez, A. H., Marshall, P., Forman, W., Jones, C., Markevitch, M., Randall, S., Schrabback, T., & Zaritsky, D. (2006). Strong and Weak Lensing United. III. Measuring the Mass Distribution of the Merging Galaxy Cluster 1ES 0657-558. *ApJ*, *652*(2), 937–947.

Brandt, W. N., & Hasinger, G. (2005). Deep Extragalactic X-Ray Surveys. *ARA&A*, *43*(1), 827–859.

Budzynski, J. M., Koposov, S. E., McCarthy, I. G., McGee, S. L., & Belokurov, V. (2012). The radial distribution of galaxies in groups and clusters. *MNRAS*, *423*(1), 104–121.

Bullock, J. S., Kolatt, T. S., Sigad, Y., Somerville, R. S., Kravtsov, A. V., Klypin, A. A., Primack, J. R., & Dekel, A. (2001). Profiles of dark haloes: evolution, scatter and environment. *MNRAS*, *321*(3), 559–575.

Cantalupo, S. (2010). Stars quenching stars: how photoionization by local sources regulates gas cooling and galaxy formation. *MNRAS*, *403*(1), L16–L20.

Carroll, S. (2019). *Spacetime and Geometry*. Cambridge University Press.
URL https://books.google.si/books?id=PTGdDwAAQBAJ

Choque-Challapa, N., Smith, R., Candlish, G., Peletier, R., & Shin, J. (2019). Leavers and remainers: galaxies split by group-exit. *MNRAS*, *490*(3), 3654–3666.

Christlein, D., & Zabludoff, A. I. (2005). Disentangling Morphology, Star Formation, Stellar Mass, and Environment in Galaxy Evolution. *ApJ*, *621*(1), 201–214.

Churazov, E., Sazonov, S., Sunyaev, R., Forman, W., Jones, C., & Böhringer, H. (2005). Supermassive black holes in elliptical galaxies: switching from very bright to very dim. *MNRAS*, *363*(1), L91–L95.

Cimatti, A., Fraternali, F., & Nipoti, C. (2019). *Introduction to Galaxy Formation and Evolution: From Primordial Gas to Present-Day Galaxies*. Cambridge University Press. URL https://books.google.si/books?id=rJCuDwAAQBAJ

Clowe, D., Bradač, M., Gonzalez, A. H., Markevitch, M., Randall, S. W., Jones, C., & Zaritsky, D. (2006). A Direct Empirical Proof of the Existence of Dark Matter. *ApJ*, *648*(2), L109–L113.

Cohen, S. A., Hickox, R. C., Wegner, G. A., Einasto, M., & Vennik, J. (2014). Star Formation and Substructure in Galaxy Clusters. *ApJ*, *783*(2), 136.

Croton, D. J. (2013). Damn You, Little h! (Or, Real-World Applications of the Hubble Constant Using Observed and Simulated Data). *PASA*, *30*, e052.

Di Matteo, T., Springel, V., & Hernquist, L. (2005). Energy input from quasars regulates the growth and activity of black holes and their host galaxies. *Nature*, *433*(7026), 604–607.

Diamond-Stanic, A. M., & Rieke, G. H. (2012). The Relationship between Black Hole Growth and Star Formation in Seyfert Galaxies. *ApJ*, *746*(2), 168.

Dolag, K., Borgani, S., Murante, G., & Springel, V. (2009). Substructures in hydrodynamical cluster simulations. *MNRAS*, *399*(2), 497–514.

Dolag, K., Komatsu, E., & Sunyaev, R. (2016). SZ effects in the Magneticum Pathfinder simulation: comparison with the Planck, SPT, and ACT results. *MNRAS*, *463*(2), 1797–1811.

Dolag, K., Reinecke, M., Gheller, C., & Imboden, S. (2008). Splotch: visualizing cosmological simulations. *New Journal of Physics*, *10*(12), 125006.

Dolag, K., Vazza, F., Brunetti, G., & Tormen, G. (2005). Turbulent gas motions in galaxy cluster simulations: the role of smoothed particle hydrodynamics viscosity. *MNRAS*, *364*(3), 753–772.

Eckart, A., & Genzel, R. (1996). Observations of stellar proper motions near the Galactic Centre. *Nature*, *383*(6599), 415–417.

Ehlert, S., Allen, S. W., Brandt, W. N., Canning, R. E. A., Luo, B., Mantz, A., Morris, R. G., von der Linden, A., & Xue, Y. Q. (2015). X-ray bright active galactic nuclei in massive galaxy clusters - III. New insights into the triggering mechanisms of cluster AGN. *MNRAS*, *446*(3), 2709–2729.

Ehlert, S., Allen, S. W., Brandt, W. N., Xue, Y. Q., Luo, B., von der Linden, A., Mantz, A., & Morris, R. G. (2013a). X-ray bright active galactic nuclei in massive galaxy clusters - I. Number counts and spatial distribution. *MNRAS*, *428*(4), 3509–3525.

Ehlert, S., von der Linden, A., Allen, S. W., Brandt, W. N., Xue, Y. Q., Luo, B., Mantz, A., Morris, R. G., Applegate, D., & Kelly, P. (2014). X-ray bright active galactic nuclei in massive galaxy clusters - II. The fraction of galaxies hosting active nuclei. *MNRAS*, *437*(2), 1942–1949.

Ehlert, S., Werner, N., Simionescu, A., Allen, S. W., Kenney, J. D. P., Million, E. T., & Finoguenov, A. (2013b). Ripping apart at the seams: the network of stripped gas surrounding M86. *MNRAS*, *430*(3), 2401–2410.

Einasto, J. (1965). On the Construction of a Composite Model for the Galaxy and on the Determination of the System of Galactic Parameters. *Trudy Astrofizicheskogo Instituta Alma-Ata*, *5*, 87–100.

Einstein, A. (1917). Kosmologische Betrachtungen zur allgemeinen Relativitätstheorie. *Sitzungsberichte der Königlich Preußischen Akademie der Wissenschaften (Berlin*, (pp. 142–152).

Event Horizon Telescope Collaboration (2019). First M87 Event Horizon Telescope Results. I. The Shadow of the Supermassive Black Hole. *ApJ*, *875*(1), L1.

Event Horizon Telescope Collaboration (2022). First Sagittarius A* Event Horizon Telescope Results. I. The Shadow of the Supermassive Black Hole in the Center of the Milky Way. *ApJ*, *930*(2), L12.

Evrard, A. E. (1991). Clues to galaxy activity from rich cluster simulations. *MNRAS*, *248*, 8P–10P.

Fabjan, D., Borgani, S., Tornatore, L., Saro, A., Murante, G., & Dolag, K. (2010). Simulating the effect of active galactic nuclei feedback on the metal enrichment of galaxy clusters. *MNRAS*, *401*(3), 1670–1690.

Fassbender, R., Šuhada, R., & Nastasi, A. (2012). AGN Triggering in the Infall Regions of Distant X-Ray Luminous Galaxy Clusters at $0.9 < z <_{\sim} 1.6$. *Advances in Astronomy*, *2012*, 138380.

Fath, E. A. (1909). The spectra of some spiral nebulae and globular star clusters. *Lick Observatory Bulletin*, *149*, 71–77.

Ferland, G. J., Korista, K. T., Verner, D. A., Ferguson, J. W., Kingdon, J. B., & Verner, E. M. (1998). CLOUDY 90: Numerical Simulation of Plasmas and Their Spectra. *PASP*, *110*(749), 761–778.

Florez, J., Jogee, S., Sherman, S., Stevans, M. L., Finkelstein, S. L., Papovich, C., Kawinwanichakij, L., Ciardullo, R., Gronwall, C., Urry, C. M., Kirkpatrick, A., LaMassa, S. M., Ananna, T. T., & Wold, I. (2020). Exploring AGN and star formation activity of massive galaxies at cosmic noon. *MNRAS*, *497*(3), 3273–3296.

Franx, M., van Dokkum, P. G., Förster Schreiber, N. M., Wuyts, S., Labbé, I., & Toft, S. (2008). Structure and Star Formation in Galaxies out to z = 3: Evidence for Surface Density Dependent Evolution and Upsizing. *ApJ*, *688*(2), 770–788.

Friedmann, A. (1924). Über die Möglichkeit einer Welt mit konstanter negativer Krümmung des Raumes. *Zeitschrift fur Physik*, *21*(1), 326–332.

Gehrels, N. (1986). Confidence Limits for Small Numbers of Events in Astrophysical Data. *ApJ*, *303*, 336.

Giocoli, C., Tormen, G., & van den Bosch, F. C. (2008). The population of dark matter subhaloes: mass functions and average mass-loss rates. *MNRAS*, *386*(4), 2135–2144.

Haardt, F., & Madau, P. (2001). Modelling the UV/X-ray cosmic background with CUBA. In D. M. Neumann, & J. T. V. Tran (Eds.) *Clusters of Galaxies and the High Redshift Universe Observed in X-rays*, (p. 64).

Haggard, D., Green, P. J., Anderson, S. F., Constantin, A., Aldcroft, T. L., Kim, D.-W., & Barkhouse, W. A. (2010). The Field X-ray AGN Fraction to z = 0.7 from the Chandra Multiwavelength Project and the Sloan Digital Sky Survey. *ApJ*, *723*(2), 1447–1468.

Haight, F. A. (1967). *Handbook of the Poisson distribution [by] Frank A. Haight*. Wiley New York.

Haines, C. P., Pereira, M. J., Sanderson, A. J. R., Smith, G. P., Egami, E., Babul, A., Edge, A. C., Finoguenov, A., Moran, S. M., & Okabe, N. (2012). LoCuSS: A Dynamical Analysis of X-Ray Active Galactic Nuclei in Local Clusters. *ApJ*, *754*(2), 97.

Hashimoto, Y., Oemler, J., Augustus, Lin, H., & Tucker, D. L. (1998). The Influence of Environment on the Star Formation Rates of Galaxies. *ApJ*, *499*(2), 589–599.

Hernquist, L., & Mihos, J. C. (1995). Excitation of Activity in Galaxies by Minor Mergers. *ApJ*, *448*, 41.

Hirschmann, M., Dolag, K., Saro, A., Bachmann, L., Borgani, S., & Burkert, A. (2014). Cosmological simulations of black hole growth: AGN luminosities and downsizing. *MNRAS*, *442*(3), 2304–2324.

Hubble, E. (1929). A Relation between Distance and Radial Velocity among Extra-Galactic Nebulae. *Contributions from the Mount Wilson Observatory*, *3*, 23–28.

Hwang, H. S., Shin, J., & Song, H. (2019). Evolution of star formation rate-density relation over cosmic time in a simulated universe: the observed reversal reproduced. *MNRAS*, *489*(1), 339–348.

Iodice, E., Sarzi, M., Bittner, A., Coccato, L., Costantin, L., Corsini, E. M., van de Ven, G., de Zeeuw, P. T., Falcón-Barroso, J., Gadotti, D. A., Lyubenova, M., Martín-Navarro, I., McDermid, R. M., Nedelchev, B., Pinna, F., Pizzella, A., Spavone, M., & Viaene, S. (2019). The Fornax3D project: Tracing the assembly history of the cluster from the kinematic and line-strength maps. *A&A*, *627*, A136.

Jauzac, M., Eckert, D., Schwinn, J., Harvey, D., Baugh, C. M., Robertson, A., Bose, S., Massey, R., Owers, M., Ebeling, H., Shan, H. Y., Jullo, E., Kneib, J. P., Richard, J., Atek, H., Clément, B., Egami, E., Israel, H., Knowles, K., Limousin, M., Natarajan, P., Rexroth, M., Taylor, P., & Tchernin, C. (2016). The extraordinary amount of substructure in the Hubble Frontier Fields cluster Abell 2744. *MNRAS*, *463*(4), 3876–3893.

Jing, Y. P. (2000). The Density Profile of Equilibrium and Nonequilibrium Dark Matter Halos. *ApJ*, *535*(1), 30–36.

King, I. R. (1972). Density Data and Emission Measure for a Model of the Coma Cluster. *ApJ*, *174*, L123.

Klypin, A., Yepes, G., Gottlöber, S., Prada, F., & Heß, S. (2016). MultiDark simulations: the story of dark matter halo concentrations and density profiles. *MNRAS*, *457*(4), 4340–4359.

Komatsu, E., Dunkley, J., Nolta, M. R., Bennett, C. L., Gold, B., Hinshaw, G., Jarosik, N., Larson, D., Limon, M., Page, L., Spergel, D. N., Halpern, M., Hill, R. S., Kogut, A., Meyer, S. S., Tucker, G. S., Weiland, J. L., Wollack, E., & Wright, E. L. (2009). Five-Year Wilkinson Microwave Anisotropy Probe Observations: Cosmological Interpretation. *ApJS*, *180*(2), 330–376.

Koulouridis, E., & Bartalucci, I. (2019). High density of active galactic nuclei in the outskirts of distant galaxy clusters. *A&A*, *623*, L10.

Koulouridis, E., & Plionis, M. (2010). Luminous X-ray Active Galactic Nuclei in Clusters of Galaxies. *ApJ*, *714*(2), L181–L184.

Koulouridis, E., Ricci, M., Giles, P., Adami, C., Ramos-Ceja, M., Pierre, M., Plionis, M., Lidman, C., Georgantopoulos, I., Chiappetti, L., Elyiv, A., Ettori, S., Faccioli, L., Fotopoulou, S., Gastaldello, F., Pacaud, F., Paltani, S., & Vignali, C. (2018). The XXL Survey. XXXV. The role of cluster mass in AGN activity. *A&A*, *620*, A20.

Kulier, A., Ostriker, J. P., Natarajan, P., Lackner, C. N., & Cen, R. (2015). Understanding Black Hole Mass Assembly via Accretion and Mergers at Late Times in Cosmological Simulations. *ApJ*, *799*(2), 178.

Landy, S. D., & Szalay, A. S. (1993). Bias and Variance of Angular Correlation Functions. *ApJ*, *412*, 64.

Lemaître, G. (1927). Un Univers homogène de masse constante et de rayon croissant rendant compte de la vitesse radiale des nébuleuses extra-galactiques. *Annales de la Société Scientifique de Bruxelles*, *47*, 49–59.

Leslie, S. K., Kewley, L. J., Sanders, D. B., & Lee, N. (2016). Quenching star formation: insights from the local main sequence. *MNRAS*, *455*(1), L82–L86.

Lidman, C., Suherli, J., Muzzin, A., Wilson, G., Demarco, R., Brough, S., Rettura, A., Cox, J., DeGroot, A., Yee, H. K. C., Gilbank, D., Hoekstra, H., Balogh, M., Ellingson, E., Hicks, A., Nantais, J., Noble, A., Lacy, M., Surace, J., & Webb, T. (2012). Evidence for significant growth in the stellar mass of brightest cluster galaxies over the past 10 billion years. *MNRAS*, *427*(1), 550–568.

Lotz, M., Dolag, K., Remus, R.-S., & Burkert, A. (2021). Rise and fall of post-starburst galaxies in Magneticum Pathfinder. *MNRAS*, *506*(3), 4516–4542.

Lotz, M., Remus, R.-S., Dolag, K., Biviano, A., & Burkert, A. (2019). Gone after one orbit: How cluster environments quench galaxies. *MNRAS*, *488*(4), 5370–5389.

Magorrian, J., Tremaine, S., Richstone, D., Bender, R., Bower, G., Dressler, A., Faber, S. M., Gebhardt, K., Green, R., Grillmair, C., Kormendy, J., & Lauer, T. (1998). The Demography of Massive Dark Objects in Galaxy Centers. *AJ*, *115*(6), 2285–2305.

Maio, U., Dotti, M., Petkova, M., Perego, A., & Volonteri, M. (2013). Effects of Circumnuclear Disk Gas Evolution on the Spin of Central Black Holes. *ApJ*, *767*(1), 37.

Marconi, A., Risaliti, G., Gilli, R., Hunt, L. K., Maiolino, R., & Salvati, M. (2004). Local supermassive black holes, relics of active galactic nuclei and the X-ray background. *MNRAS*, *351*(1), 169–185.

Martini, P., Mulchaey, J. S., & Kelson, D. D. (2007). The Distribution of Active Galactic Nuclei in Clusters of Galaxies. *ApJ*, *664*(2), 761–776.

Moore, B., Katz, N., Lake, G., Dressler, A., & Oemler, A. (1996). Galaxy harassment and the evolution of clusters of galaxies. *Nature*, *379*(6566), 613–616.

Muldrew, S. I., Croton, D. J., Skibba, R. A., Pearce, F. R., Ann, H. B., Baldry, I. K., Brough, S., Choi, Y.-Y., Conselice, C. J., Cowan, N. B., Gallazzi, A., Gray, M. E., Grützbauch, R., Li, I. H., Park, C., Pilipenko, S. V., Podgorzec, B. J., Robotham, A. S. G., Wilman, D. J., Yang, X., Zhang, Y., & Zibetti, S. (2012). Measures of galaxy environment - I. What is 'environment'? *MNRAS*, *419*(3), 2670–2682.

Mullaney, J. R., Daddi, E., Béthermin, M., Elbaz, D., Juneau, S., Pannella, M., Sargent, M. T., Alexander, D. M., & Hickox, R. C. (2012). The Hidden "AGN Main Sequence": Evidence for a Universal Black Hole Accretion to Star Formation Rate Ratio since z ~2 Producing an M $_{BH}$-M $_{*}$ Relation. *ApJ*, *753*(2), L30.

Muzzin, A., Wilson, G., Yee, H. K. C., Gilbank, D., Hoekstra, H., Demarco, R., Balogh, M., van Dokkum, P., Franx, M., Ellingson, E., Hicks, A., Nantais, J., Noble, A., Lacy, M., Lidman, C., Rettura, A., Surace, J., & Webb, T. (2012). The Gemini Cluster Astrophysics Spectroscopic Survey (GCLASS): The Role of Environment and Self-regulation in Galaxy Evolution at z ~1. *ApJ*, *746*(2), 188.

Nagai, D., & Kravtsov, A. V. (2005). The Radial Distribution of Galaxies in Λ Cold Dark Matter Clusters. *ApJ*, *618*(2), 557–568.

Natarajan, P., Kneib, J.-P., Smail, I., Treu, T., Ellis, R., Moran, S., Limousin, M., & Czoske, O. (2009). The Survival of Dark Matter Halos in the Cluster Cl 0024+16. *ApJ*, *693*(1), 970–983.

Navarro, J. F., Frenk, C. S., & White, S. D. M. (1995). Simulations of X-ray clusters. *MNRAS*, *275*(3), 720–740.

Navarro, J. F., Frenk, C. S., & White, S. D. M. (1996). The Structure of Cold Dark Matter Halos. *ApJ*, *462*, 563.

Navarro, J. F., Frenk, C. S., & White, S. D. M. (1997). A Universal Density Profile from Hierarchical Clustering. *ApJ*, *490*(2), 493–508.

Netzer, H. (2013). *The Physics and Evolution of Active Galactic Nuclei*. Cambridge University Press.
URL https://books.google.si/books?id=OYkgAwAAQBAJ

Pacucci, F., & Loeb, A. (2020). Separating Accretion and Mergers in the Cosmic Growth of Black Holes with X-Ray and Gravitational-wave Observations. *ApJ*, *895*(2), 95.

Padovani, P., Alexander, D. M., Assef, R. J., De Marco, B., Giommi, P., Hickox, R. C., Richards, G. T., Smolčić, V., Hatziminaoglou, E., Mainieri, V., & Salvato, M. (2017). Active galactic nuclei: what's in a name? *A&A Rev.*, *25*(1), 2.

Park, T., Kashyap, V. L., Siemiginowska, A., van Dyk, D. A., Zezas, A., Heinke, C., & Wargelin, B. J. (2006). Bayesian Estimation of Hardness Ratios: Modeling and Computations. *ApJ*, *652*(1), 610–628.

Pearson, W. J., Wang, L., Hurley, P. D., Małek, K., Buat, V., Burgarella, D., Farrah, D., Oliver, S. J., Smith, D. J. B., & van der Tak, F. F. S. (2018). Main sequence of star forming galaxies beyond the Herschel confusion limit. *A&A*, *615*, A146.

Peebles, P. J. E. (1980). *The large-scale structure of the universe*.

Peng, Y.-j., Lilly, S. J., Kovač, K., Bolzonella, M., Pozzetti, L., Renzini, A., Zamorani, G., Ilbert, O., Knobel, C., Iovino, A., Maier, C., Cucciati, O., Tasca, L., Carollo, C. M., Silverman, J., Kampczyk, P., de Ravel, L., Sanders, D., Scoville, N., Contini, T., Mainieri, V., Scodeggio, M., Kneib, J.-P., Le Fèvre, O., Bardelli, S., Bongiorno, A., Caputi, K., Coppa, G., de la Torre, S., Franzetti, P., Garilli, B., Lamareille, F., Le Borgne, J.-F., Le Brun, V., Mignoli, M., Perez Montero, E., Pello, R., Ricciardelli, E., Tanaka, M., Tresse, L., Vergani, D., Welikala, N., Zucca, E., Oesch, P., Abbas, U., Barnes, L., Bordoloi, R., Bottini, D., Cappi, A., Cassata, P., Cimatti, A., Fumana, M., Hasinger, G., Koekemoer, A., Leauthaud, A., Maccagni, D., Marinoni, C., McCracken, H., Memeo, P., Meneux, B., Nair, P., Porciani, C., Presotto, V., & Scaramella, R. (2010). Mass and Environment as Drivers of Galaxy Evolution in SDSS and zCOSMOS and the Origin of the Schechter Function. *ApJ*, *721*(1), 193–221.

Penzias, A. A., & Wilson, R. W. (1965). A Measurement of Excess Antenna Temperature at 4080 Mc/s. *ApJ*, *142*, 419–421.

Planck Collaboration (2020). Planck 2018 results. VI. Cosmological parameters. *A&A*, *641*, A6.

Poggianti, B. M., Bellhouse, C., Deb, T., Franchetto, A., Fritz, J., George, K., Gullieuszik, M., Jaffé, Y., Moretti, A., Mueller, A., Radovich, M., Ramatsoku, M., Vulcani, B., & GASP Team (2021). The role of environment on quenching, star formation and AGN activity. In T. Storchi Bergmann, W. Forman, R. Overzier, & R. Riffel (Eds.) *Galaxy Evolution and Feedback across Different Environments*, vol. 359, (pp. 108–116).

Poggianti, B. M., De Lucia, G., Varela, J., Aragon-Salamanca, A., Finn, R., Desai, V., von der Linden, A., & White, S. D. M. (2010). The evolution of the density of galaxy clusters and groups: denser environments at higher redshifts. *MNRAS*, *405*(2), 995–1005.

Press, W. H., & Schechter, P. (1974). Formation of Galaxies and Clusters of Galaxies by Self-Similar Gravitational Condensation. *ApJ*, *187*, 425–438.

Ragagnin, A., Dolag, K., Moscardini, L., Biviano, A., & D'Onofrio, M. (2019). Dependency of halo concentration on mass, redshift and fossilness in Magneticum hydrodynamic simulations. *MNRAS*, *486*(3), 4001–4012.

Rees, M. J. (1978). Quasars. *The Observatory*, *98*, 210–223.

Rodriguez-Gomez, V., Genel, S., Vogelsberger, M., Sijacki, D., Pillepich, A., Sales, L. V., Torrey, P., Snyder, G., Nelson, D., Springel, V., Ma, C.-P., & Hernquist, L. (2015). The merger rate of galaxies in the Illustris simulation: a comparison with observations and semi-empirical models. *MNRAS*, *449*(1), 49–64.

Ruderman, J. T., & Ebeling, H. (2005). The Origin of the Spatial Distribution of X-Ray-luminous Active Galactic Nuclei in Massive Galaxy Clusters. *ApJ*, *623*(2), L81–L84.

Salpeter, E. E. (1964). Accretion of Interstellar Matter by Massive Objects. *ApJ*, *140*, 796–800.

Santos, J. S., Altieri, B., Valtchanov, I., Nastasi, A., Bohringer, H., Cresci, G., Elbaz, D., Fassbender, R., Rosati, P., Tozzi, P., & Verdugo, M. (2015). The reversal of the SF-density relation in a massive, X-ray-selected galaxy cluster at z = 1.58: results from Herschel. *MNRAS*, *447*, L65–L69.

Sarazin, C. (1988). *X-Ray Emission from Clusters of Galaxies*. Cambridge Astrophysics. Cambridge University Press.
URL https://books.google.si/books?id=8cAFDf0NaOoC

Schmidt, M. (1963). 3C 273 : A Star-Like Object with Large Red-Shift. *Nature*, *197*(4872), 1040.

Schreiber, C., Pannella, M., Elbaz, D., Béthermin, M., Inami, H., Dickinson, M., Magnelli, B., Wang, T., Aussel, H., Daddi, E., Juneau, S., Shu, X., Sargent, M. T., Buat, V., Faber, S. M., Ferguson, H. C., Giavalisco, M., Koekemoer, A. M., Magdis, G., Morrison, G. E., Papovich, C., Santini, P., & Scott, D. (2015). The Herschel view of the dominant mode of galaxy growth from z = 4 to the present day. *A&A*, *575*, A74.

Seyfert, C. K. (1943). Nuclear Emission in Spiral Nebulae. *ApJ*, *97*, 28.

Speagle, J. S., Steinhardt, C. L., Capak, P. L., & Silverman, J. D. (2014). A Highly Consistent Framework for the Evolution of the Star-Forming "Main Sequence" from z ~0-6. *ApJS*, *214*(2), 15.

Springel, V. (2005). The cosmological simulation code GADGET-2. *MNRAS*, *364*(4), 1105–1134.

Springel, V., Di Matteo, T., & Hernquist, L. (2005a). Modelling feedback from stars and black holes in galaxy mergers. *MNRAS*, *361*(3), 776–794.

Springel, V., & Hernquist, L. (2003). Cosmological smoothed particle hydrodynamics simulations: a hybrid multiphase model for star formation. *MNRAS*, *339*(2), 289–311.

Springel, V., White, S. D. M., Jenkins, A., Frenk, C. S., Yoshida, N., Gao, L., Navarro, J., Thacker, R., Croton, D., Helly, J., Peacock, J. A., Cole, S., Thomas, P., Couchman, H., Evrard, A., Colberg, J., & Pearce, F. (2005b). Simulations of the formation, evolution and clustering of galaxies and quasars. *Nature*, *435*(7042), 629–636.

Springel, V., White, S. D. M., Tormen, G., & Kauffmann, G. (2001). Populating a cluster of galaxies - I. Results at [formmu2]z=0. *MNRAS*, *328*(3), 726–750.

Steinborn, L. K., Dolag, K., Hirschmann, M., Prieto, M. A., & Remus, R.-S. (2015). A refined sub-grid model for black hole accretion and AGN feedback in large cosmological simulations. *MNRAS*, *448*(2), 1504–1525.

Steinborn, L. K., Hirschmann, M., Dolag, K., Shankar, F., Juneau, S., Krumpe, M., Remus, R.-S., & Teklu, A. F. (2018). Cosmological simulations of black hole growth II: how (in)significant are merger events for fuelling nuclear activity? *MNRAS*, *481*(1), 341–360.

Stott, J. P., Hickox, R. C., Edge, A. C., Collins, C. A., Hilton, M., Harrison, C. D., Romer, A. K., Rooney, P. J., Kay, S. T., Miller, C. J., Sahlén, M., Lloyd-Davies, E. J., Mehrtens, N., Hoyle, B., Liddle, A. R., Viana, P. T. P., McCarthy, I. G., Schaye, J., & Booth, C. M. (2012). The XMM Cluster Survey: the interplay between the brightest cluster galaxy and the intracluster medium via AGN feedback. *MNRAS*, *422*(3), 2213–2229.

Tacchella, S., Dekel, A., Carollo, C. M., Ceverino, D., DeGraf, C., Lapiner, S., Mandelker, N., & Primack Joel, R. (2016). The confinement of star-forming galaxies into a main sequence through episodes of gas compaction, depletion and replenishment. *MNRAS*, *457*(3), 2790–2813.

Teklu, A. F., Remus, R.-S., Dolag, K., & Burkert, A. (2017). The morphology-density relation: impact on the satellite fraction. *MNRAS*, *472*(4), 4769–4785.

Tornatore, L., Borgani, S., Dolag, K., & Matteucci, F. (2007). Chemical enrichment of galaxy clusters from hydrodynamical simulations. *MNRAS*, *382*(3), 1050–1072.

Tornatore, L., Borgani, S., Matteucci, F., Recchi, S., & Tozzi, P. (2004). Simulating the metal enrichment of the intracluster medium. *MNRAS*, *349*(1), L19–L24.

Torrey, P., Wellons, S., Machado, F., Griffen, B., Nelson, D., Rodriguez-Gomez, V., McKinnon, R., Pillepich, A., Ma, C.-P., Vogelsberger, M., Springel, V., & Hernquist, L. (2015). An analysis of the evolving comoving number density of galaxies in hydrodynamical simulations. *MNRAS*, *454*(3), 2770–2786.

Tran, K.-V. H., Papovich, C., Saintonge, A., Brodwin, M., Dunlop, J. S., Farrah, D., Finkelstein, K. D., Finkelstein, S. L., Lotz, J., McLure, R. J., Momcheva, I., & Willmer, C. N. A. (2010). Reversal of Fortune: Confirmation of an Increasing Star Formation-Density Relation in a Cluster at z = 1.62. *ApJ*, *719*(2), L126–L129.

van den Bosch, F. C., Pasquali, A., Yang, X., Mo, H. J., Weinmann, S., McIntosh, D. H., & Aquino, D. (2008). Satellite Ecology: The Dearth of Environment Dependence. *arXiv e-prints*, (p. arXiv:0805.0002).

von der Linden, A., Wild, V., Kauffmann, G., White, S. D. M., & Weinmann, S. (2010). Star formation and AGN activity in SDSS cluster galaxies. *MNRAS*, *404*(3), 1231–1246.

Wang, C., Li, R., Gao, L., Shan, H., Kneib, J.-P., Wang, W., Chen, G., Makler, M., Pereira, M. E. S., Wang, L., Maia, M. A. G., & Erben, T. (2018). Do satellite galaxies trace matter in galaxy clusters? *MNRAS*, *475*(3), 4020–4026.

Webster, B. L., & Murdin, P. (1972). Cygnus X-1-a Spectroscopic Binary with a Heavy Companion ? *Nature*, *235*(5332), 37–38.

Weinberg, S., & Steven, W. (1972). *Gravitation and Cosmology: Principles and Applications of the General Theory of Relativity*. Wiley.
URL https://books.google.si/books?id=c5fvAAAAMAAJ

Wetzel, A. R., Tinker, J. L., Conroy, C., & van den Bosch, F. C. (2013). Galaxy evolution in groups and clusters: satellite star formation histories and quenching time-scales in a hierarchical Universe. *MNRAS*, *432*(1), 336–358.

Whitaker, K. E., Franx, M., Bezanson, R., Brammer, G. B., van Dokkum, P. G., Kriek, M. T., Labbé, I., Leja, J., Momcheva, I. G., Nelson, E. J., Rigby, J. R., Rix, H.-W., Skelton, R. E., van der Wel, A., & Wuyts, S. (2015). Galaxy Structure as a Driver of the Star Formation Sequence Slope and Scatter. *ApJ*, *811*(1), L12.

Wiersma, R. P. C., Schaye, J., & Smith, B. D. (2009). The effect of photoionization on the cooling rates of enriched, astrophysical plasmas. *MNRAS*, *393*(1), 99–107.

Wolfe, A. M., & Burbidge, G. R. (1970). Black Holes in Elliptical Galaxies. *ApJ*, *161*, 419.

Wyder, T. K., Martin, D. C., Schiminovich, D., Seibert, M., Budavári, T., Treyer, M. A., Barlow, T. A., Forster, K., Friedman, P. G., Morrissey, P., Neff, S. G., Small, T., Bianchi, L., Donas, J., Heckman, T. M., Lee, Y.-W., Madore, B. F., Milliard, B., Rich, R. M., Szalay, A. S., Welsh, B. Y., & Yi, S. K. (2007). The UV-Optical Galaxy Color-Magnitude Diagram. I. Basic Properties. *ApJS*, *173*(2), 293–314.

Yoon, Y., Im, M., & Kim, J.-W. (2017). Massive Galaxies Are Larger in Dense Environments: Environmental Dependence of Mass-Size Relation of Early-type Galaxies. *ApJ*, *834*(1), 73.

Zel'dovich, Y. B., & Novikov, I. D. (1964). The Radiation of Gravity Waves by Bodies Moving in the Field of a Collapsing Star. *Soviet Physics Doklady*, *9*, 246.

Zhao, D. H., Mo, H. J., Jing, Y. P., & Börner, G. (2003). The growth and structure of dark matter haloes. *MNRAS*, *339*(1), 12–24.

Zwicky, F. (1933). Die Rotverschiebung von extragalaktischen Nebeln. *Helvetica Physica Acta*, *6*, 110–127.

Acknowledgments

This work would not have been possible without my supervisors Klaus Dolag, Dunja Fabjan and Veronica Biffi, who guided me with their invaluable advice and regular discussions while encouraging my curiosity and letting me explore the topics I found particularly exciting. I am indebted to G3READ library[1] by Antonio Ragagnin for making data reading and processing easier. I would also like to sincerely thank other members of the CAST group for their regular suggestions and encouragement, members of other groups who were always eager to help and provide invaluable insights into various topics of astrophysics, cosmology and statistics, and everyone who supported me during my studies. I am also grateful to Slovenian Ad Futura and Zois Scholarship funds for financing my studies and my stay in Munich.

[1] github.com/aragagnin/g3read

Selbstständigkeitserklärung

Hiermit erkläre ich, die vorliegende Arbeit selbstständig verfasst zu haben und keine anderen als die in der Arbeit angegebenen Quellen und Hilfsmittel benutzt zu haben.

I hereby declare that this thesis is my own work, and that I have not used any sources and aids other than those stated in the thesis.

Munich, August 24, 2022

_____

Gregor Rihtaršič